

1 Author Response to Both Referee Comments:

2  
3 Response: We thank the two reviewers for thoughtful suggestions and constructive criticism that  
4 have helped us improve our manuscript. Below we provide responses to reviewer concerns and  
5 suggestions in blue font.

6  
7 Reviewer 1:

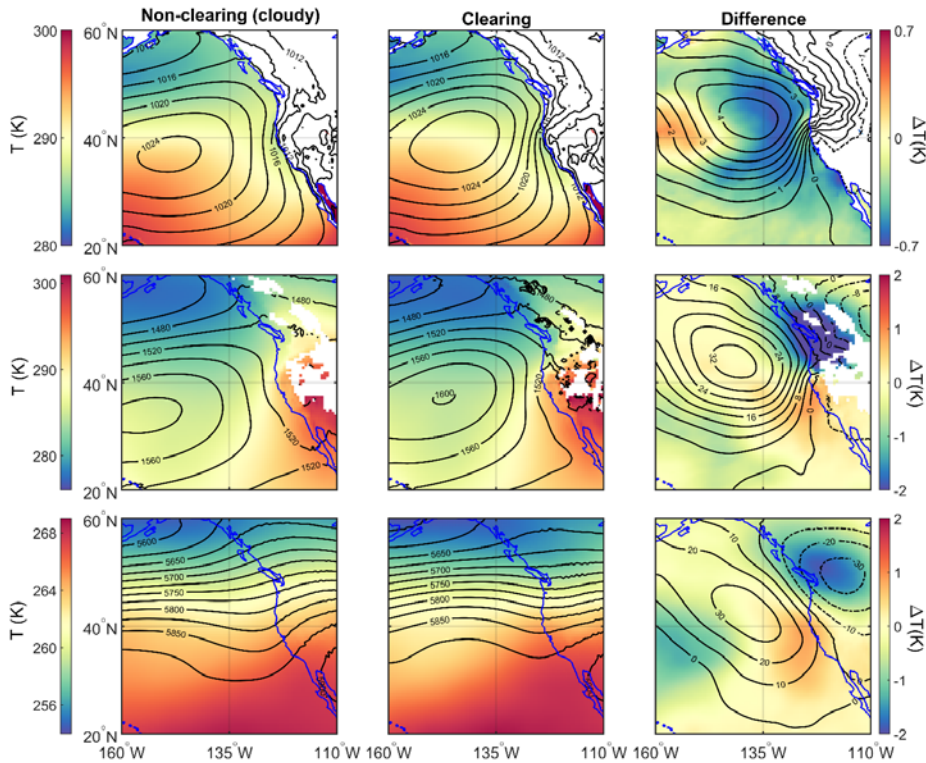
8 General comments: This paper presents a new dataset of stratocumulus cloud clearings off the  
9 California coast derived from satellite observations, and examines this dataset with a variety of  
10 perspectives, including composites of satellite and reanalysis data, aircraft case studies, and a  
11 machine learning-based examination of clearing growth rates. The multitude of approaches is  
12 thorough and effective at providing a very in-depth characterization of clearing events. The paper  
13 is well-written, the text well-supported by the provided figures, and related work is sufficiently  
14 cited and referenced.

15  
16  
17 With regards to interpretation, there are a few areas where I feel the authors can improve and  
18 clarify the message of this paper. The most general is in the interpretation of how the large-scale  
19 conditions relate to cloud clearings (mainly sections 3.2, 3.3). For a clearing event to take place  
20 and be manually identified as described in section 2.1, two conditions must be met: there must be  
21 a cloud deck present, and then there must be a coastal clearing that occurs. In other words, the  
22 environment must be initially great for a cloudy MBL, and also eventually (at least coastally)  
23 poor for a cloudy MBL. The authors spend much of their interpretation arguing (and  
24 convincingly so) why certain factors (e.g. offshore winds) would be detrimental to clouds and  
25 result in a clearing, but not much on the first condition. For example, when it comes to  
26 interpreting the link between clearing days and enhanced stability (Fig 9b), I would expect that it  
27 is not so much that the stability is causing a clearing, but rather the link between strong LTS and  
28 cloudiness that allows there to be a cloud deck to erode in the first place. Whether a particular  
29 environmental factor is predictive of there being a cloud deck, or predictive of it being eroded, is  
30 something that can help understand some of the less explained results in the paper, in particular  
31 when comparing clearing vs non-clearing days. An obvious one would be the overall higher  
32 cloud fraction on clearing days. Presumably, a day with no stratocumulus deck in which to  
33 identify a clearing would be classified as “non-clearing day” (if this is incorrect and non-cloudy  
34 days are discarded, this should be clarified in section 2.1), and therefore days in which the large-  
35 scale conditions in the NEP were unfavourable for clouds would be mixed together with cases  
36 which were very favourable to clouds and no clearing occurred in the ‘non-clearing day’  
37 category. While it would be sufficient to see this discussed in the interpretation with no  
38 additional figures, for their own interest the authors might consider splitting their ‘non-clearing  
39 days’ (of which there are approximately twice as many as clearing days anyways) into two sets,  
40 based on some criteria of overall cloudiness, and a three-way comparison between ‘overall clear  
41 days’, ‘cloudy days-with clearing’ and ‘cloudy days-no clearing’ might prove more interpretable.

42  
43 Response:

44  
45 According to the reviewer’s comment, we decided to split non-clearing events into two sub-  
46 categories of clear and non-clear based on an overall cloud fraction threshold 0.5. Based on this

47 criterion, 529 cases out of total 614 non-clearing days were further classified as cloudy non-  
 48 clearing cases. As a result, the influence of events with unfavorable large scale conditions for  
 49 low-level cloud formation are minimized. Then, we constructed the climatology comparisons of  
 50 important large scale parameters between clearing and non-clearing (cloudy) conditions similar  
 51 to Fig.7 in the manuscript. The results are shown in the following figure:  
 52



53  
 54  
 55 Figure: Climatology of non-clearing (cloudy with CF > 0.5 for study region between 135-115° W  
 56 and 30-50° N) and clearing days as well as their differences (clearing minus non-clearing) during  
 57 the summers (JJA) between 2009 and 2018 for a) mean sea level pressure (contours in hPa) and  
 58 air temperature (color map) at sea surface, b) 850 hPa geopotential heights (contours in m) and  
 59 air temperature (color map), and c) 500 hPa geopotential heights (contours in m) and air  
 60 temperature (color map). The data were obtained from MERRA-2 reanalysis. Differences  
 61 (clearing minus non-clearing) are shown in the farthest right column with separate color scales.  
 62 White areas indicate no data were available.  
 63

64 As it turns out, the general features were preserved after subcategorizing non-clearing events  
 65 based on cloud fraction. This result convinced us that the general mechanisms including the

66 displacement/enhancement of the Pacific high associated with clearing events stem from the  
67 nature of clearings and not from our analysis method. We have decided to not include this  
68 analysis in the manuscript as it might distract the discussion presented in the body of the paper.  
69 However, we revised the discussion of Section 3.2 to address reviewer’s comment regarding  
70 clarifying if certain parameters (like greater *LTS*) are responsible for clearing formation. We  
71 refer the reviewer to edits in Section 3.2 for the concern raised in this comment.

72  
73 This same point is also relevant for the growth rate discussion. The authors show that the initial  
74 growth rate is strongest. A high growth rate would obviously correlate with a larger final clearing  
75 area, and this perspective is taken throughout the discussion of growth rate influences, but also a  
76 high growth rate may be associated with initially smaller clearings (this is supposition, though  
77 the authors could easily investigate in their dataset by examining whether the fastest growing  
78 clearings tended to have smaller-than-average initial sizes). Figures 4a supports this however; the  
79 presence of a longer lower tail on 9 a.m. size and absence of a longer upper tail on 12 p.m. size  
80 (though the log scale might be overemphasizing this) indicates that small initial clearings and  
81 not large final clearings are more likely to be the result of a high growth rate. In this case, it  
82 would be equally valid to explain why certain predictors of growth rate might be associated with  
83 enhanced nighttime cloudiness (again, such as the 1 parameter, T850 or possibly *LTS*), and  
84 therefore a well (re-)formed initial deck that is then subsequently susceptible to breakup. Again,  
85 this point can largely be addressed in the discussion of results or by author rebuttal and does not  
86 require additional figures.

87  
88 Response:

89  
90 We addressed this comment by computing the average initial size of clearings (at the time relevant  
91 to image 1) which had growing rates (between image 1 and 2) faster than the 95<sup>th</sup> percentile of all  
92 growth rates. This analysis reveals that in fact the average initial size of the aforementioned subset  
93 of clearings is 239,100 km<sup>2</sup>, while the average size of all clearings is 118,150 km<sup>2</sup>. This suggests  
94 that the reviewer’s speculation is not the case as the fastest growing clearings did not tend to have  
95 smaller than average initial sizes. Thus, we have decided to not change any part of manuscript  
96 based on this comment.

97  
98 Specific comments:

99 Section 2.1, line 119: Can you describe in slightly more detail what was necessary for the visual  
100 identification of a clearing event? Approximately how large, how distinct, how much cloud had  
101 to be adjacent to the clearing? Were days when the Sc deck was completely detached from the  
102 coast or absent considered?

103  
104 Response:

105  
106 We added the following description in Section 2.1 in response to this comment:

107  
108 (i) “Each day’s sequence of GOES images were visually inspected to identify if a clearing  
109 event was present. This involved utilizing the following general guidelines: (i) There had  
110 to be sufficient cloud surrounding the clearing area that the clearing’s borders could be  
111 approximately identified, which excluded cases with highly broken cloud deck; (ii)

112 Clearings that were not connected to land between 30°-50° N in any of daily images were  
113 excluded; (iii) Days with the cloud deck completely detached from the coast between 30°-  
114 50° N were not considered; and (iv) Only clearings with a maximum daily area of greater  
115 than 15,000 km<sup>2</sup> (which translates to a clearing length on the order of 100 km) were  
116 considered. Consequently, the statistics presented in Section 3.1.1 represent a lower limit  
117 of clearing occurrence in the study region. However, it is expected that the qualitative  
118 trends discussed in Section 3.1.1 are representative of clearing behavior in the study  
119 region.”  
120

### 121 Section 3.2 (Clearing vs Non-Clearing)

122 The difference in subsidence between clearing and non-clearing days seems stark and  
123 geographically well-matched to the clearing locations, and yet it comes out as minimally  
124 important in the PD analysis. Is the only effect of subsidence to lead to a drier lower FT and  
125 therefore all its signal is captured in T850? The w700 discussion seemed very brief.  
126

127 Response: The influence of subsidence on clearing growth is further explained in Section 3.3 as  
128 follows:

129  
130 “The relationship between  $\omega$  at 700 hPa and  $PD_{GR_{Area}}$  is complex. Brueck et al. (2015) suggested  
131 that enhanced  $\omega_{700}$  promotes cloudiness due to its link to higher *LTS*. Myers and Norris (2013)  
132 further showed that stronger subsidence can reduce *CF* (at fixed inversion strength) by pushing  
133 down the top of the MBL, which is also supported by Bretherton et al. (2013). The  $PD_{GR_{Area}}$   
134 profile of  $\omega_{700}$  exhibited a minimum point near a value of  $0 - 0.2 \text{ Pa s}^{-1}$ , with increases in  $GR_{Area}$   
135 below and above that range. The increase in  $PD_{GR_{Area}}$  with  $\omega$  values above  $0.2 \text{ Pa s}^{-1}$  can be  
136 attributed to the negative influence of subsidence on lower *CF* (via pushing down the top of the  
137 MBL) as discussed by Myers and Norris (2013). Conversely, the increase in  $GR_{Area}$  with  
138 decreasing  $\omega$  values below  $0 \text{ Pa s}^{-1}$  can be due to upward motion reducing the strength of the  
139 inversion capping the MBL, which is important to sustain the cloud deck. Vertical motions  
140 represented by the  $\omega_{700}$  parameter could also induce dynamical circulations affecting cloud top  
141 processes such as shear and entrainment.”  
142

143 The difference in AOD (low AOD on clearing days, mainly from 43N and up) may be  
144 explainable by the circulations shown in figure 8, with anomalously northerly and westerly flow  
145 bringing in relatively cleaner air from the marine midlatitudes. That being said, there is no  
146 obvious connection between the AOD and Nd maps (low AOD but high Nd on clearing days,  
147 though not collocated) that would suggest that the AOD anomalies are having any significant  
148 microphysical effect in terms of increasing available CCN, even north of the clearing region.  
149 One remedy would be backtrajectory analysis from the low AOD anomaly region, or else  
150 looking at the species of aerosol in MERRA-2 to see whether summertime wildfires (which have  
151 a large effect on AOD) are impacting the AOD results. The authors state that this may be left for  
152 future work, which I would agree with.  
153

154 Response: This could be subject of future work. Too much for this current paper in our view.  
155

156 Section 3.3 (Growth Rates): It’s not clear to me that the condition of requiring only that  $r_2 < 0.5$   
157 is a sufficient independence constraint to allow for accurate interpretation of the PD results. For

158 true independence, the authors could have performed an EOF decomposition of all mentioned  
159 variables, including those that would clearly correlate strongly with other variables (e.g. LTS,  
160 EIS, which as the authors point out are crucial MBL cloud variables), perform the GBRT  
161 regression and PD analysis, and additionally the correlation of leading EOFs with input  
162 variables. I admit that this would add a level of interpretation, but it would more effectively deal  
163 with the tricky problem that so many of these variables are correlated. As it stands the selection  
164 of variables seems a little arbitrary, and it is not clear that the resulting ranking of the variables in  
165 Figure 11 is physically meaningful. It might be helpful to see another relative ordering of the  
166 importance of these variables in accurately determining the growth rate, such as permutation  
167 feature importance. Machine learning results are inherently difficult to interpret and the authors  
168 have done a more thorough job than many, but one way to improve robustness of interpretation  
169 is using multiple evaluation methods.

170

171 Response:

172 We revised the test regarding  $r^2$  criterion to emphasize that the threshold value of 0.5 is chosen  
173 based on trial and error and it will only reduce the negative impact of correlated variables and  
174 will not completely remove undesired effects:

175

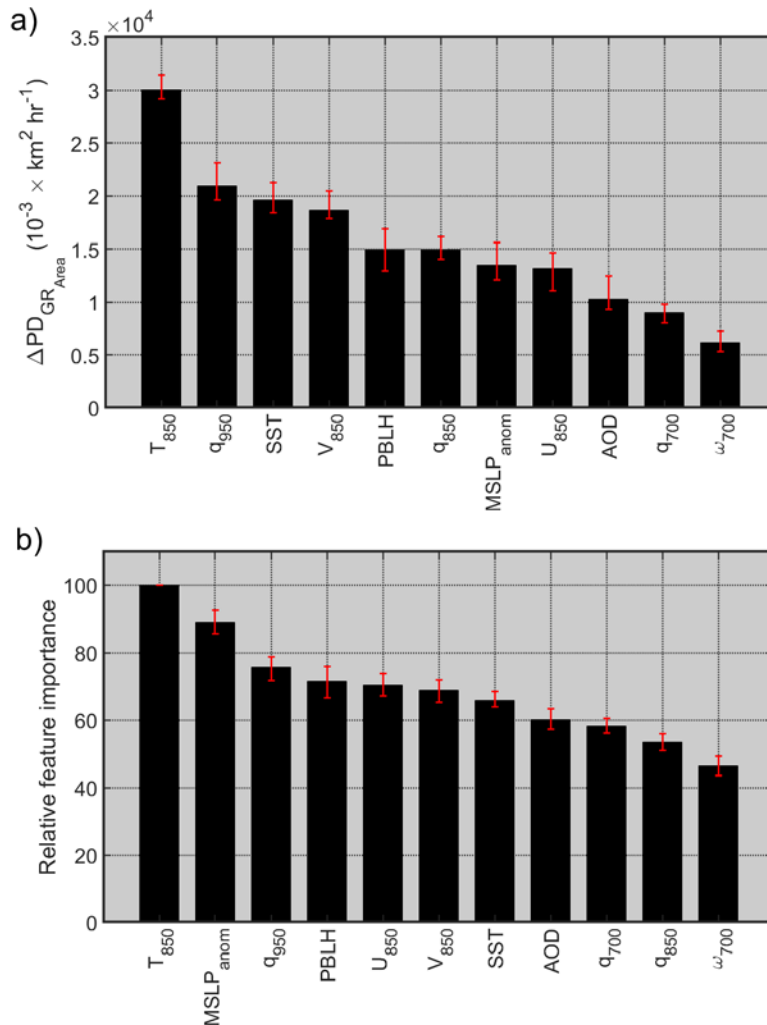
176 “While *PD* plots are not flawless in capturing the influence of each variable in the model,  
177 especially if the input variables are strongly correlated, they provide useful information for  
178 interpretation of GBRT results (Friedman and Meulman 2003; Elith et al., 2008). To decrease the  
179 undesired influence of correlated variables on *PD* profiles, an arbitrary  $r^2$  threshold of 0.5 was  
180 used based on the linear regressions between prospective input parameters. For instance, there  
181 were three choices of air temperature (i.e., at 950, 850, and 700 hPa), but based on the  $r^2$  criterion,  
182 only one ( $T_{850}$ ) was used in the model to minimize the unwanted impact of dependent input  
183 parameters. Lower tropospheric stability (*LTS*: defined as the difference between the potential  
184 temperature of the free troposphere (700 hPa) and the surface) is the stability parameter that has  
185 been widely used as a key factor controlling the coverage of stratocumulus clouds. However, in  
186 this study, the effects of stability were examined by putting  $T_{850}$  and *SST* into the model without  
187 explicitly including *LTS*. The correlation between *LTS* and  $T_{850}$  prevented them to be used as input  
188 parameters simultaneously. Using  $T_{850}$  and *SST* instead of *LTS* is advantageous because the results  
189 can be more informative by revealing different impacts of the two individual parameters on the  
190 model’s output rather than just one parameter in the form of *LTS*. In addition, the mean sea level  
191 pressure anomaly ( $MSLP_{anom}$ ) was used as an input parameter, which was calculated in reference  
192 to the average values of *MSLP* for the summer months for the study period. In the end, the  
193 following 11 predicting variables from MERRA-2 were used as input parameters for the GBRT  
194 simulations, with data product details summarized in Table 1: *AOD*,  $T_{850}$ ,  $q_{950}$ ,  $q_{850}$ ,  $q_{700}$ , *SST*,  
195  $MSLP_{anom}$ ,  $U_{850}$ ,  $V_{850}$ , *PBLH*, and  $\omega_{700}$ . It is important to note that the results of extensive sensitivity  
196 tests led to the selection of the set of parameters presented in this study. Also, these sensitivity  
197 tests confirmed that the general conclusions presented here were preserved regardless of using  
198 different sets of the input parameters.

199 To train, test, and validate the statistical models, the dataset was split into random parts. The  
200 training set was comprised of 75% of the data points, 30% of which were randomly selected for  
201 validation. This process helped reduce variance and increase model robustness. The remaining  
202 25% of the data points comprised the test dataset. The model setup was tuned using training data,  
203 for which different scenarios were tested that were specified by a parameter grid through a 10-

204 fold cross-validated search. The model was run on the dataset 30 times to achieve robust results.  
205 To qualitatively rank the input parameters based on their influence on growth rates, two scoring  
206 metrics were calculated over 30 runs: (i) differences between the maximum and minimum of  $PD$   
207 ( $\Delta PD$ ); and (ii) the relative feature importance following the method developed by Friedman  
208 (2001), which is determined by the frequency that a variable is chosen for splitting, weighted by  
209 the gained improvement due to each split and averaged over all trees (Friedman and Meulman  
210 2003; Elith et al., 2008).”

211  
212 We have also calculated the relative feature importance in addition to the range of  $PD$  provide in  
213 Fig. 10. As the reviewer suggested, this may help to make a more robust conclusion regarding  
214 the relative importance of input variables in the GBRT model. We updated Fig. 10 and  
215 discussion related to that figure as follows:

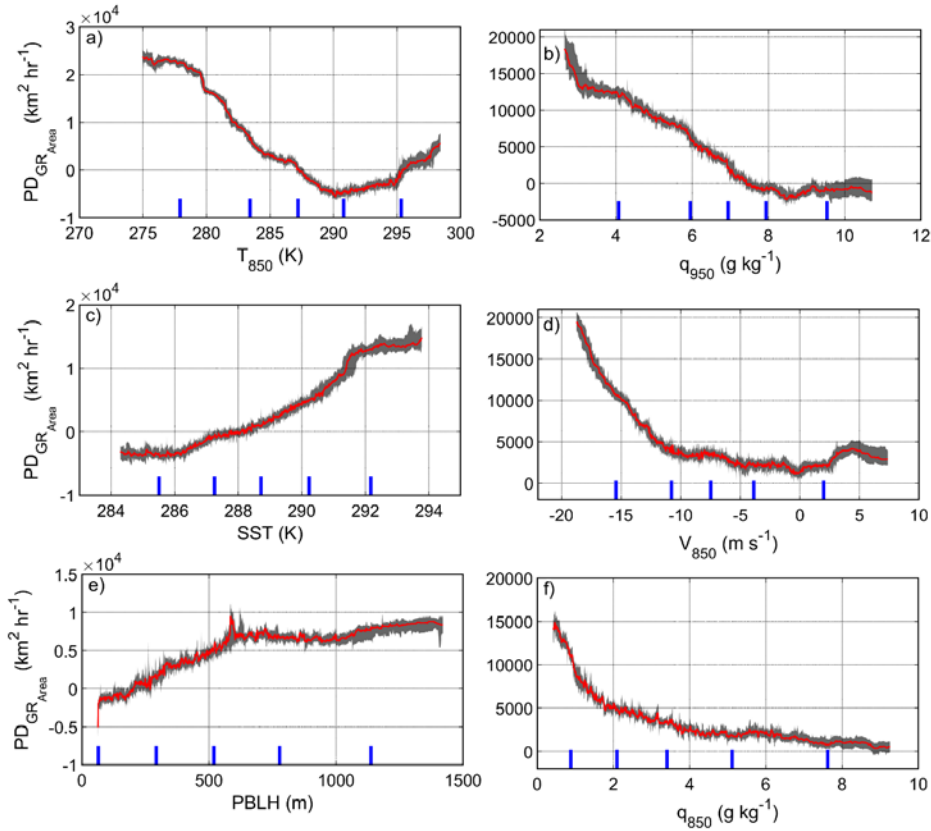
216  
217 “The range of  $PD$ s for each individual environmental parameter and the relative feature  
218 importance are used here as two proxies for the sensitivity of clearing growth rates to that  
219 specific parameter. Higher  $PD$  ranges translate to a higher sensitivity of  $GR_{Area}$  to that specific  
220 parameter, indicating that it is likely a major influential factor. In addition, the relative feature  
221 importance indicates how useful each parameter was in building the GBRT model. The range of  
222  $PD$  of clearing growth rates and relative feature importance for all the parameters included in the  
223 GBRT model are provided in Fig. 10, moving from left to right in order of highest to lowest  
224 influence in the model. While it is expected that the results of these two methods of rankings do  
225 not match entirely (Fig. 10a and 10b), certain characteristics are similar between these two  
226 proxies: 1- using both proxies,  $T_{850}$  and  $\omega_{700}$  appeared as the top and lowest ranking parameters,  
227 respectively; 2-  $q_{950}$  comes out among top the most important parameters as second and third  
228 place according to the range of  $PD$  and relative feature importance proxies, respectively; 3-  $AOD$   
229 and  $q_{700}$  emerged among the four lowest-ranking parameters; 4-  $SST$  and  $V_{850}$  appear next to each  
230 other in the ranking using both scoring proxies. There are some distinct differences among the  
231 ranking of parameters as shown in Fig. 10. For instance, while  $MSLP_{anom}$  appeared as a  
232 moderately influential parameter in  $GR_{Area}$  according to  $PD$  proxy, this parameter turned out to  
233 be the second most important variable using relative feature importance proxy. In another  
234 example,  $q_{850}$  has the second least important rank according to relative importance feature proxy,  
235 but it is moderately important based on the range of  $PD$  (Fig. 10a). The observed discrepancies  
236 between the results of two proxies can stem from underlying differences in the methods used to  
237 quantify the relative significance of each parameter. Moreover, the relative feature importance  
238 proxy may be less susceptible to the unwanted influence of highly correlated input predictors on  
239 the ranking outcome (Hastie et al., 2009).”



240  
 241 **Figure 10.** Two scoring methods used for measuring the relative influence of input variables in  
 242 the GBRT model: a) the median difference of maximum and minimum partial dependence (PD)  
 243 of clearing growth rate ( $GR_{Area}$ ), and b) the median of relative feature importance calculated based  
 244 on the method developed by Friedman (2001). Error bars represent the range of variability in 30  
 245 model runs. Note that GBRT simulations were performed using clearing growth rates obtained  
 246 from the analysis of first and second GOES images (~09:00 – 12:00 PST) for all 306 clearing  
 247 events examined.  
 248

249 One area where I think the authors may have stretched the interpretation past the limits of PD  
 250 analysis is lines 546-558, for instance with the discussion of MSLP and GR. The problem with  
 251 using PD and correlated variables is that you risk simulating completely nonphysical states  
 252 which produce nonsensical results. The high and low tails of the PD sensitivity to MSLP could  
 253 be a result of the breaking of assumed independence. This could be ameliorated with the addition  
 254 of a rug plot/histogram to each Figure 12 subplot, showing some kind of likelihood or frequency  
 255 of occurrence of that particular state (how often a -500 Pa MSLP anomaly occurred in the region  
 256 affects the degree to which the interpretation of that portion of the PD plot is nonphysical), or the  
 257 addition of some ICE (individual conditional expectation) plots, both of which are commonly  
 258 used to help with the interpretation of PD plots.

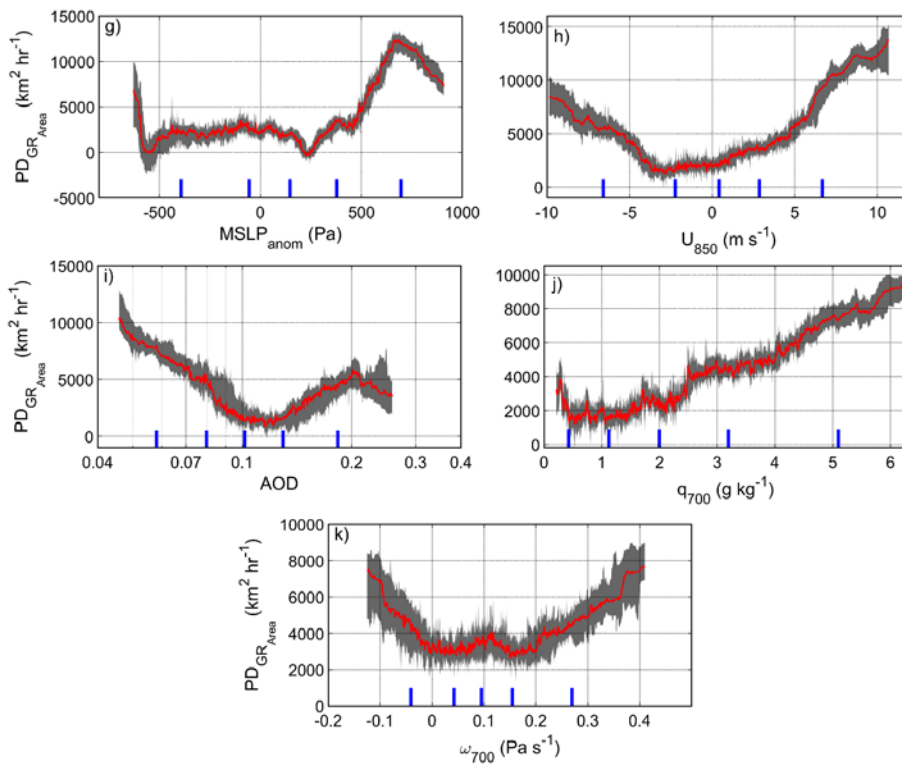
259  
 260 **Response:**  
 261 To address this comment, we updated Fig. 11 with the information about the distributions of data  
 262 by marking the various percentiles (5<sup>th</sup>, 25<sup>th</sup>, 50<sup>th</sup>, 75<sup>th</sup>, and 95<sup>th</sup>) of input data as blue markers.



263 **Figure 11.** The median partial dependence (PD) of clearing growth rate ( $GR_{Area}$ ) on the following  
 264 parameters: a) air temperature at 850 hPa ( $T_{850}$ ), b) air specific humidity at 950 hPa ( $q_{950}$ ), c) sea  
 265 surface temperature (SST).



266 surface temperature (*SST*), d) meridional wind speed at 850 hPa ( $V_{850}$ ), e) planetary boundary layer  
 267 height (*PBLH*), f) air specific humidity at 850 hPa ( $q_{950}$ ), g) mean sea level pressure anomaly  
 268 ( $MSLP_{anom}$ ), h) zonal wind speed at 850 hPa ( $U_{850}$ ), i) aerosol optical depth (*AOD*), j) air specific  
 269 humidity at 700 hPa ( $q_{700}$ ), and k) vertical pressure velocity at 700 hPa ( $\omega_{700}$ ). Grey Shaded areas  
 270 represent the range of variability of *PD* for 30 model runs. Blue lines represent the values of the  
 271 (left to right) 5<sup>th</sup>, 25<sup>th</sup>, 50<sup>th</sup>, 75<sup>th</sup>, and 95<sup>th</sup> percentiles of the input parameter. GBRT simulations  
 272 were performed using clearing growth rates obtained from the analysis of first and second GOES  
 273 images (09:00 – 12:00 PST) for all 306 clearing events examined.  
 274



275  
 276 **Figure 12 (continued).**

277  
 278  
 279 Technical corrections/suggestions:  
 280 Figure 12 caption (line 1250): grey shaded areas, not red.

281 **Response: Fixed.**

282  
 283  
 284 Figure 13: It would be helpful to see the inversion levels from Table 3 marked on these  
 285 plots.

286  
287 Response: We think adding the inversion heights to Fig. 13 may confuse readers as they can  
288 easily find them in Table 3 and their values are different for cloudy and clear columns. Also,  
289 readers can spot the base of inversion according to the cloud top marked in Fig. 13.  
290

291 Reviewer 2:

292 Review of "Stratocumulus cloud clearing: Statistics from satellites, reanalysis models, and  
293 airborne measurements" by Dadashazar et al.

294  
295 Using several data sources and a machine learning technique, this paper examines the topic of  
296 marine boundary layer stratiform cloud clearings over the northeastern Pacific Ocean. The study  
297 uses a holistic approach by considering spatial scales ranging from the synoptic-scale to the  
298 microscale. The authors' do a nice job of utilizing satellite retrievals, reanalysis grids, and  
299 airborne measurements to highlight the complexity of the problem which involves interactions  
300 between the western United States coastline and the marine environment – a region which has  
301 historically received much attention in the literature.

302  
303 I think that the results stemming from this work are certainly interesting and worthy of  
304 publication. Because the authors' cover so many topics, I do have several major comments and  
305 many minor comments. The major comments concern one of the techniques used for the MODIS  
306 processing in addition to interpretation of some of the results. Overall, I recommend that the  
307 paper be accepted for publication once the authors' address my comments.

308  
309 Major/general comments:

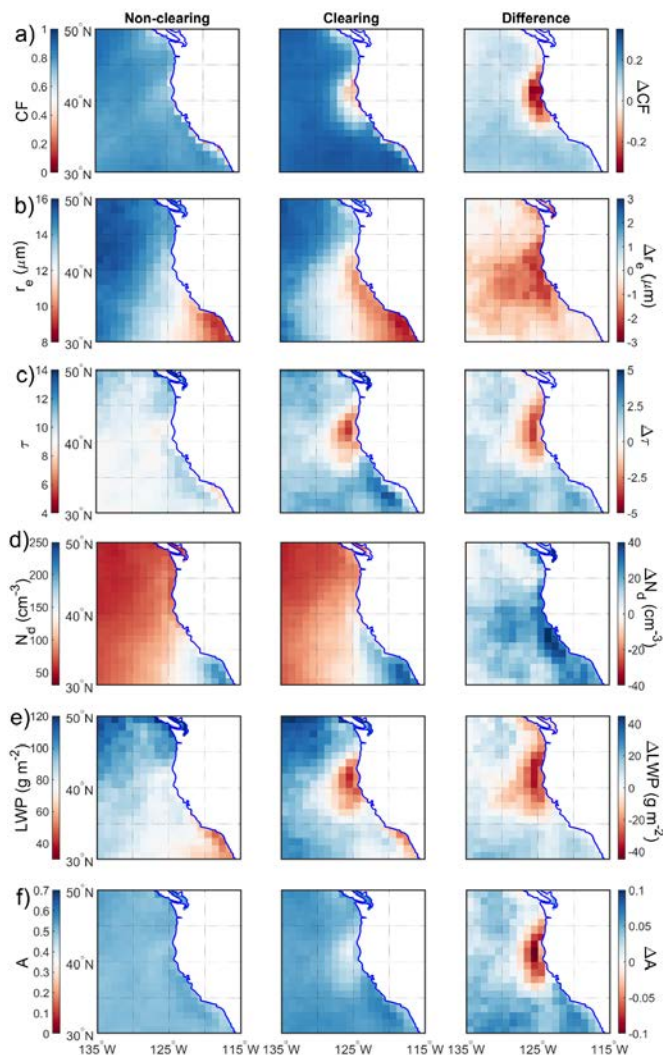
310 1. I am slightly concerned about the methods used to estimate cloud droplet number  
311 concentration,  $N_d$ . Because the authors' compare plots of  $N_d$  between clearing and non-clearing  
312 days, certainly there are differences in cloud base temperature and pressure (as implied by  
313 several figures shown in this study) that would affect the adiabatic lapse rate of LWC. Therefore,  
314 using an average value of the adiabatic lapse rate of LWC, which is derived from measurements  
315 concentrated near the central California coastline (Braun et al., 2018), may not be representative  
316 of the much larger domain on which the present study focuses. I recommend that the authors'  
317 calculate the adiabatic lapse rate of LWC using the MODIS retrievals of cloud top temperature  
318 and pressure. I do not mean to sound nitpicky here, but estimation of  $N_d$  already carries  
319 relatively large uncertainty, so I think that it is only fair that you estimate it as accurately as  
320 possible. It will be interesting to see how sensitive the  $N_d$  estimate is to this lapse rate  
321 calculation.

322  
323 Response:

324  
325 Addressing the reviewer concern about using a constant value for adiabatic ( $\Gamma_{ad}$ ) lapse rate of  
326 LWC, we recalculated  $N_d$  values for both MODIS-Aqua and Terra using  $\Gamma_{ad}$  that are dependent of  
327 cloud top temperature and pressures. Panel d of Figures 9 and S6 are also updated accordingly. It  
328 turns out the above modification had negligible effects on the average spatial distribution of  $N_d$   
329 over the region of interest on both clearing and non-clearing days. As such, we have decided to  
330 not change any discussion regarding Fig. 9 in the manuscript. We have also revised a few lines in  
331 Section 2.1 to describe the methodology of estimating  $N_d$  from MODIS observations as follow:

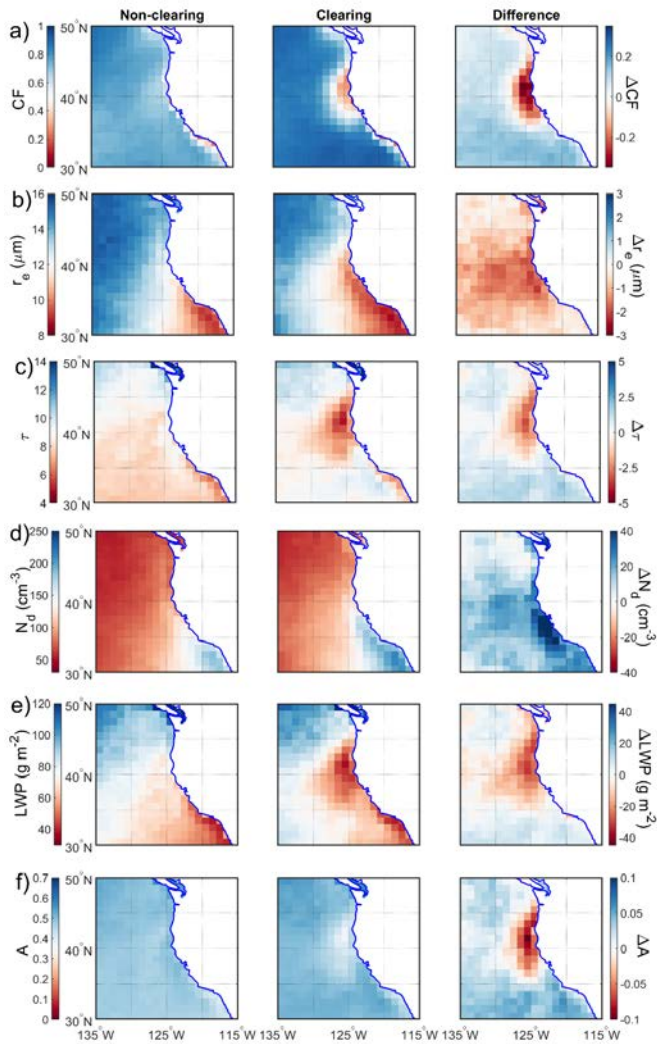
332  
333 "...where  $\rho_w$  is the density of liquid water,  $\Gamma_{ad}$  is the adiabatic lapse rate of liquid water content  
334 (LWC), and the parameter  $k$  is representative of droplet spectral shape as the cube of the ratio  
335 between the volume mean radius and the effective radius.  $\Gamma_{ad}$  is a function of temperature and  
336 pressure (Albrecht et al., 1990). In this study, cloud top temperature and pressure, provided by

337 MODIS, are used to estimate  $\Gamma_{ad}$  following the methodology described in Braun et al. (2018). A  
 338 constant value of 0.8 (Martin et al. 1994) is assigned to  $k$  in Equation 1.”



339  
 340 **Figure 9.** Average cloud parameters for non-clearing and clearing days obtained from MODIS  
 341 Terra Level 3 (Collection 6.1) data: a) cloud fraction day ( $CF$ ), b) cloud top droplet effective radius  
 342 ( $r_e$ ), c) cloud optical thickness ( $\tau$ ), d) cloud droplet number concentration ( $N_d$ ), e) cloud liquid  
 343 water path ( $LWP$ ), and f) cloud albedo ( $A$ ). Differences (clearing minus non-clearing) are shown  
 344 in the farthest right column with separate color scales. Values from any instances of clear pixels

345 were omitted from the analysis to produce panels b-f. Fig. S6 is an analogous figure based on  
 346 MODIS Aqua data.  
 347



348 **Figure S6.** Average cloud parameters for non-clearing and clearing days obtained from MODIS  
 349 Aqua Level 3 (Collection 6.1) data: a) cloud fraction day (CF), b) cloud top droplet effective  
 350 radius ( $r_e$ ), c) cloud optical thickness ( $\tau$ ), d) cloud droplet number concentration ( $N_d$ ), e) cloud  
 351 liquid water path (LWP), and f) cloud albedo (A). Differences (clearing minus non-clearing) are  
 352

353 shown in the farthest right column with separate color scales. Values from any instances of clear  
354 pixels were omitted from the analysis to produce these figures.

355  
356

357 2. I think that the arguments presented in Section 3.2 regarding the spatial differences in PBLH  
358 (P11, L420-425) require additional explanation. Firstly, citations are needed to support the  
359 presented hypotheses. More importantly, why do you think that CF is higher for the broad study  
360 region on clearing days? What about the synoptic scale scenarios and the role of offshore flow?  
361 Advection of warm air combined with compressional warming near the coastline will increase  
362 layer thickness and therefore thin out the MBL below. This seems like a chicken-egg problem. Is  
363 it actually cloud processes that are responsible for the shallower PBLHs or are the large-scale  
364 dynamics/thermodynamics reducing clouds and therefore causing the shallower PBLHs or  
365 perhaps some combination of the two mechanisms?

366

367 Response:

368

369 We addressed the comment by revising/updating the noted argument presented in Section 3.2 as  
370 follows below. We also added new references to support our discussion.

371

372 “Another key environmental parameter related to MBL cloud coverage is the *PBLH*. Consistent  
373 with previous studies (Neiburger et al., 1961; Wood and Bretherton 2004), regardless of whether  
374 clearings were present, *PBLH* generally increases with distance from the coast (Fig. 8d), where  
375 warmer *SSTs* lead to deeper MBLs by weakening the inversion (Bretherton and Wyant 1997). The  
376 shallowing of the MBL near the California coast is also notable with enhanced gradients in clearing  
377 days. The aforementioned MBL shallowing is believed to be a crucial element in development of  
378 coastal jet off the California coast (Zemba and Friehe 1987; Parish 2000). Previous studies  
379 (Beardsley et al., 1987; Edwards et al., 2001; Parish 2000; Zuidema et al., 2009) also reported  
380 MBL height adjustment in the vicinity of coast due to hydraulic adaptation to coastal topography,  
381 thermally driven circulation, and geostrophic adjustment in the cross-coast direction in response  
382 to the contrast in surface heating between ocean and land. There is also a strong gradient in *PBLH*  
383 along the shoreline in the vicinity of Cape Blanco (Fig. 8d). While the presence of a similar  
384 gradient in *SST* (Fig. 8a) may partly explain the observed gradient in *PBLH*, coastally induced  
385 processes could also play a role.

386 Comparing clearing with non-clearing days, *PBLH* tends to be higher on clearing days,  
387 with the largest differences (~200 m) observed to the north off the coasts of Washington and British  
388 Columbia, which re-emphasizes the important role of coastal topography near Cape Blanco and  
389 Cape Mendocino in mesoscale dynamics (Beardsley et al., 1987; Haack et al., 2001). Zuidema et  
390 al. (2009) suggested that dynamical blocking of the surface winds by the southern Peruvian Andes  
391 contributed to boundary layer thickening by encouraging mesoscale convergence. Enhanced  
392 dynamical blocking of surface winds by coastal topography near Cape Blanco, as suggested by  
393 greater wind speeds on clearing days (Fig. 7a), can lead to a deeper MBL in the coastal regions  
394 north and northwest of Cape Blanco. In contrast, coastal areas south of Cape Blanco, exhibit  
395 negligible differences in *PBLH* between clearing and non-clearing days. In the aforementioned  
396 regions, enhanced hydraulic response (i.e., expansion fan (Parish et al., 2016)) to coastal  
397 topography, may cause slightly shallower MBL on clearing days.

398 Higher MBL depths in the offshore regions of clearing days is noteworthy to discuss. Parameters  
399 influencing MBL depth include entrainment rates, vertical velocity at the top of MBL, and  
400 horizontal advection of MBL (Wood and Bretherton 2004; Rahn and Garreaud 2010). Although  
401 on clearing days there may be greater subsidence rates offshore (Fig. 8c) promoting a shallower  
402 MBL, the sum of entrainment and horizontal advection terms counteract the aforementioned effect  
403 resulting in a deeper MBL. Wood and Bretherton (2004) showed for the Northeast and Southeast  
404 Pacific that entrainment and subsidence were the most influential terms in the MBL prognostic  
405 equation, which acted in the opposite manner. It is also likely that entrainment processes resulting  
406 from changes in small scale turbulence contributed to elevated *PBLH* on clearing days (Randall  
407 1984, Rahn and Garreaud 2010). The maps of *CF* from MODIS Terra (Fig. 9a) can provide at least  
408 one possible explanation for the spatial differences in *PBLH* between clearing and non-clearing  
409 days. Cloud fraction is generally higher for the broad study region on clearing days, which leads  
410 to more opportunity for cloud top radiative cooling to then fuel turbulence in MBL (Wood 2012).  
411 Greater turbulence can lead to a deeper MBL by promoting greater entrainment at the top of MBL  
412 (Randall 1984; Wood 2007).”

413 3. The discussion in Section 3.2 connecting the MERRA-2 and MODIS results raises numerous  
414 questions that the authors’ should address. For example, on P11, L447-448: This is an interesting  
415 yet surprising result. I am wondering how aerosol are treated in MERRA-2. Which aerosol types  
416 are included in the reanalysis? Is AOD calculated differently when clouds are present in a  
417 column? I must say that I am quite surprised that between clearing and non-clearing days, the  
418 MODIS retrievals show a clear difference in microphysical variables suggestive of aerosol  
419 influence, but MERRA-2 AOD does not show a clear deference in aerosol loading. While the  
420 authors’ do provide a possible explanation for this confounding result, I am wondering if it is  
421 possible to look at precipitation rates from the MERRA-2 outputs? Or use the MODIS retrievals  
422 and the RCB-LWP-Nd relationship derived in Comstock et al. (2004) to estimate cloud base  
423 precipitation rate? I think that some general investigative work here would be nice to help shed  
424 light.

425  
426 Reference: Comstock, K.K., Wood, R., Yuter, S.E. and Bretherton, C.S. (2004), Reflectivity and  
427 rain rate in and below drizzling stratocumulus. Q.J.R. Meteorol. Soc., 130:  
428 2891-2918. doi:10.1256/qj.03.187

429  
430 Response: This is an excellent point and gets a bit more into the weeds of the critical details of  
431 how MERRA-2 and MODIS compare. We share here a bit more about MERRA-2:

432  
433 The MERRA-2 aerosol reanalysis (Buchard et al., 2017; Randles et al., 2017) relies on the  
434 GEOS-5 Goddard Aerosol Assimilation System (Buchard et al., 2015) where the Goddard  
435 Chemistry, Aerosol, Radiation, and Transport (GOCART) (Chin et al., 2002) model is used to  
436 simulate 15 externally mixed aerosol tracers including hydrophobic and hydrophilic black carbon  
437 and organic carbon, dust (five size bins), sea salt (five size bins), and  $\text{SO}_4^{2-}$ . Sea salt and dust  
438 emissions are driven by wind speed in the GOCART model. Other species are treated using  
439 various emissions from combustion, biomass burning, biogenic sources, and volcanic emissions.  
440 The dominant removal mechanisms for aerosols include gravitational settling, dry deposition,  
441 and wet scavenging. MERRA-2 assimilates AOD from ground and satellite-based remote  
442 sensors, including AVHRR, AERONET, MISR, and MODIS.  
443

444 Buchard, V., da Silva, A. M., Colarco, P. R., Darmenov, A., Randles, C. A., Govindaraju, R., . . .  
445 Spurr, R. (2015). Using the OMI Aerosol Index and Absorption Aerosol Optical Depth to  
446 Evaluate the NASA MERRA Aerosol Reanalysis. *Atmospheric Chemistry and Physics*, 15(10),  
447 5743-5760. doi:10.5194/acp-15-5743-2015

448  
449 Buchard, V., Randles, C. A., da Silva, A. M., Darmenov, A., Colarco, P. R., Govindaraju, R.,  
450 Ferrare, R., Hair, J., Beyersdorf, A. J., Ziemba, L. D., and Yu, H.: The MERRA-2 Aerosol  
451 Reanalysis, 1980 Onward. Part II: Evaluation and Case Studies, *J Climate*, 30, 6851-6872,  
452 10.1175/Jcli-D-16-0613.1, 2017.

453  
454 Chin, M., Ginoux, P., Kinne, S., Torres, O., Holben, B. N., Duncan, B. N., Martin, R. V., Logan,  
455 J. A., Higurashi, A., and Nakajima, T.: Tropospheric aerosol optical thickness from the  
456 GOCART model and comparisons with satellite and Sun photometer measurements, *J Atmos*  
457 *Sci*, 59, 461-483, Doi 10.1175/1520-0469(2002)059<0461:Taotft>2.0.Co;2, 2002.

458  
459 Randles, C. A., da Silva, A. M., Buchard, V., Colarco, P. R., Darmenov, A., Govindaraju, R.,  
460 Smirnov, A., Holben, B., Ferrare, R., Hair, J., Shinozuka, Y., and Flynn, C. J.: The MERRA-2  
461 Aerosol Reanalysis, 1980 Onward. Part I: System Description and Data Assimilation Evaluation,  
462 *J Climate*, 30, 6823-6850, 10.1175/Jcli-D-16-0609.1, 2017.

463  
464 We added the following text to the paper based on the lengthier description above, which we feel  
465 is adequate to articulate how MERRA-2 handles aerosols:

466  
467 “Of note is that the MERRA-2 aerosol reanalysis relies on the GEOS-5 Goddard Aerosol  
468 Assimilation System (Buchard et al., 2015) for which the Goddard Chemistry, Aerosol,  
469 Radiation, and Transport (GOCART) model (Chin et al., 2002) simulates 15 externally mixed  
470 aerosol tracers including sulfate, dust (five size bins), sea salt (five size bins), and hydrophobic  
471 and hydrophilic black carbon and organic carbon. Of relevance to this study, GOCART applies  
472 wind-speed dependent emissions for sea salt. Furthermore, the dominant removal mechanisms  
473 for aerosols include gravitational settling, dry deposition, and wet scavenging.”

474  
475 Also, we feel as though deeper examination into precipitation rates is best left for future work.  
476 We did not want to get too deep in this current manuscript into the aerosol-related aspects but  
477 believe that there are enough compelling results to investigate the aerosol-related aspects in  
478 subsequent work.

479  
480 Minor/specific comments:

481  
482 1. P2, L41: Do you mean model simulations from this study or previous studies? Please clarify.

483  
484 Response: This study. Revised sentence:

485  
486 “Measurements were compared on both sides of the clear-cloudy border of clearings at multiple  
487 altitudes in the boundary layer and free troposphere, with results helping to support links  
488 suggested by this study’s model simulations.”

489  
  
16



490 2. P3, L54-56: This statement deserves citations; please cite some papers here.

491

492 Response: Added:

493

494 “Stratocumulus clouds also play an important role in the global radiation budget due to their high  
495 albedo contrast with the underlying ocean surface (Hartmann and Short, 1980; Herman et al.,  
496 1980; Stephens and Greenwald, 1991).”

497

498 Hartmann, D. L., and Short, D. A.: On the Use of Earth Radiation Budget Statistics for Studies of  
499 Clouds and Climate, *J Atmos Sci*, 37, 1233-1250, Doi 10.1175/1520-  
500 0469(1980)037<1233:Otuoe>2.0.Co;2, 1980.

501

502 Herman, G. F., Wu, M. L. C., and Johnson, W. T.: The Effect of Clouds on the Earths Solar and  
503 Infrared Radiation Budgets, *J Atmos Sci*, 37, 1251-1261, Doi 10.1175/1520-  
504 0469(1980)037<1251:Teocot>2.0.Co;2, 1980.

505

506 Stephens, G. L., and Greenwald, T. J.: The Earths Radiation Budget and Its Relation to  
507 Atmospheric Hydrology .2. Observations of Cloud Effects, *J Geophys Res-Atmos*, 96, 15325-  
508 15340, Doi 10.1029/91jd00972, 1991.

509

510 3. P3, L85-86: Introduce abbreviations for cloud fraction and cloud liquid water path here?

511

512 Response: Done

513

514 4. P4, L110-112: Are there differences in retrieval and/or post-processing techniques between  
515 GOES-11 and GOES-15 that could impact interpretation/comparison of their results?

516

517 Response: Not to our knowledge.

518

519 5. P4, 119-121: Please explain how you identified a clearing event using visual inspection.

520

521 Response: We added the following description in Section 2.1 in response to this comment:

522

523 “Each day’s sequence of GOES images were visually inspected to identify if a clearing event was  
524 present. This involved utilizing the following general guidelines: (i) There had to be sufficient  
525 cloud surrounding the clearing area that the clearing’s borders could be approximately identified,  
526 which excluded cases with highly broken cloud deck; (ii) Clearings that were not connected to  
527 land between 30°-50° N in any of daily images were excluded; (iii) Days with the cloud deck  
528 completely detached from the coast between 30°-50° N were not considered; and (iv) Only  
529 clearings with a maximum daily area of greater than 15,000 km<sup>2</sup> (which translates to a clearing  
530 length on the order of 100 km) were considered. Consequently, the statistics presented in Section  
531 3.1.1 represent a lower limit of clearing occurrence in the study region. However, it is expected  
532 that the qualitative trends discussed in Section 3.1.1 are representative of clearing behavior in the  
533 study region.”

534

535 6. P5, L146: From which wavelength retrieval are you using data?

536 Response: We added the requested information:

537  
538 “The key daytime parameters (Table 1) retrieved for this study relevant to liquid clouds included  
539 the following, which were retrieved at 2.1  $\mu\text{m}$  and selected based on their importance for marine  
540 boundary layer (MBL) cloud studies:  $CF$  obtained from the MODIS cloud mask algorithm  
541 (Platnick et al., 2003), cloud optical thickness ( $\tau$ ),  $LWP$ , and cloud droplet effective radius ( $r_e$ ).  
542 Detailed information about these MODIS products is described elsewhere (Platnick et al., 2003;  
543 Platnick et al., 2017; Hubanks et al., 2019).”

544  
545 7. P5, L147: Is any day that is not a clearing day lumped in with non-clearing days? Or were  
546 some days not considered in the analysis?

547 Response: A non-clearing day is defined as any summer day between 2009 and 2018 which was  
548 not identified as a clearing day. We clarify this in the first paragraph of Section 3.2 as follows:

549  
550  
551 “Large-scale dynamic and thermodynamic characteristics were contrasted (parameters in Table 1)  
552 between clearing and non-clearing days (Fig. 6). Sub-daily data were averaged up to daily  
553 resolution for parameters of interest, which were subsequently used to produce a climatology for  
554 non-clearing (614 days) and clearing (306 days) cases for the summers between 2009 and 2018. It  
555 is important to note that non-clearing cases include those summer days (e.g., June, July, and  
556 August) from 2009 through 2018 that were not categorized as clearing days. We further calculated  
557 the difference between clearing and non-clearing conditions.”

558  
559 8. P5, L148: Why use 1 deg x 1 deg data rather than the higher resolution data that are available?  
560 I imagine that the resolution of the GOES data are much higher than 1 deg x 1 deg.

561 Response: The reviewer is correct. A decision was made early to use the larger resolution data  
562 early in the study and the results we feel are robust and informative. Future work by anyone  
563 interested can certainly probe similar phenomena at higher resolution, but we decided not to have  
564 to re-do the entire analysis for this comment.

565  
566  
567 9. P5, L150-153: Why are all of these cloud microphysical properties important in the context of  
568 cloud clearings? Some justification in this section would be nice.

569 Response: Text added:

570  
571  
572 “The key daytime parameters (Table 1) retrieved for this study relevant to liquid clouds included  
573 the following, which were selected based on their importance for marine boundary layer (MBL)  
574 cloud studies:”

575  
576 10. P5, L151-153, L156: Please italicize variables here and throughout the remaining text.

577 Response: Done

578  
579 11. P5, L167-170: Does this need to be its own paragraph?

581

582 Response: We added the paragraph in question to the previous paragraph to address this issue.

583

584 12. P5, Section 2.2: Similar to the previous section, it would be nice to hear some justification as  
585 to why you choose the listed parameters/vertical levels. Why are these parameters/vertical levels  
586 important to the analysis? Were other variables considered and found to be not useful?

587

588 Response: We added text to explain our choice of parameters and levels:

589

590 “The parameters were chosen based on their ability to provide a sufficient view of atmospheric  
591 conditions in which MBL clouds form, evolve, and dissipate. Various vertical levels were used  
592 for some MERRA-2 products as a way of obtaining representative information for different  
593 layers of the MBL and free troposphere.”

594

595 13. Figure 2: The gray shading in panels c and d are a bit deceiving. Is the cloud base/top/depth  
596 in panel c truly that horizontally homogeneous? Panel d makes it seem as though cloud extends  
597 from the surface to 1000 m. I think that I understand what you are trying to show, but perhaps  
598 showing it a bit differently would be less confusing.

599

600 Response: We typically show our clouds in this manner in past publications. We find our Fig. 2  
601 caption to be sufficiently clear. And we trust that readers know that the gray box in panel c is  
602 meant to be representative of where clouds were, and they are not that clear-cut linear at the  
603 edges.

604

605 14. P6-7, L222-234: Please explain how all of these turbulence measurements will aid in  
606 understanding the physical mechanism(s) that contribute to cloud clearing processes.

607

608 Response: We discuss the actual results in the Results section and do not think an exhaustive  
609 discussion is needed here in the Methods section. Rather, we revise the first sentence of this  
610 paragraph:

611

612 “Ten Hz measurements of environmental parameters were used to estimate turbulent variance  
613 and covariance flux values, which may be relevant to the understanding of clearing formation  
614 and evolution based on past work (Crosbie et al., 2016).”

615

616 15. P6, L224: Why use a 2-km wide high pass filter? I imagine this is influenced by the aircraft  
617 speed? By the way, what is the typical aircraft speed?

618

619 Response: Typical aircraft speed is  $\sim 55 \text{ m s}^{-1}$ . We add a line about this now: “The typical  
620 aircraft speed was  $55 \text{ m s}^{-1}$ .”

621

622 We used a 2-km wide high pass filter for detrending signals, which is helpful for flux  
623 calculations. It is a common strategy employed in studies of this nature. A 2-km wide high-pass  
624 filter is conservatively picked to assure filtering of any signals that does not stem from MBL  
625 turbulent eddies (with the typical size being less than MBL depth). Given the aircraft speed of  
626  $\sim 55 \text{ m s}^{-1}$ , a 2-km wide filter translates to a filter with passband frequency of 0.0275 Hz. No  
627 change made for this comment.

628  
629 16. P7, L236: Is Fig. 2c supposed to show where the inversion sits?  
630  
631 Response: The sentence in question says the inversion base typically coincides with cloud top.  
632 Thus, Fig. 2c gives a representative view of where the inversion base sits. No change made for  
633 this comment.  
634  
635 17. P7, L236-238: Why use temperature rather than potential temperature?  
636  
637 Response: Both could work. We used temperature as has been done in past work. No change  
638 made for this comment.  
639  
640 18. P7, L238-240: This sentence is a bit confusing; please reword.  
641  
642 Response: Revised:  
643  
644 “Inversion top was defined as the highest altitude at which  $d\theta_l/dz$  exceeded  $0.1 \text{ K m}^{-1}$ , where  $\theta_l$  is  
645 liquid water potential temperature and  $z$  is altitude.”  
646  
647 19. P7, L247-248: Please reference the GBRT method for unfamiliar readers.  
648  
649 Response: We already did in the second sentence of the paragraph. But we now added another  
650 one to the first sentence if that helps:  
651  
652 “A Gradient Boosted Regression Tree (GBRT) model approach was implemented to investigate  
653 the impact of environmental parameters on the evolution of clearing events (Friedman 2001).”  
654  
655 20. P8, L284: How is this  $r^2$  threshold determined? Are the results sensitive to this choice?  
656  
657 Response: The  $r^2$  threshold was determined by choice. Sensitivity tests were done with different  
658 combinations of parameters and the general conclusions were preserved. We updated some text  
659 in the manuscript to address this comment:  
660  
661 “While  $PD$  plots are not flawless in capturing the influence of each variable in the model,  
662 especially if the input variables are strongly correlated, they provide useful information for  
663 interpretation of GBRT results (Friedman and Meulman 2003; Elith et al., 2008). To decrease the  
664 undesired influence of correlated variables on  $PD$  profiles, an arbitrary  $r^2$  threshold of 0.5 was  
665 used based on the linear regressions between prospective input parameters. For instance, there  
666 were three choices of air temperature (i.e., at 950, 850, and 700 hPa), but based on the  $r^2$  criterion,  
667 only one ( $T_{850}$ ) was used in the model to minimize the unwanted impact of dependent input  
668 parameters. Lower tropospheric stability ( $LTS$ : defined as the difference between the potential  
669 temperature of the free troposphere (700 hPa) and the surface) is the stability parameter that has  
670 been widely used as a key factor controlling the coverage of stratocumulus clouds. However, in  
671 this study, the effects of stability were examined by putting  $T_{850}$  and  $SST$  into the model without  
672 explicitly including  $LTS$ . The correlation between  $LTS$  and  $T_{850}$  prevented them to be used as input  
673 parameters simultaneously. Using  $T_{850}$  and  $SST$  instead of  $LTS$  is advantageous because the results

674 can be more informative by revealing different impacts of the two individual parameters on the  
675 model's output rather than just one parameter in the form of *LTS*. In addition, the mean sea level  
676 pressure anomaly (*MSLP<sub>anom</sub>*) was used as an input parameter, which was calculated in reference  
677 to the average values of *MSLP* for the summer months for the study period. In the end, the  
678 following 11 predicting variables from MERRA-2 were used as input parameters for the GBRT  
679 simulations, with data product details summarized in Table 1: *AOD*, *T<sub>850</sub>*, *q<sub>950</sub>*, *q<sub>850</sub>*, *q<sub>700</sub>*, *SST*,  
680 *MSLP<sub>anom</sub>*, *U<sub>850</sub>*, *V<sub>850</sub>*, *PBLH*, and  $\omega_{700}$ . It is important to note that the results of extensive sensitivity  
681 tests led to the selection of the set of parameters presented in this study. Also, these sensitivity  
682 tests confirmed that the general conclusions presented here were preserved regardless of using  
683 different sets of the input parameters.”

684  
685 21. P8, L298-299: What about the other MERRA-2 variables listed in Table 1 that are not listed  
686 here?

687  
688 Response: Well, they are listed still in Table 1 for completeness to walk readers through our  
689 process of analysis to reach the point of Lines 298-299. No harm in doing that in our opinion.

690  
691 22. P9, L322-323: Please reference a figure here.

692  
693 Response: Done. Additionally, we now differentiate between Figure 3a and 3b in the text.

694  
695 23. Figure 5: Because this plot is relatively straightforward, and only two sentences are written  
696 about it, I think that it makes more sense to add it to Figure 4, which also shows related variables  
697 as a function of time.

698  
699 Response: We added Figure 5 to the Supplement as adding it to Fig. 4 made this figure hard to  
700 read.

701  
702 24. P9, L354-356: What about near Point Conception? Are similar mechanisms responsible for  
703 the reduction of CF here?

704  
705 Response: We added the following text and added that point to Figure 6a:

706  
707 “Less pronounced is a centroid of reduced cloud fraction by Point Conception, where similar  
708 mechanisms may be at work.”

709  
710 25. P9, L356-361: Is it possible to plot low-level (maybe 100 m) wind arrows over the CF  
711 contours in Fig. 6 to support/refute this hypothesis?

712  
713 Response: Figure 8 shows winds clearly and it would be redundant in our view to put them in  
714 Figure 6 too.

715  
716 26. P9, L361-363: You mention southerly wind, but what about northerly wind along the  
717 coastline, which is much more common. Are expansion fan dynamics still present?

718  
719 Response: The sentences are revised accordingly:

720  
721 “The significance of these capes is discussed in many previous studies (Beardsley et al., 1987;  
722 Haack et al., 2001; Juliano et al., 2019a/b) pointing their ability to alter local dynamics, cloud  
723 depth, and various microphysical processes such as entrainment. Cloud thinning in the vicinity of  
724 the capes due to an expansion fan effect is reported for both northerly and southerly flow  
725 (Beardsley et al., 1987; Juliano et al., 2017).”

726  
727 27. Figure 7: In the difference plot in panel a, are there truly no regions where the SLP is lower  
728 in clearing cases?

729  
730 Response: This occurred because of the choice of spacing in the contour plot. Figure 7 has been  
731 updated to fix this issue.

732  
733 28. P10, L369: How might using nearly 2 times more non-clearing days influence your results?

734  
735 Response: It obviously provides more statistics and solidifies the non-clearing results. We do not  
736 expect this difference in days to affect the general conclusions.

737  
738 29. P10, L383: When you reference Fig. 8a, should this instead be a reference to Fig. 8b?

739  
740 Response: Correct, thanks. Change made.

741  
742 30. P10, L395-396: A few more citations would be nice for a statement that is “well  
743 documented”.

744  
745 Response: Sentence revised as the “well-documented” is unnecessary and seems to be a  
746 distraction.

747  
748 31. P11, L411-413: Can you speculate as to why you observe this?

749  
750 Response: This paragraph is revised to provide a potential explanation for the observed trend:

751  
752 “The changes in synoptic-scale conditions, including relocation/strengthening of the Pacific high,  
753 on clearing days in comparison to non-clearing days can alter large-scale subsidence. This is  
754 indeed confirmed in Fig. 8b using  $\omega_{700}$  as the proxy variable, with the strongest difference between  
755 clearing and non-clearing days (up to  $\sim 0.1 \text{ Pa s}^{-1}$ ) off the coast by Cape Blanco and Cape  
756 Mendocino and geographically coincident with where the sharpest gradients occur for *MSLP*  
757 between clearing and non-clearing cases (Fig. 6). It is interesting to note that the maximum *LTS*  
758 values coincide spatially with enhanced values of  $\omega_{700}$  on non-clearing days, in contrast to clearing  
759 days when the peak value of  $\omega_{700}$  is farther north from where *LTS* peaks (Fig. 8c). Consistent with  
760 the results presented here (Fig. 8b), modeling studies (Burk and Thompson 1996; Munoz and  
761 Garreaud 2005) reported enhanced subsidence for the entrance regions of the Chilean and  
762 California CLLJs in response to coastal features. These studies also reported the generation of a  
763 warm layer above the MBL due to coastal mechanisms especially downstream of coastal points  
764 and capes. This is also the case in this study where higher air temperature at 850 hPa was observed  
765 to the south of Cape Blanco and Cape Mendocino on clearing days (Fig. 5b). In addition, higher

766 *LTS* values on clearing days by up to ~2 K (Fig. 8c) are largely associated with the presence of  
767 warmer layer above the MBL south of Cape Blanco and Cape Mendocino. It is likely that reduced  
768 *SSTs* and greater subsidence contributed to generally higher *LTS* on clearing days versus non-  
769 clearing days (Fig. 8c). Other works have pointed to the connection between cooler *SSTs*, higher  
770 boundary layer cloud amount, and increased stability in the lower atmosphere (Norris and Leovy  
771 1994, Klein and Hartman 1993).”

772  
773 32. P11, L414-415: Why does PBLH exhibit this trend? Is this a well-known feature of the  
774 MBL offshore the western U.S.?

775  
776 Response: We edited this line to add a few references and to address the suspected reason for the  
777 observed trend in PBLH:

778  
779 “Another key environmental parameter related to MBL cloud coverage is the *PBLH*. Consistent  
780 with previous studies (Neiburger et al., 1961; Wood and Bretherton 2004), regardless of whether  
781 clearings were present, *PBLH* generally increases with distance from the coast (Fig. 8d), where  
782 warmer *SSTs* lead to deeper MBLs by weakening the inversion (Bretherton and Wyant 1997).  
783 The shallowing of the MBL near the California coast is also notable with enhanced gradients in  
784 clearing days. The aforementioned MBL shallowing is believed to be a crucial element in  
785 development of coastal jet off the California coast (Zemba and Friehe 1987; Parish 2000).  
786 Previous studies (Beardsley et al., 1987; Edwards et al., 2001; Parish 2000; Zuidema et al., 2009)  
787 also reported MBL height adjustment in the vicinity of coast due to hydraulic adaptation to  
788 coastal topography, thermally driven circulation, and geostrophic adjustment in the cross-coast  
789 direction in response to the contrast in surface heating between ocean and land. There is also a  
790 strong gradient in *PBLH* along the shoreline in the vicinity of Cape Blanco (Fig. 8d). While the  
791 presence of a similar gradient in *SST* (Fig. 8a) may partly explain the observed gradient in *PBLH*,  
792 coastally induced processes could also play a role.”

793  
794 33. P11, L467: Lower LWP values because the clouds are thinner, LWCs are lower, or both?

795  
796 Response: Presumably both. No change needed to text in our view.

797  
798 34. Section 3.3: Generally speaking, how do sample sizes influence the interpretation of these  
799 results? Many of the steep slopes shown in Fig. 12 occur at the low or high ends of the parameter  
800 spaces which is likely where the fewest number of samples lie. Are the results robust in these  
801 areas?

802  
803 Response: Added the following text:

804  
805 “Note that the 5<sup>th</sup>, 25<sup>th</sup>, 50<sup>th</sup>, 75<sup>th</sup>, and 95<sup>th</sup> percentiles of input parameter values are denoted in  
806 Figure 12 to caution that sharp slopes in the bottom and top 5<sup>th</sup> percentiles are based on few data  
807 points and that robust conclusions should not stem from those outer bounds.”

808  
809 35. P13, L514-516: Are the local changes in slope of the PD-T850 relationship important? For  
810 example, from 275 to 280 K, the slope is relatively small, but from 281 to 282 K, the slope is  
811 relatively large.

812  
813 Response: The best we thought to do was report our method of how these plots were generated  
814 and then leave it to readers to conclude using their own criteria how important local changes are.  
815 In our view, we are most interested in more macroscopic trends in these plots and also changes in  
816 signs of relationships.

817  
818 36. P13, L524-534: Please reference the various panels in this section to help the reader.

819 Response: Done.

820  
821  
822 37. P13, L540-543: Please provide a citation for this phenomenon. An example of previous  
823 work in this region may be found in Rahn et al. (2016, Observations of Large Wind Shear above  
824 the Marine Boundary Layer near Point Buchon, California, JAS).

825  
826 Response: Done:

827  
828 “Stronger northerly flow is associated with offshore flow of dry and warm air that can reside  
829 above the cloud top, which can dissipate the cloud layer after entrainment and via enhanced  
830 shearing (via Kelvin-Helmholtz instability) and mixing of cloudy parcels with warm and dry air  
831 in the FT (e.g., Rahn et al., 2016). As will be shown later, aircraft data showed that typical wind  
832 speeds parallel to clear-cloudy interfaces were near or greater than  $10 \text{ m s}^{-1}$  (Fig. 12).”

833  
834 38. P14, L557-558: A negative U850 promoting cloud clearing makes sense due to the offshore  
835 flow component, but can you hypothesize as to why strong positive U850 values also promote  
836 cloud clearing?

837  
838 Response: We are not sure and make this explicit:

839  
840 “Clearing growth due to negative zonal winds can be explained by the offshore flow component,  
841 however, the reason for growth during periods of positive zonal winds is unclear.”

842  
843 39. P14, L566: Might these vertical motions also induce dynamical circulations and thereby  
844 influence shear/turbulence/entrainment processes near cloud top?

845  
846 Response: Maybe so. We add text to give this idea some attention in the draft:

847  
848 “Vertical motions represented by the  $\omega_{700}$  parameter could also induce dynamical circulations  
849 affecting cloud top processes such as shear and entrainment.”

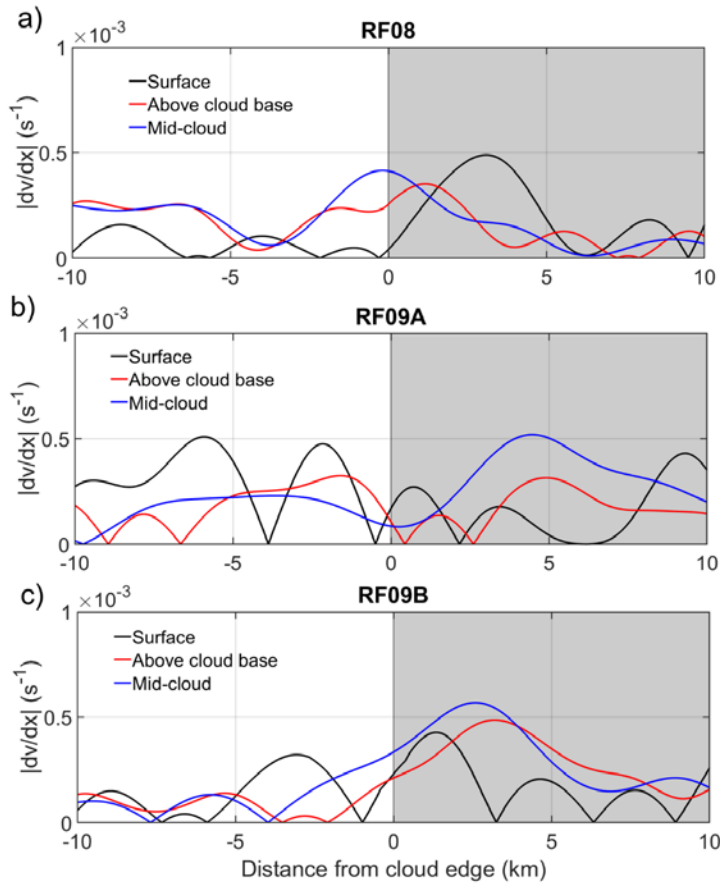
850  
851 40. P15, L592: Specific or relative humidity?

852  
853 Response: Made it clear it is “specific”.

854  
855 41. P15, L614-627: I like this portion of the analysis, and the topic of horizontal wind shear is  
856 one that probably does not receive enough attention. I think that perhaps a line plot showing how  
857 the horizontal shear changes with distance for each of the vertical levels may be very useful.



858  
859 Response:  
860 We calculated horizontal shear for constant level legs and displayed it in SI file. Additionally,  
861 the paragraph has been updated accordingly:  
862  
863 “To extend upon the possibility of shearing effects, absolute changes in  $v$  ( $/v$ ) were calculated for  
864 level legs performed at the clear-cloudy border for the three research flights (Table 2). For  
865 consistency, these calculations were based on level legs of a constant length of  $\sim 40$  km with  
866 relatively equal spacing on both sides of the clear-cloudy border.  $/v$  was calculated by multiplying  
867 40 km by the slope of the linear fit of  $v$  versus distance from cloud edge, where negative (positive)  
868  $x$  values represent distance away from the edge on the clear (cloud) side. The results reveal that  
869 the horizontal wind shear was strongest somewhere between mid-cloud and cloud top altitudes,  
870 with the lowest values at the FT level. The lowest values in the MBL were observed in the surface  
871 legs. This can be attributed to turbulent transport of the momentum (Zemba and Friehe 1987) to  
872 the surface and the consequent drop in CLLJ wind speeds in the clear column. In addition, Fig. S7  
873 shows absolute horizontal shear ( $|dv/dx|$ ) as a function of distance from the cloud boundary for the  
874 parallel component of horizontal wind speed. Horizontal shear profiles for all research flights (Fig.  
875 S7) are slightly noisy especially at the surface legs, but they show the presence of the greatest  
876 horizontal wind gradient within 5 km length away from clear-cloudy edge. Shear at the clear-  
877 cloudy edge, especially at cloud levels, can support clearing growth through enhancing the mixing  
878 of cloudy and clear air. Crosbie et al. (2016) also showed using the case of NiCE RF19 that that  
879 mixing of cloudy air with adjacent clear air can be an important contributor to cloud erosion and  
880 thus expansion of clearings. To probe deeper into the clearing cases, the subsequent discussion  
881 compares vertically-resolved data on both sides of the clear-cloudy border based on soundings and  
882 level legs.”



883 **Figure S7.** Absolute variations in horizontal shear as a function of distance from the cloud  
 884 boundary for the parallel component of horizontal wind speed for three case research flights: a)  
 885 RF08, b) RF09A, and c) RF09B. These variations were shown only for constant altitude legs  
 886 (surface, above cloud base, and mid-cloud legs). Cloudy columns are highlighted in grey.  
 887  
 888

889 42. P16, L648-650: I do not understand this sentence; please reword.

890  
 891 Response: We revised the sentence:

892  
 893 “The wind maximum in the clearing also enhanced moisture advection, which counteracted the  
 894 accumulation of moisture caused by mixing induced by vertical shear.”

895  
 896 43. P16, L660: How is the cloud base rain rate determined?  
 897

898 Response: Text added:

899

900 “Cloud base rain rate was quantified using the size distributions of drizzle drop ( $D_p > 40 \mu\text{m}$ )  
901 obtained from CIP in the bottom third of clouds along with documented relationships between  
902 fall velocity and drop size (Wood 2005b).”

903

904 44. P16-17, L677-681: Are you able to hypothesize why, in all three flights, surface PCASP  
905 concentrations are higher on the cloudy side even though the surface wind speeds are higher on  
906 the clear side? Is it possible that drizzle drops evaporate after the wet scavenging processes and  
907 therefore concentrate aerosol near the surface, whereas aerosol are well-mixed in the MBL on  
908 the clear side? If available, vertical profiles may help here.

909

910 Response: We went ahead and made vertical profiles as shown in the new Figure S8. It is too  
911 difficult to reach the speculation above with a high level of confidence provided by the reviewer  
912 based on the available dataset in our opinion. Entrainment of free tropospheric aerosol particles  
913 is likely a possible explanation too. We added the following text:

914

915 “Figure S8 shows vertical profiles of aerosol concentrations on both sides of the clearing border,  
916 highlighting differences above cloud top level especially in RF09A and RF09B with higher values  
917 in the cloudy column. Higher aerosol concentrations were also observed in the cloud column in  
918 the sub-cloud layer even though surface wind speeds were always higher in the clear column for  
919 all three flights. Surface winds and thus sea spray production do not exclusively influence the  
920 aerosol concentrations. A likely explanation of higher concentrations in the MBL in the cloudy  
921 column is that there could be entrainment of more polluted free tropospheric aerosol as has been  
922 reported to be a common occurrence during the FASE flights (e.g., Mardi et al., 2019). As also  
923 reported during FASE, there can be sub-cloud evaporation of drizzle resulting in droplet residual  
924 particles that contribute to the aerosol concentration budget in the cloudy column (Dadashazar et  
925 al., 2018).”

926

927

928

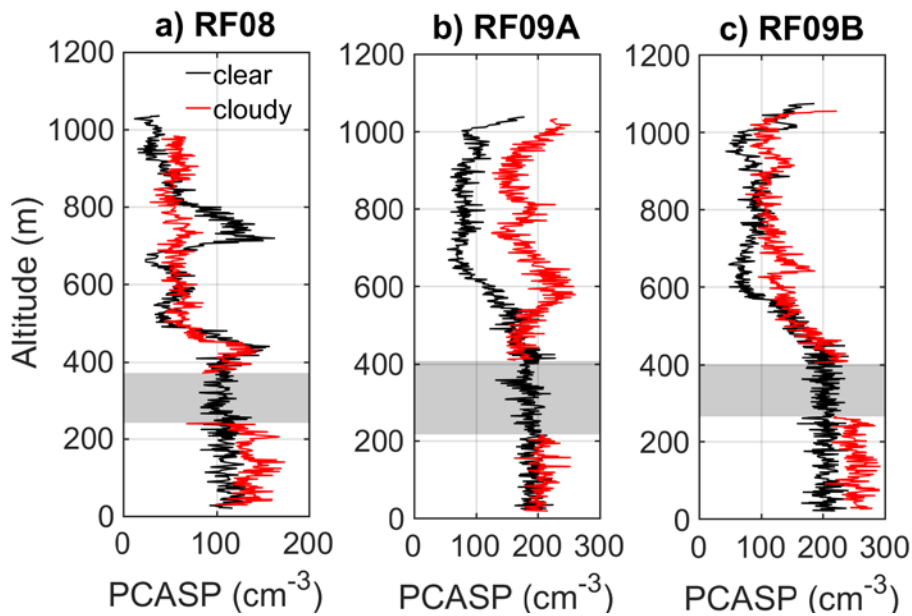


**Figure S8.** PCASP profiles obtained from soundings performed in clear and cloudy columns for three case research flights: a) RF08, b) RF09A, and c) RF09B. The altitude range where the cloud deck was present is highlighted in grey. PCASP data are unreliable in cloud due to droplet shatter artifacts and thus not shown.

45. P17, L683: Do you mean stronger gradients in horizontal wind speed?

Response: Yes, that is correct. Text revised.

“Stronger horizontal wind speed gradients,…”

46. P17, L683-685: What about the role of positive (cyclonic) vorticity that is generated by this horizontal shear? Could this influence cloud properties near the cloudy-clear interface?

Response: We suppose that is a possibility but we felt it was not necessary to address this in the text to avoid having too many speculations without unambiguous support.

47. P18, L749-765: I think that in order for the authors’ to argue whether buoyancy or shear production of turbulence is more important, they should calculate the terms according to the TKE equation (e.g., see Eq. 5.1a in Stull, An Introduction to Boundary Layer Meteorology, 1988).

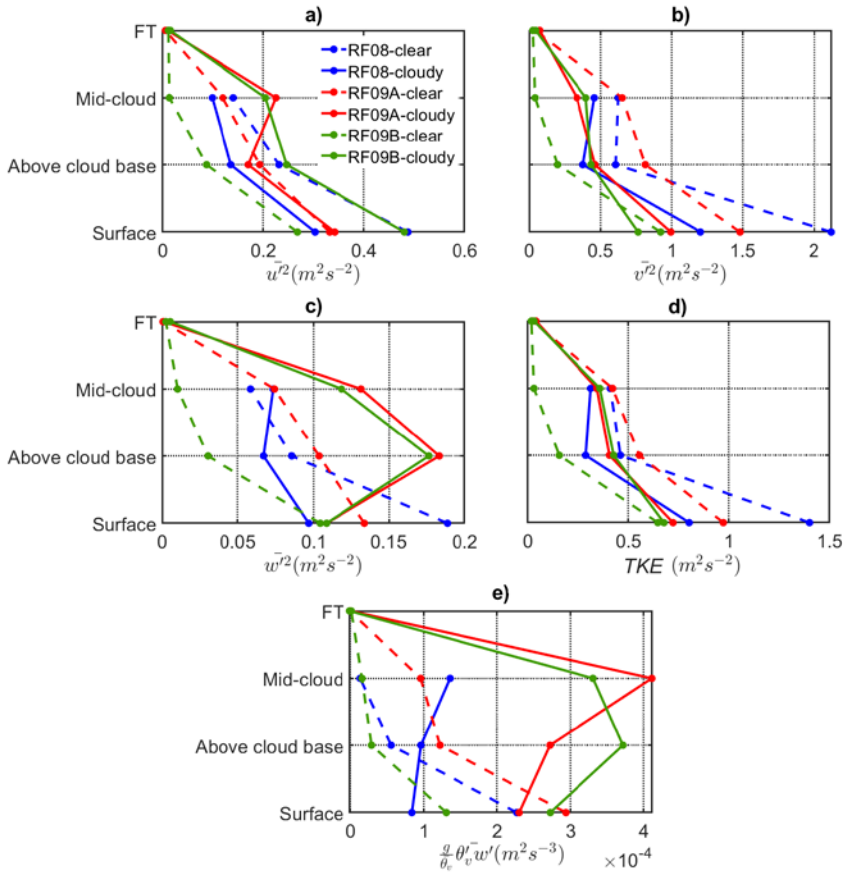
953 Response: This was in fact attempted already but the data looked noisy and inconclusive; this is  
954 mainly a limitation of the aircraft data. We do not feel this is really necessary to respond to as a  
955 result.

956  
957 48. P18, L754-755: Adding vertical profiles of TKE would be very useful.

958  
959 Response: The vertical profiles of TKE have been added to Fig. 13. We also updated the text as  
960 follows:

961  
962 “Profiles of  $\overline{u'^2}$  and  $\overline{v'^2}$  exhibited downward trends with increasing altitude for RF09A and  
963 RF09B, in general agreement with the findings for RF08. One contrasting aspect was the  
964 comparison of  $\overline{v'^2}$  between clear and cloudy columns, which mirrored RF08 during RF09A, while  
965 in RF09B, the values of  $\overline{v'^2}$  for the clear side were substantially lower. In addition,  $\overline{w'^2}$  profiles  
966 during RF09A and RF09B are substantially enhanced in the cloudy column as compared to RF08,  
967 with maxima in the cloud layer. There is an accompanying increase in the buoyancy flux for these  
968 profiles suggestive of a more significant contribution of buoyancy to *TKE* production (Fig. 13e).

969 Although more subtle,  $\overline{u'^2}$  values also showed an increase in the cloudy column of RF09A and  
970 RF09B relative to the clear column, also supportive of the role of buoyancy in these cases. In  
971 addition, *TKE* profiles (Fig. 13d) were largely influenced by variances in the horizontal component  
972 of wind speed ( $\overline{u'^2}$  and  $\overline{v'^2}$ ) which led to overall greater *TKE* values in the clear column except  
973 for RF09B.”  
974



975 **Figure 13.** Selected dynamic parameters for the clear (dash lines) and cloudy (solid lines) parts of  
 976 the legs performed at different altitudes for three FASE case research flights: Panels a-c) exhibit  
 977 squared average velocity fluctuations of wind speeds components ( $u$  and  $v$  horizontal components,  
 978  $w$  vertical component). Horizontal wind speeds are decomposed into two components, ( $u$ )  
 979 perpendicular and ( $v$ ) parallel, relative to the cloud edge. Panels d) and e) display turbulent kinetic  
 980 energy and buoyancy flux profiles, respectively, for the three flights.  
 981  
 982

983 49. P18, L759: What do you mean by “stabilizing effect”?

984  
 985 Response: Those words were removed.

986  
 987 50. P19, L803-805: Can new remote sensing platforms, such as GOES-16/17, help with the  
 988 diurnal analysis of cloud properties?  
 989

990 Response: Yes. Text added:

991  
992 “More data such as those provided by GOES platforms can help understand processes occurring  
993 at the microscale that scale up to more climatologically relevant scales.”  
994  
995 Grammatical/wording recommendations:  
996 1. P6, L198: Please change “Of the relevance to this study” to “Of relevance to this study”.  
997  
998 [Response: Edited.](#)  
999  
1000 2. P7, L254: Please change “or each of the 306 events.” to “for each of the 306 days.”.  
1001  
1002 [Response: Fixed.](#)  
1003  
1004 3. P8, L313: Please change “between 2009 and 2018” to “from 2009 through 2018”.  
1005  
1006 [Response: Fixed.](#)  
1007  
1008 4. P10, L366: Please change “Large-scale characteristics of a dynamic and thermodynamic  
1009 nature were contrasted” to “Large-scale dynamic and thermodynamic characteristics were  
1010 contrasted”.  
1011  
1012 [Response: Edited.](#)  
1013  
1014 5. P10, L401: Please change “likely contribute” to “likely contributes”.  
1015  
1016 [Response: Edited.](#)  
1017 6. P11, L410: Please change “geographical coincident” to “geographically coincident”.  
1018  
1019 [Response: Edited.](#)  
1020  
1021 7. P12, L494: Consider changing “GBRT model to model clearing” to “GBRT model to  
1022 reproduce clearing”.  
1023  
1024 [Response: Changed.](#)  
1025  
1026 8. P12, L500: Please remove “partial dependence” as this acronym has already been defined.  
1027  
1028 [Response: Edited.](#)  
1029  
1030 9. P16, L656: Please change “lesser effect” to “reduced effect”.  
1031  
1032 [Response: Edited.](#)  
1033  
1034 10. P19, L780-781: Consider changing “clearings visible from space” to “clearings as suggested  
1035 by satellite retrievals”.  
1036

1037 [Response: Changed.](#)

1038

1039 11. P19, L782: Please change “centroid of clearings is centered” to “centroid of clearings is  
1040 located”

1041

1042 [Response: Edited.](#)

1043

1044 12. P19, L808: Please change “sea spray fluxes, which subsequently can impact clouds” to “sea  
1045 spray fluxes and can subsequently impact clouds”.

1046

1047 [Response: Edited.](#)

1048

1049



1050 **Stratocumulus Cloud Clearings: Statistics from Satellites, Reanalysis Models, and Airborne**  
1051 **Measurements**

1052  
1053 Hossein Dadashazar<sup>1</sup>, Ewan Crosbie<sup>2,3</sup>, Mohammad S. Majdi<sup>4</sup>, Milad Panahi<sup>5</sup>, Mohammad A.  
1054 Moghaddam<sup>5</sup>, Ali Behrangi<sup>5</sup>, Michael Brunke<sup>5</sup>, Xubin Zeng<sup>5</sup>, Haflidi H. Jonsson<sup>6</sup>, Armin  
1055 Sorooshian<sup>1,5\*</sup>

1056  
1057 <sup>1</sup>Department of Chemical and Environmental Engineering, University of Arizona, Tucson, AZ,  
1058 USA

1059 <sup>2</sup>Science Systems and Applications, Inc., Hampton, VA, USA

1060 <sup>3</sup>NASA Langley Research Center, Hampton, VA, USA

1061 <sup>4</sup>Department of Electrical and Computer Engineering, University of Arizona, Tucson, AZ, USA

1062 <sup>5</sup>Department of Hydrology and Atmospheric Sciences, University of Arizona, Tucson, AZ, USA

1063 <sup>6</sup>Naval Postgraduate School, Monterey, CA, USA

1064  
1065 \*Corresponding author: armin@email.arizona.edu

1066

1067 Abstract

1068 This study provides a detailed characterization of stratocumulus clearings off the U.S. West  
1069 Coast using remote sensing, reanalysis, and airborne in situ data. Ten years (2009-2018) of  
1070 Geostationary Operational Environmental Satellite (GOES) imagery data are used to quantify the  
1071 monthly frequency, growth rate of total area (*GR<sub>Area</sub>*), and dimensional characteristics of 306 total  
1072 clearings. While there is interannual variability, the summer (winter) months experienced the most  
1073 (least) clearing events with the lowest cloud fractions being along coastal topographical features  
1074 along the central to northern coast of California including especially just south of Cape Mendocino  
1075 and Cape Blanco. From 09:00 to 18:00 (PST), the median length, width, and area of clearings  
1076 increased from 680 to 1231 km, 193 to 443 km, and ~67,000 to ~250,000 km<sup>2</sup>, respectively.  
1077 Machine learning was applied to identify the most influential factors governing the *GR<sub>Area</sub>* of  
1078 clearings between 09:00-12:00 PST, which is the time frame of most rapid clearing expansion.  
1079 The results from Gradient Boosted Regression Tree (GBRT) modeling revealed that air  
1080 temperature at 850 hPa (*T<sub>850</sub>*), specific humidity at 950 hPa (*q<sub>950</sub>*), sea surface temperature (*SST*),  
1081 and meridional wind speed at 850 hPa (*V<sub>850</sub>* anomaly in mean sea level pressure (*MSLP<sub>anom</sub>*) were  
1082 probably most impactful in enhancing *GR<sub>Area</sub>* using two scoring schemes. Clearings have  
1083 distinguishing features such as an enhanced Pacific high shifted more towards northern California,  
1084 offshore air that is warm and dry, stronger coastal surface winds, enhanced lower tropospheric  
1085 static stability, and increased subsidence. Although clearings are associated obviously with  
1086 reduced cloud fraction where they reside, the domain-averaged cloud albedo was actually slightly  
1087 higher on clearing days as compared to non-clearing days. To validate speculated processes linking  
1088 environmental parameters to clearing growth rates based on satellite and reanalysis data, airborne  
1089 data from three case flights were examined. Measurements were compared on both sides of the  
1090 clear-cloudy border of clearings at multiple altitudes in the boundary layer and free troposphere,  
1091 with results helping to support links suggested by this study's model simulations. More  
1092 specifically, airborne data revealed the influence of the coastal low-level jet and extensive  
1093 horizontal shear at cloud-relevant altitudes that promoted mixing between clear and cloudy air.  
1094 Vertical profile data provide support for warm and dry air in the free troposphere additionally  
1095 promoting expansion of clearings. Airborne data revealed greater evidence of sea salt in clouds on  
1096 clearing days, pointing to a possible role for, or simply the presence of, this aerosol type in clearing  
1097 areas coincident with stronger coastal winds.

1098  
1099

Formatted: Font: Italic

Formatted: Font: Italic

Formatted: Font: Italic

Formatted: Font: Italic

Formatted: Font: Italic

Formatted: Font: Italic

1100 **1. Introduction**

1101 Stratocumulus clouds play an important role in both global and regional climate systems.  
1102 Stratocumulus clouds are the dominant cloud type over marine environments based on annual  
1103 mean of area covered (Warren et al., 1986; Hahn and Warren, 2007). In coastal areas, these clouds  
1104 can impact industries such as agriculture, transportation (e.g., aviation), military operations,  
1105 coastal ecology, and biogeochemical cycles of nutrients. Stratocumulus clouds also play an  
1106 important role in the global radiation budget due to their high albedo contrast with the underlying  
1107 ocean surface- ([Hartmann and Short, 1980](#); [Herman et al., 1980](#); [Stephens and Greenwald, 1991](#)).  
1108 Challenges in accurately simulating the presence and properties of stratocumulus clouds include  
1109 the difficulty in separating the influence of microphysical and dynamical factors and the existence  
1110 of multiple feedbacks in cloud systems (Brunke et al., 2019). Therefore, accurate characterization  
1111 of cloud formation and evolution is critical.

1112 Numerous studies have examined the behavior of clouds off the United States (U.S.) West  
1113 Coast (e.g., Coakley et al., 2000; Durkee et al., 2000; Stevens et al., 2003; Lu et al. 2009; Painemal  
1114 and Minnis, 2012; Modini et al., 2015; Sanchez et al., 2016). The persistence of the cloud deck in  
1115 this region, especially during the summer, makes it a key location for studying marine  
1116 stratocumulus clouds. Furthermore, the prevalence of freshly-emitted aerosols from ships provides  
1117 an optimal setting for field measurements of aerosol-cloud-precipitation interactions because of  
1118 the relative ease of finding strong aerosol perturbations, from which cloud responses can be  
1119 robustly quantified (e.g., Russell et al., 2013). Over the decades of research conducted in the  
1120 aforementioned study region and two other major stratocumulus regions (Southeast Pacific Ocean  
1121 off the Chile-Peru coasts and Southeast Atlantic Ocean off the Namibia-Angola coasts), one  
1122 feature that has not received sufficient attention is large scale stratocumulus clearings that are  
1123 easily observed in satellite imagery and often exceed 100 km in width (Fig. 1). Perhaps the most  
1124 obvious impact of these clearings is the change in albedo as an otherwise cloudy area would be  
1125 highly reflective. Improving understanding of factors governing clearings has implications for  
1126 modeling of marine boundary layer clouds and for operational forecasting of weather and fog along  
1127 coastlines.

1128 Previous studies have documented the existence of large scale cloud clearings off the U.S.  
1129 West Coast (e.g., Kloesel, 1992). During the 2013 Nucleation in Cloud Experiment (NiCE), three  
1130 case study flights with the Center for Interdisciplinary Remotely-Piloted Aircraft Studies  
1131 (CIRPAS) Twin Otter examined clearings off the California coast, with a focus on diurnal behavior  
1132 and contrasting aerosol and thermodynamic properties across the cloud-clearing interface (Crosbie  
1133 et al., 2016). Based on a multi-day event, they showed that a clearing expanded during the day and  
1134 contracted at night towards the coast with oscillations between growth and decay over the multi-  
1135 day clearing lifetime. They observed that small scale processes (~1 km) at the clearing-cloud  
1136 border are influential in edge dynamics that likely upscale to more climatologically influential  
1137 scales, which is why reanalysis data cannot accurately replicate the spatial profile of cloud fraction  
1138 ([CF](#)) and cloud liquid water path ([LWP](#)) when compared to satellite data. One of their three events  
1139 was associated with a so-called “southerly surge”, also referred to as a coastally-trapped  
1140 disturbance (CTD). CTD events were recently characterized off the U.S. West Coast by Juliano et  
1141 al. (2019a,b). Clearing events have been examined over the southeast Atlantic Ocean with the  
1142 catalyst for cloud erosion shown to be atmospheric gravity waves (Yuter et al., 2018). While these  
1143 aforementioned studies have explained details associated with clearings in different coastal  
1144 regions, there are many unanswered questions remaining and a need for more statistics associated  
1145 with clearings to build more robust conclusions.

1146 The goal of this work is to build upon cloud clearing studies over the U.S. West Coast to  
1147 provide a more comprehensive analysis using the synergy of data from satellite remote sensors,  
1148 reanalysis products, and airborne in-situ measurements. We first examine a decade of satellite data  
1149 to report on statistics associated with the temporal and spatial characteristics of clearings. These  
1150 characteristics are then studied in conjunction with environmental properties from reanalysis  
1151 products and machine learning simulations to identify factors potentially contributing to the  
1152 formation and evolution of clearings. Lastly, airborne in situ data are used to validate findings  
1153 from the aforementioned analyses and to gain more detailed insight into specific events that  
1154 otherwise would not be possible with reanalysis and satellite products. The most significant  
1155 implications of our results are linked to modeling of fog and boundary layer clouds, with major  
1156 implications for a range of societal and environmental issues such as climate, military operations,  
1157 transportation, and coastal ecology.  
1158

## 1159 2. Experimental Methods

### 1160 2.1 Satellite Datasets

1161 Long-term statistics associated with clearings were obtained using Geostationary  
1162 Operational Environmental Satellite (GOES) visible band (~0.6  $\mu\text{m}$ ) images. Visual imagery data  
1163 were obtained from GOES-11 for 2009 through 2011 and from GOES-15 between 2012 and 2018  
1164 (data products summarized in Table 1). Images were analyzed for the spatial domain bounded by  
1165 115°-135° W and 30°-50° N. The following steps led to the identification of individual clearings  
1166 using GOES images, of which a total of 306 were identified between 2009 and 2018:  
1167

- 1168 (ii) GOES-11 and GOES-15 visible images were obtained from the National Oceanic and  
1169 Atmospheric Administration (NOAA) Comprehensive Large Array-data Stewardship  
1170 System (CLASS) database (<http://www.class.noaa.gov>).
- 1171 (iii) Each day's sequence of GOES images were visually inspected to identify if a clearing event  
1172 was present. This involved utilizing the following general guidelines: (i) there had to be  
1173 sufficient cloud surrounding the clearing area that the clearing's borders could be  
1174 approximately identified, which excluded cases with highly broken cloud deck; (ii)  
1175 clearings that were not connected to land between 30°-50° N in any of daily images were  
1176 excluded; (iii) days with the cloud deck completely detached from the coast between 30°-  
1177 50° N were not considered; and (iv) only clearings with a maximum daily area of greater  
1178 than 15,000 km<sup>2</sup> (which translates to a clearing length on the order of 100 km) were  
1179 considered. Consequently, the statistics presented in Section 3.1.1 represent a lower limit  
1180 of clearing occurrence in the study region. However, it is expected that the qualitative  
1181 trends discussed in Section 3.1.1 are representative of clearing behavior in the study region.
- 1182 (iv) For each clearing event, four images were selected to both quantify clearing properties and  
1183 characterize diurnal variability: (i) Image 1 after sunrise, between 14:15 UTC (7:15 Pacific  
1184 Standard Time (PST)) and 16:45 UTC (09:45 PST) with a median at ~16:00 UTC (09:00  
1185 PST); (ii) Image 2 at a time relevant to the *Moderate* Resolution Imaging  
1186 Spectroradiometer (MODIS) Terra overpass over the study region, between 18:45 UTC  
1187 (11:45 PST) and 20:45 UTC (13:45 PST) with a median at ~19:00 UTC (~12:00 PST); (iii)  
1188 Image 3 at a time relevant to the MODIS Aqua overpass over the study region, ranging  
1189 from 19:45 UTC (12:45 PST) to 22:15 UTC (15:15 PST) with a median at ~22:00 UTC  
1190 (~15:00 PST); and (iv) Image 4 before sunset, ranging from 22:45 UTC (15:45 PST) to

1191 02:15 UTC (19:15 PST) with a median at ~01:00 UTC (~18:00 PST). For the purposes of  
1192 subsequent discussion, local times (PST) will be used.

1193 (v) A custom-made cloud mask algorithm was applied consisting of the following steps: (i)  
1194 each visible image was converted to an 8-bit integer gray-scale image with values assigned  
1195 to each pixel ranging from 0 (black) to 255 (white); (ii) continental areas were masked  
1196 from the analysis (i.e., green regions in Fig. 1), meaning that their values were not included  
1197 in subsequent steps; (iii) a histogram of values for all pixels over the ocean was calculated  
1198 for each image obtained in the previous step and then Otsu's method (Otsu 1979) was  
1199 applied on the obtained histogram to compute a global threshold to categorize each pixel  
1200 as either clear or cloudy; (iv) a MATLAB image processing toolbox was used to extract  
1201 the clearing as an object, including the pixels at the clearing-cloud border and pixels inside  
1202 the clearing; (v) information contained within the clear pixels was then used to estimate  
1203 clearing dimensions such as width, length, area, and centroid for the spatial domain  
1204 bordered by 115°-135° W and 30°-50° N; and (vi) a MATLAB application was written to  
1205 automate all of the aforementioned steps to process data for a decade (2009-2018).  
1206

1207 Data were used from the MODIS on the Terra and Aqua satellites to characterize cloud ~~and~~  
1208 ~~aerosol~~ properties on clearing and non-clearing days in the spatial domain of analysis defined  
1209 above. Daily Level 3 ~~Collection 6.1~~ data (Hubanks et al., 2019) with spatial resolution 1°×1° were  
1210 downloaded from the LAADS DAAC distribution system  
1211 (<https://ladsweb.modaps.eosdis.nasa.gov/>). The key daytime parameters (Table 1) retrieved for  
1212 this study relevant to liquid clouds included the following, ~~which were retrieved at 2.1 μm and~~  
1213 ~~selected based on their importance for marine boundary layer (MBL) cloud fraction (studies: CF)~~  
1214 obtained from the MODIS cloud mask algorithm (Platnick et al., 2003), cloud optical thickness  
1215 ( $\tau$ ), ~~cloud liquid water path (LWP)~~, and cloud droplet effective radius ( $r_e$ ). Detailed information  
1216 about these MODIS products is described elsewhere (Platnick et al., 2003; Platnick et al., 2017;  
1217 Hubanks et al., 2019).

1218 Although MODIS Level 3 data parameters do not include cloud droplet number  
1219 concentration ( $N_d$ ), previous studies estimated  $N_d$  using retrievals of  $\tau$  and  $r_e$  with assumptions  
1220 (Bennartz, 2007; Painemal and Zuidema, 2010; McCoy et al., 2017). We use the following  
1221 equation from Painemal and Zuidema (2010) to estimate  $N_d$ :  
1222

$$1223 N_d = \frac{(\Gamma_{ad})^{\frac{1}{2}}}{k} \frac{10^{\frac{1}{2}}}{4\pi\rho_w^{\frac{1}{2}}} \frac{\tau^{\frac{1}{2}}}{r_e^{\frac{5}{2}}} \quad (1)$$

1224 where  $\rho_w$  is the density of liquid water,  $\Gamma_{ad}$  is the adiabatic lapse rate of liquid water content  
1225 ( $LWC$ ), and the parameter  $k$  is representative of droplet spectral shape as the cube of the ratio  
1226 between the volume mean radius and the effective radius. ~~While Painemal~~  $\Gamma_{ad}$  is a function of  
1227 ~~temperature and Zuidema (2010) pressure (Albrecht et al., 1990). In this study, cloud top~~  
1228 ~~temperature and pressure, provided by MODIS, are used a~~  $\Gamma_{ad}$  value equal to  $2.0 \times 10^{-4} \text{ g m}^{-4}$  to  
1229 estimate  $N_d$  for  $\Gamma_{ad}$ . ~~following the southeast Pacific region, we use the average value of~~  $\Gamma_{ad} =$   
1230  $2.3 \times 10^{-4} \text{ g m}^{-4}$  ~~reported by methodology described in Braun et al. (2018) for the northeast~~  
1231 ~~Pacific). A constant value of 0.8 (Martin et al. 1994) is assigned to  $k$  in Equation 1.~~

1232 ~~Similar to our previous study on clearings (Crosbie et al., 2016), cloud top albedo ( $A$ ) was~~  
1233 ~~quantified using  $\tau$  in the following relationship (Lacis and Hansen 1974):~~  
1234

Formatted: Font: Italic

Formatted: Font: Italic

Formatted: Font: Italic

Formatted: Font: Italic

Formatted: Font: Italic

Formatted: Font: Italic

Formatted: Font: Italic

Formatted: Font: Italic

Formatted: Font: Italic

Formatted: Font: Italic

Formatted: Font: Italic

Formatted: Font: Italic

1235  $A = \frac{\tau}{\tau+7.7}$  (2)

1236

## 1237 2.2 Reanalysis Data

1238 Various products from Modern-Era Retrospective analysis for Research and Applications,  
1239 Version 2 (MERRA-2; Gelaro et al., 2017) were used to gain insight into possible mechanisms  
1240 influencing the formation and evolution of clearings off the U.S. West Coast. MERRA-2 data were  
1241 downloaded from the NASA Goddard Earth Sciences Data and Information Services Center (GES  
1242 DISC; <https://disc.gsfc.nasa.gov/>). Table 1 summarizes MERRA-2 parameters used in this work,  
1243 including detailed information such as their product identifier and temporal resolution. -The  
1244 parameters were chosen based on their ability to provide a sufficient view of atmospheric  
1245 conditions in which MBL clouds form, evolve, and dissipate. Various vertical levels were used for  
1246 some MERRA-2 products as a way of obtaining representative information for different layers of  
1247 the MBL and free troposphere (FT). Of note is that the MERRA-2 aerosol reanalysis relies on the  
1248 GEOS-5 Goddard Aerosol Assimilation System (Bucharad et al., 2015) for which the Goddard  
1249 Chemistry, Aerosol, Radiation, and Transport (GOCART) model (Chin et al., 2002) simulates 15  
1250 externally mixed aerosol tracers including sulfate, dust (five size bins), sea salt (five size bins),  
1251 and hydrophobic and hydrophilic black carbon and organic carbon. Of relevance to this study,  
1252 GOCART applies wind-speed dependent emissions for sea salt. Furthermore, the dominant  
1253 removal mechanisms for aerosols include gravitational settling, dry deposition, and wet  
1254 scavenging.

1255

1256

## 1257 2.3 Airborne In-Situ Data

1258 Motivated by the three case study research flights (RFs) probing clearings during the NiCE  
1259 campaign (Crosbie et al., 2016), the Fog and Stratocumulus Evolution Experiment (FASE) was  
1260 carried out with nearly the same payload on the Center for Interdisciplinary Remotely-Piloted  
1261 Aircraft Studies (CIRPAS) Twin Otter between July and August 2016 (Sorooshian et al., 2018).  
1262 Data were used from three case RFs examining clearings: RF08 on 2 August 2016, and  
1263 RF09A/RF09B on 3 August 2016. The back-to-back flights on 3 August afforded an opportunity  
1264 to examine the evolution of clearing properties at the clear-cloudy interface over a span of a few  
1265 hours. Figure 2 shows GOES imagery and the flight pattern for RF09A, which is representative of  
1266 the other two shown in Figs. S1-S2. The same flight strategy from NiCE (Crosbie et al., 2016) was  
1267 used in the FASE RFs and included the following set of maneuvers (Fig. 2c): (i) spiral profiles on  
1268 both sides of the clear-cloudy interface; (ii) level legs extending on both sides of the clear-cloudy  
1269 interface near the ocean surface (~30 m; called “surface leg”), above cloud base, and mid-cloud;  
1270 (iii) a series of sawtooth maneuvers up and down between ~60 m below and above the cloud top  
1271 on both sides of the clear-cloudy interface; and a (iv) level leg in the ~~free troposphere (FT)~~ at ~1  
1272 km altitude. The typical aircraft speed was 55 m s<sup>-1</sup>.

1273 Commonly used instruments provided dynamic, thermodynamic, and navigational data  
1274 (Crosbie et al., 2016; Dadashazar et al., 2017; Sorooshian et al., 2018). ~~Of the~~ relevance to this  
1275 study are 10 Hz measurements of wind speeds, air temperature, and humidity. Setra pressure  
1276 transducers attached to a five-hole gust probe radome provided three components of wind speeds  
1277 after correction for aircraft motion, which was obtained by a C-MIGITS-III GPS/INS system.  
1278 Ambient air temperature was measured by a Rosemount Model 102 total temperature sensor. Also,

1279 humidity data were collected with an EdgeTech Vigilant chilled mirror hygrometer (EdgeTech  
1280 Instruments, Inc.).

1281 Cloud micro/macrophysical parameters were measured at 1 Hz with various instruments.  
1282 Size distributions of cloud droplets and rain droplets were characterized using the Forward  
1283 Scattering Spectrometer Probe (FSSP;  $D_p \sim 2\text{--}45 \mu\text{m}$ ) and Cloud Imaging Probe (CIP;  $D_p \sim 25\text{--}$   
1284  $1600 \mu\text{m}$ ). Cloud base rain rate was quantified using the size distributions of drizzle drop ( $D_p > 40$   
1285  $\mu\text{m}$ ) obtained from CIP in the bottom third of clouds along with documented relationships between  
1286 fall velocity and drop size (Wood 2005a). *LWC* data were obtained using a PVM-100 (Gerber et  
1287 al., 1994), which were vertically integrated during sounding profiles to quantify cloud *LWP*.  
1288 Aerosol concentration data are reported here from the passive cavity aerosol spectrometer probe  
1289 (PCASP;  $D_p \sim 0.11\text{--}3.4 \mu\text{m}$ ; Particle Measuring Systems (PMS), Inc.; modified by Droplet  
1290 Measurement Technologies, Inc.) at 1 Hz time resolution. Cloud water composition data were  
1291 obtained using a modified Mohnen slotted-rod collector (Hegg & Hobbs, 1986) that was manually  
1292 placed out of the aircraft during cloud passes to collect cloud water. The collected samples were  
1293 analyzed for water-soluble ions using ion chromatography (IC; Thermo Scientific Dionex ICS-  
1294 2100 system) and water-soluble elements using triple quadrupole inductively coupled plasma mass  
1295 spectrometry (ICP-QQQ; Agilent 8800 Series). Liquid-phase concentrations of species were  
1296 converted to air-equivalent units ( $\mu\text{g m}^{-3}$ ) via multiplication with the sample-averaged *LWC*. The  
1297 reader is referred to other works for more extensive discussion about cloud water collection and  
1298 sample analysis from FASE and other recent CIRPAS Twin Otter campaigns (Crosbie et al., 2018;  
1299 Prabhakar et al., 2014; Sorooshian et al., 2013a; Wang et al., 2016; Youn et al., 2015).

1300 Ten Hz measurements of environmental parameters were used to estimate turbulent  
1301 variance and covariance flux values, which may be relevant to the understanding of clearing  
1302 formation and evolution based on past work (Crosbie et al., 2016). To perform the aforementioned  
1303 calculations, collected data for wind speed and temperature were de-trended using a 2-km wide  
1304 high pass filter that utilizes a minimum order-filter with a stopband attenuation of 60 dB and  
1305 transition band steepness of 0.95. Friction velocity ( $u^*$ ) was calculated from the surface leg  
1306 following the method provided in Stull (1988) and Wood (2005, 2005b). In addition, convective  
1307 velocity ( $w^*$ ) was estimated by implementing the buoyancy integral method (Nicholls and  
1308 Leighton, 1986). Turbulent kinetic energy (*TKE*) in the ~~marine boundary layer (MBL)~~ MBL is  
1309 generated by two main mechanisms, specifically shear and buoyancy generation. Following Wood  
1310 (2005, 2005b), the ratio of the MBL depth ( $z_i$ ) to the Monin–Obukhov length ( $L_{MO}$ ) was estimated  
1311 as a way to determine the relative influence of shear versus buoyancy in values of *TKE*. Large  
1312 positive values of the ratio ( $z_i/L_{MO}$ ) are associated with the turbulence in the MBL governed more  
1313 with buoyancy production, while small or negative values are associated with the dominance of  
1314 shear production.

1315 Properties relevant to the inversion layer were estimated from sawtooth maneuvers above  
1316 and below the cloud top, which typically coincided with the inversion base altitude (Fig. 2c). The  
1317 inversion base height was defined as the altitude where the ambient temperature first reached its  
1318 minimum above the sea surface (Crosbie et al., 2016). Inversion top was defined as the highest  
1319 altitude with the gradient inat which  $d\theta/dz$  exceeded  $0.1 \text{ K m}^{-1}$ , where  $\theta_i$  is liquid water potential  
1320 temperature over and  $z$  is altitude in the inversion layer ( $d\theta_i/dz$ ) exceeding  $0.1 \text{ K m}^{-1}$ .  $d\theta/dz$  was  
1321 calculated from linear fits over a moving window of 75 points from 10 Hz data. The following  
1322 characteristics were estimated and reported for the inversion layer: (i) inversion base height; (ii)  
1323 inversion top height; (iii) inversion depth; (iv) jump in liquid water temperature ( $\Delta\theta_i$ ); (v)

Formatted: Font: Italic

Formatted: Font: Italic

Formatted: Font: Italic

Formatted: Font: Italic

Formatted: Font: Italic

Formatted: Font: Italic

Formatted: Font: Italic

Formatted: Font: Italic

Formatted: Font: Italic

Formatted: Font: Italic

Formatted: Font: Italic

Formatted: Font: Italic

Formatted: Font: Italic

Formatted: Font: Italic

Formatted: Font: Italic



1324 maximum gradient of the potential temperature ( $(d\theta/dz)_{\max}$ ); (vi) drop in the total moisture ( $\Delta q_i$ );  
1325 and (vii) change in the horizontal wind speed ( $\Delta U$ ).

Formatted: Font: Italic

Formatted: Font: Italic

Formatted: Font: Italic

## 1327 2.4 Clearing Growth Modeling Using Machine Learning

1328 A Gradient Boosted Regression Tree (GBRT) model approach was implemented to  
1329 investigate the impact of environmental parameters on the evolution of clearing events- (Friedman  
1330 2001). GBRT models have been successfully used in past work to study low-level clouds (Fuchs  
1331 et al., 2018). The Scikit-Learn library (Pedregosa et al., 2011) was used for careful parameter  
1332 tuning in order to accurately represent the data and desired relationships without overfitting the  
1333 model (Fuchs et al., 2018).

Formatted: Font: Italic

1334 We apply the GBRT model to analyze clearing growth rates of total area ( $GR_{Area}$ ) obtained  
1335 from the comparative analysis between GOES Image 1 (~9:00 PST) and Image 2 (~12:00 PST)  
1336 ~~or~~ for each of the 306 events. As will be shown, the most rapid clearing growth occurs between  
1337 9:00 and 12:00 PST among the three time increments between Images 1-4 (i.e., 09:00 - 18:00 PST).  
1338 Here we describe how the predictor values were obtained. A rectangular box was placed around  
1339 the larger of the clearing areas from Image 1 or 2 for each clearing event using the maximum and  
1340 minimum values of both latitude and longitude. The same size rectangular box was then placed on  
1341 the other image using identical latitude and longitude bounds. MERRA-2 data were then obtained  
1342 for each  $0.5^\circ \times 0.625^\circ$  grid within the rectangular area for the two images, and then averaged for  
1343 the pair of images. Each grid was also assigned the value of the clearing  $GR_{Area}$  for the entire  
1344 clearing (i.e., each grid had the same value of  $GR_{Area}$  assigned to it). Parameters used in the  
1345 modeling included those relevant to aerosol (aerosol optical depth ( $AOD$ )), thermodynamics (air  
1346 temperature ( $T$ ), air specific humidity ( $q$ ), and sea-surface temperature ( $SST$ ), and dynamic  
1347 variables (mean sea level pressure anomaly ( $MSLP_{anom}$ ), zonal wind speed ( $U$ ), meridional wind  
1348 speed ( $V$ ), planetary boundary layer height ( $PBLH$ ), and vertical pressure velocity ( $\omega$ )). Most of  
1349 the aforementioned variables were first analyzed at different vertical levels including the surface,  
1350 950 hPa, 850 hPa, and 700 hPa in order to then filter variables out to keep only the most appropriate  
1351 input parameters.

Formatted: Font: Italic

Formatted: Font: Italic

Formatted: Font: Italic

Formatted: Font: Italic

Formatted: Font: Italic

Formatted: Font: Italic

Formatted: Font: Italic

Formatted: Font: Italic

Formatted: Font: Italic

Formatted: Font: Italic

Formatted: Font: Italic

Formatted: Font: Italic

Formatted: Font: Italic

Formatted: Font: Italic

Formatted: Font: Italic

Formatted: Superscript

Formatted: Superscript

1352 Model simulation results are reported in terms of a parameter termed 'partial dependence'  
1353 ( $PD$ ) following methods in earlier works (e.g., Friedman, 2001; Fuchs et al., 2018).  $PD$  plots  
1354 represent the change of the clearing  $GR_{Area}$  relative to a selected parameter by marginalizing over  
1355 the remaining predictors. For each given value of a selected parameter ( $x_s$ ), partial dependence  
1356 ( $PD(x_s)$ ) can be obtained by computing the average of model outputs using the training data as  
1357 shown in Equation 3:

$$1358 \quad PD(x_s) = \frac{1}{n} \sum_{i=1}^n \hat{f}(x_s, x_R^{(i)}) \quad (3)$$

1359 where  $\hat{f}$  is the machine learning model,  $x_R$  are the remaining parameters, and  $n$  is the number of  
1360 instances in the training data.  $PD$  profiles were computed between the 1<sup>st</sup> and 99<sup>th</sup> percentile of  
1361 each selected parameter.

1362 ~~To correctly interpret the model output using the PD criterion and gradient boosting, it was  
1363 required that the model input parameters not be correlated. Thus, the input parameters were chosen  
1364 so as to have the least correlation among them. Two input parameters were determined to be  
1365 independent if a linear regression between the two parameters yielded an  $r^2$  value of less than  
1366 0.5. While PD plots are not flawless in capturing the influence of each variable in the model,  
1367 especially if the input variables are strongly correlated, they provide useful information for  
1368 interpretation of GBRT results (Friedman and Meulman 2003; Elith et al., 2008). To decrease the~~



1369 ~~undesired influence of correlated variables on PD profiles, an arbitrary  $r^2$  threshold of 0.5 was~~  
1370 ~~used based on the linear regressions between prospective input parameters.~~ For instance, there  
1371 were three choices of air temperature (i.e., at 950, 850, and 700 hPa), but based on the  $r^2$  criterion,  
1372 only one ( $T_{850}$ ) was used in the model, ~~as it proved to be an independent~~ ~~minimize the unwanted~~  
1373 ~~impact of dependent~~ input ~~parameter~~ ~~parameters~~. Lower tropospheric stability (*LTS*: defined as the  
1374 difference between the potential temperature of the ~~free troposphere~~ ~~FT~~ (700 hPa) and the surface)  
1375 is the stability parameter that has been widely used as a key factor controlling the coverage of  
1376 stratocumulus clouds. However, in this study, the effects of stability were examined by putting  
1377  $T_{850}$  and  $SST$  into the model without explicitly including *LTS*. The correlation between *LTS* and  
1378  $T_{850}$  prevented them to be used as input parameters simultaneously. Using  $T_{850}$  and  $SST$  instead of  
1379 *LTS* is advantageous because the results can be more informative by revealing different impacts of  
1380 the two individual parameters on the model's output rather than just one parameter in the form of  
1381 *LTS*. In addition, the mean sea level pressure anomaly ( $MSLP_{anom}$ ) was used as an input parameter,  
1382 which was calculated in reference to the average values of  $MSLP$  for the summer months for the  
1383 study period. In the end, the following ~~eleven~~ ~~11~~ predicting variables from MERRA-2 were used as  
1384 input parameters for the GBRT simulations, with data product details summarized in Table 1:  
1385  $AOD$ ,  $T_{850}$ ,  $q_{950}$ ,  $q_{850}$ ,  $q_{700}$ ,  $SST$ ,  $MSLP_{anom}$ ,  $U_{850}$ ,  $V_{850}$ ,  $PBLH$ , and  $\omega_{700}$ . ~~It is important to note that~~  
1386 ~~the results of extensive sensitivity tests led to the selection of the set of parameters presented in~~  
1387 ~~this study. Also, these sensitivity tests confirmed that the general conclusions presented here were~~  
1388 ~~preserved regardless of using different sets of the input parameters.~~

1389 To train, test, and validate the statistical models, the dataset was split into random parts.  
1390 The training set was comprised of 75% of the data points, 30% of which were randomly selected  
1391 for validation. This process helped reduce variance and increase model robustness. The remaining  
1392 25% of the data points comprised the test dataset. The model setup was tuned using training data,  
1393 for which different scenarios were tested that were specified by a parameter grid through a 10-fold  
1394 cross-validated search. The model was run on the dataset 30 times to achieve robust results. To  
1395 qualitatively rank the input parameters based on their influence on growth rates, ~~differences~~  
1396 ~~between the maximum and minimum of PD ( $\Delta PD$ ) were calculated over 30 runs~~ ~~two scoring~~  
1397 ~~metrics were calculated over 30 runs: (i) differences between the maximum and minimum of PD~~  
1398 ~~( $\Delta PD$ ); and (ii) the relative feature importance following the method developed by Friedman~~  
1399 ~~(2001), which is determined by the frequency that a variable is chosen for splitting, weighted by~~  
1400 ~~the gained improvement due to each split and averaged over all trees (Friedman and Meulman~~  
1401 ~~2003; Elith et al., 2008).~~

### 1403 3. Results and Discussion

#### 1404 3.1 Temporal and Spatial Profile of Clearings

##### 1405 3.1.1 Monthly and Interannual Trends

1406 The frequency of clearing events was quantified for the three summer months (June – July  
1407 – August, JJA) of each year ~~between~~ ~~from~~ 2009 ~~and~~ ~~through~~ 2018 (Fig. 33a). Note that if a clearing  
1408 event lasted multiple days as in the case of the 11-day clearing probed by Crosbie et al. (2016), it  
1409 was counted separately for each individual day rather than assigned a value of one for a multi-day  
1410 period. There was considerable interannual variability, with clearing events ranging between a  
1411 minimum of 14 in 2017 and a maximum of 45 in 2011. The relative percentage of total days in the  
1412 summer season having clearings ranged from 15.2% – 48.9% with a mean  $\pm$  standard deviation of  
1413  $33.3 \pm 10.9$  days. The specific month with the most clearing events varied between years, with  
1414 August typically having the least number of events among the summer months. The most recent

Formatted: Font: Italic

Formatted: Font: Italic

Formatted: Font: Italic

Formatted: Font: Italic

Formatted: Font: Italic

Formatted: Font: Italic

Formatted: Font: Italic

Formatted: Font: Italic

Formatted: Font: Italic

Formatted: Font: Italic

Formatted: Font: Italic

Formatted: Font: Italic

Formatted: Font: Italic

Formatted: Font: Italic

Formatted: Font: Italic

Formatted: Font: Italic

Formatted: Font: Italic

Formatted: Font: Italic

Formatted: Font: Italic

Formatted: Font: Italic

Formatted: Font: Italic

Formatted: Font: Italic

Formatted: Font: Italic

Formatted: Font: Italic

Formatted: Font: Italic

1415 year of the decade examined, 2018, was used to more closely examine the distribution of clearing  
1416 events as a function of all 12 months. Daily probabilities of clearing events are shown for each  
1417 month, with the highest probability between May and September ( $> 0.2$ ), especially June ( $\sim 0.42$ )  
1418 (Fig. 3b). Daily probabilities were lowest in the winter season, with January having no clearings  
1419 (0).

1420 To identify if the monthly profile of clearings is biased by the monthly profile of  $CF$ , Figs.  
1421 S3-S4 show the mean annual cycle of MODIS  $CF$  for 2018 and 2009-2018, respectively. The range  
1422 in  $CF$ s for 2018 and 2009-2018 were 0.59-0.76 and 0.60-0.74, respectively, with the mean values  
1423 being  $0.69 \pm 0.05$  and  $0.68 \pm 0.04$ . This is indicative of relatively low variability. A reasonable  
1424 question is if August had the lowest clearing daily probability of the summer months because it  
1425 potentially had the lowest  $CF$ . Figs. S3-S4 do not show significant variations in  $CF$  between the  
1426 summer months, with mean values in 2018 for June, July, and August being 0.71, 0.72, and 0.72,  
1427 respectively. Also, the lowest mean daily probability in 2018 was for January and February, but  
1428 those months do not exhibit the lowest  $CF$  (January = 0.76, February = 0.67). Rather, September  
1429 exhibited the lowest  $CF$  (0.59). Finally,  $CF$  decreased from 0.72 to 0.59 from August to September  
1430 2018, but the daily probability of clearings actually increased slightly. Thus, the systematic  
1431 changes in  $CF$  between months are not the primary cause for inter-monthly variation in clearing  
1432 formation.

### 1433 3.1.2 Diurnal

1434 Dimensional characteristics of cloud clearings as a function of time of day are summarized  
1435 here. The median width of clearings was smallest in the morning at 09:00 (193 km), with an  
1436 increase between 09:00 and 12:00, and then a leveling off in expansion until 18:00 (443 km) (Fig.  
1437 4). Clearing length and area followed the same qualitative trend in growth with an initial increase  
1438 and then leveling off. The median length and area of clearings at 09:00 were 680 km and  $\sim 67,000$   
1439  $\text{km}^2$ , respectively, with values at 18:00 being  $\sim 1231$  km and  $\sim 250,000$   $\text{km}^2$ . The aspect ratio  
1440 (width:length) was of interest to quantify how long such clearings are relative to their width  
1441 throughout the day, with results indicating a minor increase that was more linear than asymptotic  
1442 (from  $\sim 0.32$  at 09:00 to  $\sim 0.37$  at 18:00). Although the range in median values was very small, there  
1443 was significant variability at each of the four time steps shown. Figure 5S5 quantifies the  $GR$  of  
1444 total area, width, and length by comparing 12:00 to 09:00, 15:00 to 12:00, and 18:00 to 15:00. The  
1445  $GR$ s for clearing length, width, and area are expectedly lowest from 15:00 to 18:00 and highest  
1446 from 09:00 to 12:00.

1447 Figure 65 shows cloud fraction  $CF$  maps for the times corresponding to panels 1 – 4 for all  
1448 306 events between 2009 and 2018. The spatial maps show that the centroid of the clearings is  
1449 generally focused on the coastal topographical features along the central to the northern coast of  
1450 California including especially just south of Cape Mendocino and Cape Blanco. Less pronounced  
1451 is a centroid of reduced  $CF$  by Point Conception, where similar mechanisms may be at work. The  
1452 09:00 map most clearly shows that those two topographical features potentially serve as ‘trigger  
1453 points’ for the majority of clearings, and as a typical clearing day develops, the cloud fraction  $CF$   
1454 gets reduced around those points by moving farther south and to the west. Juliano et al. (2019a,b)  
1455 also discussed the significance of these capes is discussed in their analysis of CTDs many  
1456 previous studies (Beardsley et al., 1987; Haack et al., 2001; Juliano et al., 2019a,b) pointing to  
1457 their ability to alter local dynamics, cloud depth, and various microphysical processes such as  
1458 entrainment. Southerly wind during CTDs promotes cloud thinning on the northern

Formatted: Font: Italic

Formatted: Font: Italic

Formatted: Font: Italic

Formatted: Font: Italic

Formatted: Font: Italic

Formatted: Font: Italic

Formatted: Font: Italic

Formatted: Font: Italic

Formatted: Font: Italic

Formatted: Font: Italic

Formatted: Font: Italic

1460 ~~side~~vicinity of the capes due to an expansion fan effect (~~is reported for both northerly and southerly~~  
1461 ~~flow~~ (Beardsley et al., 1987; Juliano et al., 2017).

1462

### 1463 3.2 Contrasting Clearing and Non-Clearing Cases

1464 Large-scale ~~characteristics of a~~ dynamic and thermodynamic ~~nature characteristics were~~  
1465 ~~contrasted~~ (parameters in Table 1) ~~were contrasted~~ between clearing and non-clearing days (Fig.  
1466 7). Sub-daily data were averaged up to daily resolution for parameters of interest, which were  
1467 subsequently used to produce a climatology for non-clearing (614 days) and clearing (306 days)  
1468 cases for the summers between 2009 and 2018. ~~It is important to note that non-clearing cases~~  
1469 ~~include those summer days (e.g., June, July, and August) from 2009 through 2018 that were not~~  
1470 ~~categorized as clearing days.~~ We further calculated the difference between clearing and non-  
1471 clearing conditions.

1472 The Pacific high usually sets up ~~a few hundred kms~1000 km~~ west of California during the  
1473 summertime, which promotes northerly flow near the surface along the coastline (e.g., Juliano et  
1474 al., 2019a). As compared to non-clearing cases, clearing days are characterized by having an  
1475 enhanced Pacific high shifted more towards northern California (Fig. 7-6a). ~~The presence of~~  
1476 ~~Pacific high over the ocean and thermal low over the land, especially for the summer months, are~~  
1477 ~~the main synoptic components contributing to the formation of coastal low-level jets (CLLJs)~~  
1478 ~~along the California coast (Beardsley et al., 1987; Parish 2000). California CLLJs are characterized~~  
1479 ~~by vertically narrow regions of intensified coast-parallel winds in low altitudes near the MBL top~~  
1480 ~~(Burk and Thompson 1996) with an average strength of  $\sim 15 \text{ m s}^{-1}$  (Lima et al., 2018). In contrast,~~  
1481 ~~CLLJs have a relatively large horizontal offshore extent of up to a couple of hundred kms, which~~  
1482 ~~is determined by the Rossby radius of deformation (Ranjha et al., 2013).~~ In both cases (clearing  
1483 and non-clearing), the cross-coast gradient in ~~MSLP~~ and 850 hPa geopotential height gradients are  
1484 the highest in northern California and directed away from the coast. Due to the displacement of  
1485 the Pacific high towards the northeast part of the study region on clearing days, these gradients are  
1486 much more profound on clearing days as compared to non-clearing days. ~~The zonal pressure~~  
1487 ~~gradient is the main parameter controlling the intensity and occurrence of California CLLJs~~  
1488 ~~(Zemba and Friehe 1987; Parish 2000; Lima et al., 2018). The probability of CLLJ incidents is~~  
1489 ~~most likely greater on clearing days as a response to the enhanced pressure gradients near the coast.~~  
1490 ~~This results in~~ ~~is also supported by low level wind fields shown in Fig. 7, which exhibit~~ a 2-5 m s<sup>-1</sup>  
1491 increase in northerly surface wind speed (Fig. 8a7a) between 35°N and 45°N. Looking at the 850  
1492 hPa wind field (Fig. 8b7b), there is also a  $\sim 2\text{-}5 \text{ m s}^{-1}$  increase in wind speed but in this case more  
1493 in a northeasterly direction, which equates to having offshore flow from the northern California  
1494 coast. The tightening of the 850 hPa geopotential height gradient on clearing days results in strong  
1495 offshore flows by Cape Blanco and Cape Mendocino (Fig. 8a) ~~where cloud fraction minima are~~  
1496 ~~observed (Fig. 6-7b) where CF minima are observed (Fig. 5). In addition, Beardsley et al. (1987)~~  
1497 ~~reported periods of low cloudiness along the California coast as a response to the synoptic scale~~  
1498 ~~features, an increase in the pressure gradient along the coast, and enhanced wind speeds. In other~~  
1499 ~~studies, over the southeast Pacific (Garreaud and Munoz 2005; Zuidema et al., 2009), dissipation~~  
1500 ~~of the coastal stratocumulus cloud deck was observed over the jet regions.~~ Average conditions at  
1501 500 hPa indicate mostly westerly flow on both clearing and non-clearing days. Non-clearing days  
1502 exhibited a weak trough offshore, while during clearing days a ridge is present at 500 hPa farther  
1503 offshore, ~~which can be attributed to.~~ ~~Displacement and strengthening of the stronger~~ high-pressure  
1504 system on clearing days: ~~can be associated with the passage of mid-latitude ridges (Garreaud and~~  
1505 ~~Munoz 2005).~~

Formatted: Font: Italic

1506 The difference in air temperature between clearing and non-clearing cases at the surface  
1507 reaches up to  $\sim 0.7$  K on the western edge of the study domain (Fig. 7a6a). Clearing cases exhibited  
1508 cooler temperatures closer to the coast where the clearings develop and evolve. *SST* shows a similar  
1509 pattern as air temperature at the surface (Fig. 9a8a). Faster offshore winds at the surface can  
1510 promote ocean upwelling and thus cooler *SSTs* (Lima et al., 2018), as was also observed for CTD  
1511 events in the same region (Juliano et al., 2019a). Furthermore, the generally high ~~cloud~~  
1512 ~~fractions~~*CFs* during clearing days for the entire spatial domain reduces radiative transfer to the  
1513 ocean, also acting to reduce *SST* over the broader study region. ~~It is well documented that~~  
1514 ~~cloudiness~~*Cloudiness* and surface winds play a major role in influencing *SSTs* (e.g., Klein et al.,  
1515 1995). In contrast, air temperatures at higher levels (850 and 500 hPa) are enhanced adjacent to  
1516 the coastline in clearing cases. Air temperature at 850 hPa is higher (lower) to the south (north) of  
1517 Cape Blanco and Cape Mendocino (Fig. 65) in clearing cases as compared to non-clearing cases,  
1518 with the difference reaching as high as  $\sim 2$  K. The enhanced offshore flow of warm and dry air in  
1519 in the vicinity of Cape Blanco and Cape Mendocino likely ~~contribute~~*contributes* to why many of  
1520 the clearings geographically are centered ~~at~~*by* these coastal topographical features (Fig. 6-5). ~~It is~~  
1521 ~~noteworthy that over the west coast of subtropical South America, cloud dissipation over and~~  
1522 ~~upstream of the coastal jet region was reported (Garreaud and Munoz 2005; Zuidema et al., 2009),~~  
1523 ~~whereas downstream there was enhanced CF, which appears to be analogous to this study.~~

1524 ~~Concomitant with higher cloud fraction and reduced SSTs, The changes in synoptic-scale~~  
1525 ~~conditions, including relocation/strengthening of the study region also exhibited generally higher~~  
1526 ~~LTS by up to  $\sim 2$  K Pacific high, on clearing days versus in comparison to non-clearing days (Fig.~~  
1527 ~~9b). Other works have pointed to the connection between cooler SSTs, higher boundary layer cloud~~  
1528 ~~amount, and increased stability in the lower atmosphere (Norris and Leovy 1994, Klein and~~  
1529 ~~Hartman 1993). With enhanced LTS values on clearing days, it is expected that there will be~~  
1530 ~~simultaneously strong can alter large-scale subsidence. This is indeed confirmed in Fig. 9e8b using~~  
1531  ~~$\rho_{700}$  as the proxy variable, with the strongest difference between clearing and non-clearing days~~  
1532 ~~(up to  $\sim 0.1$  Pa  $s^{-1}$ ) off the coast by Cape Blanco and Cape Mendocino and~~  
1533 ~~geographical~~*geographically* coincident with where the sharpest gradients occur for *MSLP* between  
1534 clearing and non-clearing cases (Fig. 7-6a). It is interesting to note that the maximum *LTS* values  
1535 ~~in LTS~~ coincide spatially with ~~enhanced values of  $\rho_{700}$  on non-clearing days, in contrast to clearing~~  
1536 ~~days when the peak value of  $\rho_{700}$  is farther north from where LTS peaks (Fig. 8c). Consistent with~~  
1537 ~~the results presented here (Fig. 8b), modeling studies (Burk and Thompson 1996; Munoz and~~  
1538 ~~Garreaud 2005) reported enhanced subsidence for the entrance regions of the Chilean and~~  
1539 ~~California CLLJs in response to coastal features. These studies also reported the generation of a~~  
1540 ~~warm layer above the MBL due to coastal mechanisms especially downstream of coastal points~~  
1541 ~~and capes. This is also the case in this study where higher air temperature at 850 hPa was observed~~  
1542 ~~to the south of Cape Blanco and Cape Mendocino on clearing days (Fig. 6b). In addition, higher~~  
1543 ~~LTS values on clearing days by up to  $\sim 2$  K (Fig. 8c) are largely associated with the presence of~~  
1544 ~~warmer layer above the MBL south of Cape Blanco and Cape Mendocino. It is likely that reduced~~  
1545 ~~SSTs and greater subsidence contributed to generally higher LTS on clearing days versus non-~~  
1546 ~~clearing days (Fig. 8c). Other works have pointed to the connection between cooler SSTs, higher~~  
1547 ~~boundary layer cloud amount, and increased stability in the lower atmosphere (Klein and Hartman~~  
1548 ~~1993; Norris and Leovy 1994).~~

1549 Another key environmental parameter related to MBL cloud coverage is the *PBLH*.  
1550 ~~Regardless~~*Consistent with previous studies (Neiburger et al., 1961; Wood and Bretherton 2004),*  
1551 ~~regardless~~ of whether clearings were present, *PBLH* generally increases with distance from the

Formatted: Font: Italic

Formatted: Font: Italic

Formatted: Font: Italic

Formatted: Font: Italic

Formatted: Font: Italic

Formatted: Font: Italic

Formatted: Font: Italic

Formatted: Font: Italic

Formatted: Font: Italic

Formatted: Font: Italic

Formatted: Font: Italic

1552 coast (Fig. 9d), where warmer SSTs lead to deeper MBLs by weakening the inversion  
1553 (Bretherton and Wyant 1997). The shallowing of the MBL near the California coast is also notable  
1554 with enhanced gradients on clearing days. The aforementioned MBL shallowing is believed to be  
1555 a crucial element in development of the coastal jet off the California coast (Zemba and Friehe  
1556 1987; Parish 2000). Previous studies (Beardsley et al., 1987; Edwards et al., 2001; Parish 2000;  
1557 Zuidema et al., 2009) also reported MBL height adjustment in the vicinity of coast due to hydraulic  
1558 adaptation to coastal topography, thermally driven circulation, and geostrophic adjustment in the  
1559 cross-coast direction in response to the contrast in surface heating between ocean and land. There  
1560 is also a strong gradient in PBLH along the shoreline in the vicinity of Cape Blanco (Fig. 8d).  
1561 While the presence of a similar gradient in SST (Fig. 8a) may partly explain the observed  
1562 gradient in PBLH, coastally induced processes could also play a role.

Formatted: Font: Italic

1563 Comparing clearing with non-clearing days, PBLH tends to be higher on clearing days  
1564 though, with the largest differences (~200 m) observed to the north off the coasts of Washington  
1565 and British Columbia. The smallest, which re-emphasizes the important role of coastal topography  
1566 near Cape Blanco and Cape Mendocino in mesoscale dynamics (Beardsley et al., 1987; Haack et  
1567 al., 2001). Zuidema et al. (2009) suggested that dynamical blocking of the surface winds by the  
1568 southern Peruvian Andes contributed to boundary layer thickening by encouraging mesoscale  
1569 convergence. Enhanced dynamical blocking of surface winds by coastal topography near Cape  
1570 Blanco, as suggested by greater wind speeds on clearing days (Fig. 7a), can lead to a deeper MBL  
1571 in the coastal regions north and northwest of Cape Blanco. In contrast, coastal areas south of Cape  
1572 Blanco, exhibit negligible differences existed where the majority of clearings evolved, specifically  
1573 off the California coast in PBLH between clearing and non-clearing days. In the aforementioned  
1574 regions, enhanced hydraulic response (i.e., expansion fan (Parish et al., 2016)) to coastal  
1575 topography, may cause slightly shallower MBL on clearing days.

Formatted: Font: Italic

1576 Higher MBL depths in the offshore regions of clearing days is noteworthy to discuss.  
1577 Parameters influencing MBL depth include entrainment rates, vertical velocity at the top of MBL,  
1578 and horizontal advection of MBL (Wood and Bretherton 2004; Rahn and Garreaud 2010).  
1579 Although on clearing days there may be greater subsidence rates offshore (Fig. 8b) promoting a  
1580 shallower MBL, the sum of entrainment and horizontal advection terms counteract the  
1581 aforementioned effect resulting in a deeper MBL. Wood and Bretherton (2004) showed for the  
1582 Northeast and Southeast Pacific that entrainment and subsidence were the most influential terms  
1583 in the MBL prognostic equation, which acted in the opposite manner. It is also likely that  
1584 entrainment processes resulting from changes in small scale turbulence contributed to elevated  
1585 PBLH on clearing days (Randall 1984; Rahn and Garreaud 2010). The maps of cloud fraction CF  
1586 from MODIS Terra (Fig. 10a) can provide at least one possible explanation for the spatial  
1587 differences in PBLH between clearing and non-clearing days. Cloud fraction is generally higher  
1588 for the broad study region on clearing days, which leads to more opportunity for cloud top radiative  
1589 cooling to then fuel turbulence in MBL (Wood 2012). Greater turbulence can lead to a deeper  
1590 MBL. But in the one area where PBLHs are not enhanced for the clearing days, off the California  
1591 coast, cloud fractions are reduced, which is why PBLH does not exhibit by promoting greater  
1592 values and actually has lower PBLH values. entrainment at the top of MBL (Randall 1984; Wood  
1593 2007).

Formatted: Indent: First line: 0.5"

1594 Figure 9e shows spatial maps of specific humidity at 10 m above the sea surface ( $q_{10m}$ ),  
1595 which serves as a proxy of available moisture in MBL. Assuming a shallow and well-mixed MBL,  
1596  $q_{10m}$  represents moisture levels in the MBL. Similar to SST,  $q_{10m}$  increases to the south of the

Formatted: Font: Italic

Formatted: Font: Italic

Formatted: Font: Italic

Formatted: Font: Italic



1597 study region with especially reduced values immediately adjacent to the California coast.  
1598 Comparing clearing and non-clearing days, the former is less humid in the MBL (up to  $-0.6 \text{ g kg}^{-1}$ ).  
1599 This is at least partly attributed to offshore flow and entrainment of dry continental air. Specific  
1600 humidity was also examined at 850 hPa, which is closer to the vertical layer more relevant to air  
1601 impacting cloud top close to the coastline. Figure 9f8f shows that  $q_{850}$  was substantially lower (up  
1602 to  $\sim -1.2 \text{ g kg}^{-1}$ ) in the clearing cases, especially in the regions where most of the clearings occur.  
1603 Drier air above cloud top will decrease cloudiness through entrainment processes. It is interesting  
1604 to note that the area of greatest  $q_{850}$  difference (Fig. 9f8f) corresponds to the area of greatest  
1605 northeasterly winds in the difference plot of the wind field at 850 hPa (Fig. 8b7b). These pieces of  
1606 evidence point to the role of dry continental air in contributing to the formation and sustenance of  
1607 clearings via offshore flow.

Formatted: Font: Italic

Formatted: Font: Italic

1608 Another important parameter influencing MBL clouds is nuclei of the cloud droplets,  
1609 specifically the cloud condensation nuclei (*CCN*). *CCN* in the region originate from a blend of  
1610 sources, including natural ones (sea spray, marine and continental biogenic emissions, terrestrial  
1611 dust), biomass burning, ship exhaust, and continental anthropogenic sources (Hegg et al., 2010;  
1612 Coggon et al., 2014; Wang et al., 2014; Maudlin et al., 2015; Mardi et al., 2018). As a  
1613 representation of the general level of aerosol pollution in the region, spatial maps are shown for  
1614 Aerosol Optical Depth (*AOD*), which is a columnar measurement of aerosol extinction (Fig. 9g8g).  
1615 In general, regions closer to the shore exhibit higher values of *AOD* on non-clearing days, with  
1616 especially higher levels north of  $40^\circ \text{ N}$ . It is unclear as to why this is, since stronger winds on  
1617 clearing days along the coast have the potential for more emissions from marine biogenic sources  
1618 (via upwelling), sea spray, and offshore continental flow. Although based on speculation, one of  
1619 many possible explanations could be that stronger fluxes of sea spray on clearing days have the  
1620 potential to expedite the drizzle formation process in polluted clouds via broadening of cloud  
1621 droplet size distributions, which leads to wet scavenging of aerosols in the study region  
1622 (Dadashazar et al., 2017; Jung et al., 2015; MacDonald et al., 2018; Sorooshian et al., 2013b).  
1623 South of Cape Blanco and Cape Mendocino on clearing days, there were pockets of high *AOD*  
1624 relative to other coastal locations, which is presumed to be linked to stronger winds and offshore  
1625 continental flow; this is analogous to how CTD events exhibit more pollution north of these coastal  
1626 features when there is southerly flow (Juliano et al., 2019a). That the greatest *AOD* differences  
1627 occur close to the coast ~~warrant~~warrants additional research as ~~they~~such differences may be  
1628 suggestive of variations in ocean-land-atmosphere interactions that result from the movement and  
1629 strengthening of the Pacific high during clearing events. Future work should examine if such *AOD*  
1630 differences on clearing versus non-clearing days are linked to differences in MBL sources and  
1631 sinks (i.e., wet scavenging), or FT processes.

Formatted: Font: Italic

Formatted: Font: Italic

Formatted: Font: Italic

Formatted: Font: Italic

Formatted: Font: Italic

Formatted: Font: Italic

Formatted: Font: Italic

1632 Spatial maps of cloud microphysical variables provide consensus that clearing days  
1633 generally have higher  $N_d$  and reduced values of  $r_e$ ,  $\tau$ , and *LWP* near the California coast where  
1634 clearings form and evolve (Fig. 409). Figure 55S6 shows the same qualitative results based on  
1635 MODIS Aqua data for cloud microphysical parameters. Lower *LWP* values on clearing days near  
1636 the coast are consistent with offshore flow of dry and warm air eroding clouds. The combination  
1637 of higher  $N_d$  and lower *LWP* by the coastline results in smaller  $r_e$  on clearing days. The more  
1638 polluted clouds along the coastline during clearing days, especially south of major capes, is  
1639 analogous to CTD clouds being more polluted during southerly wind regimes in the study region  
1640 (Juliano et al., 2019a<sup>4</sup>,b). An intriguing aspect of clearing days was that although a significant  
1641 section of the study region was cloud-free, the mean cloud albedo (*A*) over the entire study domain  
1642 was actually slightly higher than on non-clearing days (Fig. 40f9f). More specifically, the domain-

Formatted: Font: Italic

Formatted: Font: Italic

Formatted: Font: Italic

Formatted: Font: Italic

Formatted: Font: Italic

Formatted: Font: Italic

Formatted: Font: Italic

Formatted: Font: Italic

Formatted: Font: Italic

1643 averaged  $A$  values based on MODIS Terra data (and using Eq. 2) were 0.50 and 0.53 for non-  
1644 clearing and clearing cases, respectively. The corresponding values using MODIS Aqua data were  
1645 0.48 and 0.50, respectively. It is possible that the method used to identify clearing led to the greater  
1646  $CF$  and  $A$  on clearing days in distant offshore regions. It is difficult to identify the root cause of  
1647 greater  $CF$  and  $A$  on clearing days versus non-clearing days, but Garreaud and Munoz (2005) also  
1648 demonstrated that the cloud deck tends to dissipate over CLLJ regions in contrast to an increase in  
1649 cloudiness downstream of the jet core. This is also the case in this study as large scale conditions  
1650 such as an intensified Pacific high and greater  $LTS$  on clearing days are in favor of the preservation  
1651 of cloud deck in the regions except for coastal areas impacted by a CLLJ.

Formatted: Font: Italic

Formatted: Font: (Default) Times New Roman, 12 pt

### 1653 3.3 Modeling of Clearing Growth Rates

1654 It has been already shown (Figs. 4-65) that clearings exhibit diurnal variability in  
1655 dimensional characteristics, with rapid growth between 09:00 and 12:00 PST- (Fig. S5). It is of  
1656 interest now to examine what environmental parameters control the growth within this 3 h period  
1657 based on the 306 clearing cases between 2009 and 2018. The GBRT modeling method was used  
1658 to this end based on the method described in Section 2.4.

1659 The coefficient of determination ( $r^2$ ) between predicted and observed clearing growth rates  
1660 for the 30 randomly selected testing datasets ranged between 0.52 to 0.77 with an average of 0.65.  
1661 A multivariate linear regression model using the LASSO method (Tibshirani, 1996) was also  
1662 applied to the obtained dataset to assess the performance of the GBRT model in comparison to the  
1663 linear model. The  $r^2$  value of the linear model varied between 0.08 and 0.11 with an average of  
1664 0.10, revealing the poor performance as compared to the GBRT model. As noted in at least one  
1665 previous study (Klein 1997), linear models can explain less than 20% of the variance in low cloud  
1666 amount on daily time scales. This is in contrast to monthly time scales for which such models  
1667 perform much better and can explain over 50% of the variance (Klein and Hartmann, 1993; Norris  
1668 and Leovy, 1994). Part of the success of the GBRT model to ~~model~~reproduce clearing growth rates  
1669 can be attributed to the complexity of the model, specifically its ability to capture non-linearity  
1670 between clearing growth rates and environmental parameters.

Formatted: Font: Italic

Formatted: Font: Italic

1671 ~~As there is independence between model parameters, the~~The range of  $PD$ s for each  
1672 individual environmental parameter ~~is and the relative feature importance are~~ used here as a  
1673 ~~proxy~~two proxies for the sensitivity of clearing growth rates to that specific parameter. Higher  $PD$   
1674 ranges translate to a higher sensitivity of  $GR_{Area}$  to that specific parameter, indicating that it is a  
1675 major influential factor. The range of partial dependence ( $PD$ ) of clearing growth rates for all the  
1676 parameters included in the GBRT model is provided in Fig. 11, moving from left to right in order  
1677 of highest to lowest  $PD$  ranges. Figure 12 likely a major influential factor. In addition, the relative  
1678 feature importance indicates how useful each parameter was in building the GBRT model. The  
1679 range of  $PD$  of clearing growth rates and relative feature importance for all the parameters included  
1680 in the GBRT model are provided in Fig. 10, moving from left to right in order of highest to lowest  
1681 influence in the model. While it is expected that the results of these two methods of rankings do  
1682 not match perfectly (Fig. 10a and 10b), certain characteristics are similar between these two  
1683 proxies: (i) using both proxies,  $T_{850}$  and  $\omega_{700}$  appeared as the top and lowest ranking parameters,  
1684 respectively; (ii)  $q_{950}$  emerges as one of the most important parameters, being second and third  
1685 place according to the range of  $PD$  and relative feature importance proxies, respectively; (iii)  $AOD$   
1686 and  $q_{700}$  emerged among the four lowest-ranking parameters; and (iv)  $SST$  and  $V_{850}$  appear next to  
1687 each other in the ranking using both scoring proxies. There are some distinct differences among  
1688 the ranking of parameters as shown in Fig. 10. For instance, while  $MSLP_{anom}$  appeared as a

Formatted: Font: Italic

Formatted: Font: Italic

Formatted: Font: Italic

1689 moderately influential parameter in  $GR_{Area}$  according to  $PD$  proxy, this parameter turned out to be  
1690 the second most important variable using the relative feature importance proxy. In another  
1691 example,  $q_{850}$  has the second least important rank according to relative importance feature proxy,  
1692 but it is moderately important based on the  $PD$  range (Fig. 10a). The observed discrepancies  
1693 between the results of two proxies can stem from underlying differences in the methods used to  
1694 quantify the relative significance of each parameter. Moreover, the relative feature importance  
1695 proxy may be less susceptible to the unwanted influence of highly correlated input predictors on  
1696 the ranking outcome (Hastie et al., 2009).

1697 Figure 11 shows the profiles of  $PD$  for  $GR_{Area}$  ( $PD_{GR_{Area}}$ ) relative to each individual  
1698 parameter tested, where increasing values of  $PD_{GR_{Area}}$  indicate that the corresponding change on  
1699 the x-axis for the value of the specific parameter is conducive to faster clearing growth.

1700 Figure 11 displays the  $PD$  of clearing  $GR_{Area}$  for the range of change in environmental parameters  
1701 used in the GBRT model. The top ranking parameter with the highest  $PD$  range was air  
1702 temperature at 850 hPa ( $T_{850}$ ). The difference in  $PD$  range from  $T_{850}$  to the next best parameter  
1703 ( $q_{950}$ ) was the greatest between any other consecutive pair of parameters. Note that the 5<sup>th</sup>, 25<sup>th</sup>,  
1704 50<sup>th</sup>, 75<sup>th</sup>, and 95<sup>th</sup> percentiles of input parameter values are denoted in Figure 11 to caution that  
1705 sharp slopes in the bottom and top 5<sup>th</sup> percentiles are based on few data points and that robust  
1706 conclusions should not stem from those outer bounds. The response of  $PD_{GR_{Area}}$  to the changes in  
1707  $T_{850}$  is shown in Figure 11a.  $T_{850}$  is closely linked to inversion strength variables such as  $LTS$  (Klein  
1708 and Hartmann, 1993) and estimated inversion strength ( $EIS$ ) (Wood and Bretherton, 2006). At  
1709 constant  $SST$ , higher  $T_{850}$  translates to higher  $EIS$  and  $LTS$  values. It is well-established that  
1710 inversion strength plays a key role in controlling MBL cloud coverage (Klein and Hartmann,  
1711 1993). It is expected that higher  $T_{850}$  decreases (increases)  $GR_{Area}$  (cloud amount) by enhancing  
1712 stability. Figure 12a11a shows that up to 290 K, the profile of  $PD$  exhibits a downward trend as  
1713  $T_{850}$  increases. Above 290 K,  $PD$  of  $GR_{Area}$  starts to show the opposite trend with increasing  $T_{850}$ .  
1714 As noted in Brueck et al. 2015, "...increased stability is a necessary but not a controlling factor  
1715 for cloudiness, especially not when it is already sufficiently large. A further increase in inversion  
1716 strength may thus further limit cloudiness, because it increases the entrainment of relatively drier  
1717 and warmer air...". Figure 7b6b showed that  $T_{850}$  was enhanced off the California coast on clearing  
1718 days, pointing to the high potential for warm continental air to impact the underlying cloud deck  
1719 via entrainment. It is important to note that, when the model was run with the same set of  
1720 parameters but replacing  $T_{850}$  with  $LTS$ , the  $PD$  profile of  $LTS$  exhibited a qualitatively similar  
1721 trend to what was presented for  $T_{850}$  in Fig. 12a11a.

1722 The moisture content at 950 hPa was the second most influential parameter. The  $PD_{GR_{Area}}$   
1723 profile of  $q_{950}$  shows increasing values as  $q_{950}$  decreases below  $8 \text{ g kg}^{-1}$ ; (Fig. 11b), coincident with  
1724 dry air that can dissipate clouds and aid in clearing formation and expansion. Further Similarly, the  
1725  $PD_{GR_{Area}}$   $PD$  profile of growth rate generally decreases as  $q_{850}$  showed a sharp decrease below  
1726 values of  $2 \text{ g kg}^{-1}$ ; whereas  $PD_{GR_{Area}}$  leveled off above  $2 \text{ g kg}^{-1}$ ; increases (Fig. 11f). In contrast to  
1727 the other level heights, the  $PD_{GR_{Area}}$  profile of  $q_{700}$  exhibits an opposite trend but a smaller  
1728 influence on  $GR_{Area}$  (Fig. 12j11j). This can be partly due to the fact that this layer of the FT is not  
1729 as close to the cloud layer, which in turn can permit other factors besides the entrainment process  
1730 to stand out. These various humidity parameters clearly show that conditions of dry air close to  
1731 the MBL top help clearings form and expand, with the most likely source being continental air.  
1732 The positive relationship between humidity at the level of clouds and low-level cloud amount was  
1733 reported in earlier studies (Albrecht 1981; Wang et al., 1993; Bretherton et al., 1995; Wang et al.,  
1734 1993).

Formatted: Font: Italic

Formatted: Font: Italic

Formatted: Font: Italic

Formatted: Font: Italic

Formatted: Normal, Indent: First line: 0", Don't adjust space between Latin and Asian text, Don't adjust space between Asian text and numbers, Tab stops: 0.31", Left

Formatted: Font: Italic

Formatted: Font: Italic

Formatted: Font: Italic

Formatted: Font: Italic

Formatted: Font: Italic

Formatted: Font: Italic

Formatted: Font: Italic

Formatted: Font: Italic

Formatted: Font: Italic

Formatted: Font: Italic

Formatted: Font: Italic

Formatted: Font: Italic

Formatted: Font: Italic

Formatted: Font: Italic

Formatted: Font: Italic

Formatted: Font: Italic

Formatted: Font: Italic

Formatted: Font: Italic

Formatted: Font: Italic

Formatted: Not Superscript/ Subscript

Formatted: Font: Italic

Formatted: Font: Italic

Formatted: Font: Italic

Formatted: Font: Italic

Formatted: Subscript

Formatted: Font: Italic

Formatted: Font: Italic

Formatted: Font: Italic



1735 ~~Sea-surface temperature and  $V_{850}$  were the next most influential parameters.~~ As previously  
1736 explained, lower  $SST$  values are associated with cloudiness (Fig. 11c) and increased  $LTS$  (Norris  
1737 and Leovy 1994, Klein and Hartman 1993). Figure 12d displays the dependence of  $PD_{GRArea}$   
1738 on  $V_{850}$ , which is representative of flow in the FT. As discussed already, clearings coincided with  
1739 CLLJs and strong northerly flow at 850 hPa, which is consistent with the sharp increase in  $PD_{GRArea}$   
1740 as northerly wind speeds increased above  $10 \text{ m s}^{-1}$  while otherwise being flat for lower speeds.  
1741 Stronger northerly flow is associated with offshore flow of dry and warm air that can reside above  
1742 the cloud top, which can dissipate the cloud layer after entrainment and via enhanced shearing (via  
1743 Kelvin-Helmholtz instability) and mixing of cloudy parcels with warm and dry air in the FT. (e.g.,  
1744 Rahn et al., 2016). As will be shown later, aircraft data showed that typical wind speeds parallel  
1745 to clear-cloudy interfaces were near or greater than  $10 \text{ m s}^{-1}$  (Fig. 1312).

1746 ~~Several parameters followed  $V_{850}$  in ranking with  $PD_{GRArea}$  ranges similar to one another:~~  
1747 ~~PBLH,  $q_{850}$ ,  $MSLP_{anom}$ , and  $U_{850}$ .~~ For PBLH, Figure 12e For PBLH, Figure 11e suggests that above  
1748  $\sim 600 \text{ m}$ ,  $PD_{GRArea}$  is relatively insensitive to positive perturbations in PBLH, but below  $\sim 600 \text{ m}$ ,  
1749 the shallower the MBL, the lower the value of  $PD_{GRArea}$ . This potentially can be attributed to the  
1750 fact that a shallower MBL could be more well-mixed and moisture can get transported from the  
1751 ocean surface to the cloud layer which promotes cloudiness (Albrecht et al., 1995). Figure 12g11g  
1752 shows that for  $MSLP_{anom}$  between  $\sim -560 \text{ Pa}$  and  $\sim -450 \text{ Pa}$ , perturbations do not have much impact  
1753 on  $GR_{Area}$ . However, above  $\sim -450 \text{ Pa}$ ,  $GR_{Area}$  is more susceptible to positive perturbations in  $MSLP$ .  
1754 This confirms that stronger Pacific high conditions in the study region promote the expansion of  
1755 clearing events during the day. ~~Also,  $GR_{Area}$  is highly sensitive to  $MSLP$  anomalies below  $\sim -560$ ;~~  
1756 ~~this can be attributed to a decrease in the dominant pressure system in the region, which is not the~~  
1757 ~~optimal condition to sustain the cloud layer.~~ Based on the  $PD_{GRArea}$  profiles in Fig. 12h11h,  
1758 clearings expanded faster as  $U_{850}$  increased above  $0 \text{ m s}^{-1}$  and decreased below  $-3 \text{ m s}^{-1}$ . Clearing  
1759 growth due to negative zonal winds can be explained by the offshore flow component, however,  
1760 the reason for growth during periods of positive zonal winds is unclear.

1761 There was low variability in the range of  $PD_{GR}$  for the rest of the parameters shown in Fig.  
1762 110:  $AOD_{700}$ ,  $q_{700}$ , and  $\omega_{700}$ . Figure 12i11i shows a decrease in  $PD_{GRArea}$  as  $AOD$  increases up to the  
1763 value of  $\sim 0.12$ , above which  $PD_{GRArea}$  increases as a function of  $AOD$ . While it is expected that  
1764 stronger northerly winds associated with clearing expansion promote higher sea salt fluxes (i.e.,  
1765 higher  $AOD$ ), future work is warranted to investigate as to whether this process subsequently  
1766 depletes cloud water and thins out clouds via expedited drizzle production via broadening of cloud  
1767 droplet size distributions, as already suggested in Section 3.2.

1768 The relationship between  $\omega$  at 700 hPa and  $PD_{GRArea}$  is complex. Brueck et al. (2015)  
1769 suggested that enhanced  $\omega_{700}$  promotes cloudiness due to its link to higher  $LTS$ . Myers and Norris  
1770 (2013) further showed that stronger subsidence can reduce cloud fraction  $CF$  (at fixed inversion  
1771 strength) by pushing down the top of the MBL, which is also supported by Bretherton et al. (2013).  
1772 The  $PD_{GRArea}$  profile of  $\omega_{700}$  exhibited a minimum point near a value of  $0 - 0.2 \text{ Pa s}^{-1}$ , with increases  
1773 in  $GR_{Area}$  below and above that range. The increase in  $PD_{GRArea}$  with higher  $\omega$  values above  $0.2 \text{ Pa}$   
1774  $\text{s}^{-1}$  can be attributed to the negative influence of subsidence on lower cloud fraction  $CF$  (via pushing  
1775 down the top of the MBL) as discussed by Myers and Norris (2013). Conversely, the increase in  
1776  $GR_{Area}$  with decreasing  $\omega$  values below  $0 \text{ Pa s}^{-1}$  can be due to upward motion reducing the strength  
1777 of the inversion capping the MBL, which is important to sustain the cloud deck. Vertical motions

Formatted: Font: Italic

Formatted: Font: Italic

Formatted: Font: Italic

Formatted: Font: Italic

Formatted: Font: Italic

Formatted: Font: Italic

Formatted: Font: Italic

Formatted: Font: Italic

Formatted: Font: Italic

Formatted: Font: Italic

Formatted: Font: Italic

Formatted: Font: Italic

Formatted: Font: Italic

Formatted: Font: Italic

Formatted: Font: Italic

Formatted: Font: Italic

Formatted: Font: Italic

Formatted: Font: Italic

Formatted: Font: Italic

Formatted: Font: Italic

Formatted: Font: Italic

Formatted: Font: Italic

Formatted: Font: Italic

Formatted: Font: Italic

Formatted: Font: Italic

Formatted: Font: Italic

Formatted: Font: Italic

Formatted: Font: Italic

Formatted: Font: Italic

Formatted: Font: Italic

Formatted: Font: Italic

1778 represented by the  $\omega_{700}$  parameter could also induce dynamical circulations affecting cloud top  
1779 processes such as shear and entrainment.

1780 It is important to caution that the interpretation of results from the GBRT simulations are  
1781 speculative and rooted in documented physical relationships between the various parameters  
1782 shown in Figs. 10-11-42 and low cloud behavior. One way to try to validate some of the  
1783 conclusions above is with airborne data for case studies. For instance, in situ data can help  
1784 confirm the nature of factors discussed above during clearing events, including vertically-  
1785 resolved winds, primary marine aerosol fluxes in different wind regimes, humidity and  
1786 temperature of air within and above the MBL, and potential for mixing of air above and below  
1787 the MBL top. The next section is an attempt to conduct this exercise using three airborne case  
1788 studies.

1789  
1790 **3.4 Airborne Case Studies**  
1791

1792 To gain a more detailed perspective on clearings in the study region, three case flights are  
1793 examined from the 2016 FASE airborne campaign. For context, Crosbie et al. (2016) examined  
1794 three different case flights during the 2013 NiCE campaign and provided the following insights,  
1795 which motivated the FASE flights for further statistics: (i) two of the three clearings (RF19 on 1  
1796 August 2013, RF23 on 7 August 2013) were immediately adjacent to the coastline and had reduced  
1797 specific humidity in the MBL on the clearing side, suggestive of dry continental offshore wind  
1798 laterally mixing into and dissipating clouds; (ii) the latter two cases also had enhanced temperature  
1799 in the clear column at cloud-relevant altitudes, which help explain the lack of clouds in the clear  
1800 column; and (iii) the other clearing flight (RF16 on 29 July 2013) had the clearing positioned to  
1801 the west of a cloud deck, which was associated with a CTD event along the coastline to the east of  
1802 the clearing (i.e., southerly surge). ~~This~~The latter case exhibited warmer temperatures in the clear  
1803 column only in the top 100 m of the MBL with similar specific humidity profiles, but with cooler  
1804 and moister air above the inversion base in the clear column. This case was suspected to be linked  
1805 to entrainment and mixing of dry air into the cloud deck to produce the clearing, but it was not a  
1806 case of subsidence/divergence, otherwise the air in the clear column would have been warmer and  
1807 drier above the inversion base.

1808 For the three FASE case flights, the clearing was always situated to the west of a cloud  
1809 deck touching the coastline (Figs. 2, S1-S2). This positioning is reminiscent of NiCE RF16, which  
1810 was less sensitive to lateral entrainment of continental air in comparison to the other two NiCE  
1811 flights. Wind data were decomposed into  $\mu$  and  $\nu$  components to represent speeds that are  
1812 perpendicular and parallel, respectively, to the clear-cloudy interface. Figure 2d illustrates an  
1813 example of how these two components of winds varied during RF09A. There were substantial  
1814 changes in  $\nu$  on the two sides of the clear-cloud border, with stronger northerly winds on the clear  
1815 side, reaching as high as  $20 \text{ m s}^{-1}$ , in contrast to about half that magnitude on the cloudy side. Wind  
1816 speed with the intensity of as high as  $20 \text{ m s}^{-1}$  is close to the values reported in previous studies  
1817 associated with California CLLJs (Parish 2000; Ranjha et al., 2013; Lima et al., 2018).  
1818 Furthermore, wind profiles obtained from soundings (Fig. 12) exhibit the structure similar to CLLJ  
1819 on clearing columns with enhanced horizontal wind speed at the altitude near the MBL top. It is  
1820 noteworthy that the cloud edge tends to reside in the transition region where the near cloud top  
1821 flow becomes similar to CLLJ (Figs. 2d and 12). The same substantial change in  $\nu$  across the

Formatted: Font: Italic

Formatted: Font: Italic

Formatted: Font: Italic

Formatted: Font: Italic

1822 interface was also present in RF08 and RF09B with stronger  $v$  winds always on the clear side.  
1823 There was no substantial change in the  $u$  component of wind speed between the two columns in  
1824 each of the three flights.

1825 To extend upon the possibility of shearing effects, absolute changes in  $v$  ( $(v_1 - v_2)/v$ ) were  
1826 calculated for level legs performed at the clear-cloudy border for the three research flights (Table  
1827 2). For consistency, these calculations were based on level legs of a constant length of ~40 km  
1828 with relatively equal spacing on both sides of the clear-cloudy border.  $(v_1 - v_2)/v$  was calculated by  
1829 multiplying 40 km by the slope of the linear fit of  $v$  versus distance from cloud edge, where  
1830 negative (positive)  $x$  values represent distance away from the edge on the clear (cloud) side. The  
1831 results reveal that the horizontal wind shear was strongest somewhere between mid-cloud and  
1832 cloud top altitudes, with the lowest values at the FT level. The lowest values in the MBL were  
1833 observed in the surface legs. This can be attributed to turbulent transport of the momentum (Zemba  
1834 and Friehe 1987) to the surface and the consequent drop in CLLJ wind speeds in the clear column.  
1835 In addition, Fig. S7 shows absolute horizontal shear ( $dv/dx$ ) as a function of distance from the  
1836 cloud boundary for the parallel component of horizontal wind speed. Horizontal shear profiles for  
1837 all research flights (Fig. S7) are slightly noisy especially at the surface legs, but they show the  
1838 presence of the greatest horizontal wind gradient within 5 km length away from clear-cloudy edge.  
1839 Shear at the clear-cloudy edge, especially at cloud levels, can support clearing growth through  
1840 enhancing the mixing of cloudy and clear air. Crosbie et al. (2016) also showed using the case of  
1841 NiCE RF19 that that mixing of cloudy air with adjacent clear air can be an important contributor  
1842 to cloud erosion and thus expansion of clearings. To probe deeper into the clearing cases, the  
1843 subsequent discussion compares vertically-resolved data on both sides of the clear-cloudy border  
1844 based on soundings and level legs.

### 1846 3.4.1 RF08

1847 RF08 (2 August 2016) represented a case similar to the NiCE RF16 (29 July 2013) case  
1848 study in Crosbie et al. (2016) where cooler and moister air above the inversion in the clear column  
1849 was speculated to be due to entrainment and mixing eroding the cloud rather than subsidence and  
1850 divergence catalyzing cloud dissipation. Of note is that there was rapid infill of cloud the night of  
1851 the NiCE FR16 flight. FASE RF08 data showed that potential temperature was warmer (~1 K) in  
1852 the MBL of the clear column as compared to the cloudy column, while in the FT, the air was  
1853 slightly warmer on the cloudy side (Fig. 4.3.12). SST was also approximately 0.4 K higher in the  
1854 clear column (Table 3). Specific humidity was almost identical in the MBL on both sides, but air  
1855 was moister above the inversion base on the clear side. As noted above, vertical profiles of  $u$   
1856 revealed little difference between the two columns, but  $v$  values were nearly twice as high in the  
1857 clear column extending from the surface to approximately 200 m above cloud top. Surface wind  
1858 speeds were also enhanced on the clear side, which resulted in greater friction velocity ( $u^* = 0.40$   
1859  $m\ s^{-1}$  vs  $0.15\ m\ s^{-1}$  on the cloudy side).

1860 An important feature was the wind maximum in and above the inversion layer on the clear  
1861 side, which resulted in larger vertical shear across the inversion on the clear side ( $5.44\ m\ s^{-1}$ )  
1862 compared with the cloudy side ( $0.8\ m\ s^{-1}$ ) (see  $\Delta U$ , Table 3). The strong shear on the clear side  
1863 likely facilitated mixing of MBL air with drier and warmer FT air. This is supported by a lower  
1864 temperature gradient ( $(\Delta\theta/\Delta z)_{max}$  in the inversion layer of the clear column ( $0.32\ K\ m^{-1}$  ~~vs~~ versus  
1865  $0.38\ K\ m^{-1}$ ), which was thicker than the cloudy column (82 m ~~vs~~ versus 55 m). ~~A further effect of~~  
1866 theThe wind maximum in the clearing ~~was to increase~~ also enhanced moisture advection,  
1867 ~~counteracting~~ which counteracted the accumulation of moisture caused by mixing induced by

Formatted: Font: Italic

Formatted: Font: Italic

Formatted: Font: Italic

Formatted: Font: Italic

Formatted: Font: Italic

Formatted: Font: Italic

Formatted: Font: Italic

Formatted: Font: Italic

Formatted: Font: Italic

Formatted: Font: Italic

1868 vertical shear.- This was most significant at the cloud top level as seen in the largest difference in  
1869 the edge-parallel wind  $/v/$  (Table 2). -In the absence of cloud, the effects of longwave radiative  
1870 cooling close to the cloud top level would be subdued allowing shear-induced mixing to erode the  
1871 sharpness of the inversion. Redistribution of moisture into the inversion also serves to insulate  
1872 lower layers from longwave cooling, further delaying the formation of cloud. The difference in  
1873  $/v/$  was smallest close to the surface, indicating that the wind maximum in the clearing had a  
1874 (comparatively) ~~lesser~~reduced effect in enhancing surface moisture fluxes. Satellite imagery  
1875 confirms that later in the day, the cloud layer filled-in partially where the clearing was with the  
1876 presumed help of nocturnal radiative forcing.

1877 The cloud layer in RF08 was the thinnest (131 m) with the shallowest MBL among all three  
1878 cases. In addition, the lowest  $N_d$  ( $107 \text{ cm}^{-3}$ ), largest  $r_e$  ( $6.6 \mu\text{m}$ ), and highest cloud base rain rate  
1879 ( $0.48 \text{ mm day}^{-1}$ ) was measured in RF08 of all three cases. The enhanced rain can likely explain  
1880 why the surface aerosol concentrations from the PCASP were lowest in RF08 ( $106\text{-}108 \text{ cm}^{-3}$  vs  
1881  $186\text{-}236 \text{ cm}^{-3}$  for the other two flights) even though surface winds were highest, specifically due  
1882 to efficient wet scavenging of aerosols. This possibility is at least linked to the speculation reported  
1883 earlier in Sections 3.2 and 3.3 that stronger northerly winds linked to the growth of clearings result  
1884 in sea salt expediting rain formation in clouds and thus thinning them out. In support of this notion,  
1885 cloud water composition results are of relevance as they provide an indication of the relative  
1886 influence of giant  $CCN$  ( $GCCN$ ) in the form of sea salt, as previously demonstrated in the region  
1887 by Dadashazar et al. (2017). The combined concentration of sodium ( $Na^+$ ) and chloride ( $Cl^-$ ) was  
1888  $60 \mu\text{g m}^{-3}$ ,  $33 \mu\text{g m}^{-3}$ , and  $64 \mu\text{g m}^{-3}$  for RF08, RF09A, and RF09B, respectively. In contrast, the  
1889 average combined sum of  $Na^+$  and  $Cl^-$  for all samples collected in FASE was  $14 \mu\text{g m}^{-3}$ . Based on  
1890 a two-tailed student's t-test with 95% confidence, the means of RF08 and RF09B were  
1891 significantly different than the mean of all FASE samples. The  $Cl^-:Na^+$  mass ratios in all three  
1892 FASE clearing flights (RF08 = 1.80, RF09A = 1.78, RF09B = 1.79) were very close or matching  
1893 that of pure sea salt (1.81), providing more confidence that sea salt was impacting these clouds via  
1894 serving as  $CCN$ . The cloud water results are in support of  $GCCN$  enhancing drizzle in RF08 and  
1895 thus thinning out clouds and removing aerosol underneath the cloud base. It is unclear with this  
1896 dataset though as to what role the impact of sea salt in depleting clouds of their water had to do  
1897 with the actual clearing, but at least there is support for this process potentially impacting the  
1898 cloudy column. ~~Consistent with the NiCE clearing cases, aerosol concentrations were relatively~~  
1899 ~~similar on both sides of the clear-cloudy border for all three FASE cases.~~

1900 Figure 44S8 shows vertical profiles of aerosol concentrations on both sides of the clearing  
1901 border, highlighting differences above cloud top level especially in RF09A and RF09B with higher  
1902 values in the cloudy column. Higher aerosol concentrations were also observed in the cloud  
1903 column in the sub-cloud layer even though surface wind speeds were always higher in the clear  
1904 column for all three flights. Surface winds and thus sea spray production do not exclusively  
1905 influence the aerosol concentrations. A likely explanation of higher concentrations in the MBL in  
1906 the cloudy column is that there could be entrainment of more polluted free tropospheric aerosol as  
1907 has been reported to be a common occurrence during the FASE flights (Mardi et al., 2019). As  
1908 also reported during FASE, there can be sub-cloud evaporation of drizzle resulting in droplet  
1909 residual particles that contribute to the aerosol concentration budget in the cloudy column  
1910 (Dadashazar et al., 2018).

1911 Figure 13 displays turbulence parameters such as variance in the three components of wind  
1912 speed (Fig. 44a13a-c), turbulent kinetic energy (Fig. 13d), and buoyancy flux (Fig. 44d13e).  
1913 Stronger horizontal wind ~~speeds~~speed gradients, and consequently stronger shear production, near

Formatted: Font: Italic

Formatted: Font: Italic

Formatted: Font: Italic

Formatted: Font: Italic

Formatted: Font: Italic

Formatted: Font: Italic

Formatted: Font: Italic

Formatted: Font: Italic

Formatted: Font: Italic

Formatted: Font: Italic

Formatted: Font: Italic

Formatted: Font: Italic

Formatted: Font: Italic

1914 the surface on the clear side resulted in greater variance in the horizontal wind components at all  
1915 MBL levels. Both  $\overline{u'^2}$  and  $\overline{v'^2}$  exhibit a general downward trend with increasing altitude, which  
1916 is also supportive of shear driven turbulence. On the other hand,  $\overline{w'^2}$ , which is closely associated  
1917 with cloud layer properties, exhibits a different trend on the cloudy side as it increases from cloud  
1918 base to mid-cloud level. For surface and above cloud base levels,  $\overline{w'^2}$  is higher in the clear column  
1919 likely due to the combined influence of shear and buoyancy terms on the turbulence budget. On  
1920 the other hand, in the mid-cloud layer,  $\overline{w'^2}$  is slightly higher (Fig. 14e13c) in the cloudy column  
1921 as compared to clear one column, which can be attributed to the buoyancy flux (Fig. 14d13e). It is  
1922 also interesting to note that RF08 is the only flight with a minimum in  $\overline{w'^2}$  being at the level  
1923 above cloud base in the cloudy column relative to other MBL levels. This is most likely due to  
1924 lower buoyancy production in the cloud layer of RF08 as compared to the other flights.

1925 To further investigate the relative role of each buoyancy and shear term in the turbulence  
1926 budget, the  $\overline{z'w'}/LMO$  ratio was compared between the two columns (Table 3). This ratio is an order  
1927 of magnitude greater in the cloudy column as compared to clear one due to the latter column having  
1928 stronger shear and reduced buoyancy flux. This confirms that shear is most likely the dominant  
1929 mechanism for turbulence production in the clear column in the absence of the cloud layer.

1930

### 1931 3.4.2 RF09A and RF09B

1932 The two flights on 3 August 2016 allowed for an opportunity to contrast clearing properties  
1933 at two different times on the same day at roughly the same location (~20 km apart). Owing to their  
1934 similarities, they are discussed together here. The clearing module in RF09A was performed  
1935 between 11:00 and 12:30 PST, while that during RF09B was performed between 15:00 - 17:00  
1936 PST. Similar to RF08, MBL air in the clear column of RF09A and RF09B was slightly warmer  
1937 than the cloudy column; however, the magnitude of the temperature difference (clear – cloudy)  
1938 decreased from RF09A (~1.1K) to RF09B (~0.8K). SST was also greater by 0.4 K in the clear  
1939 column of RF09A as compared to the cloud column, while it was slightly cooler by 0.1 K in the  
1940 clear column of RF09B.

1941 Specific humidity profiles in RF09A/RF09B exhibit more subtle differences as compared  
1942 to RF08. In contrast to RF08, air in RF09A above the inversion base was drier and warmer in the  
1943 region immediately above the inversion base and differences above the inversion base are less  
1944 clear for RF09B. During both RF09A and RF09B, the clear profile exhibited steadily decreasing  
1945 levels of water vapor with altitude, while the cloudy column was more well-mixed. The  $v'$   
1946 component of wind speed again exhibited substantially greater values in the clear column as  
1947 compared to the cloudy column for both RF09A and RF09B. Looking at the inversion layer  
1948 properties (Table 3), the temperature gradient was lower and shear was greater in the clear column  
1949 of RF09A and RF09B. Inversion depth was also greater in the clear column of RF09A, but less so  
1950 for RF09B.

1951 The sounding data in RF09A qualitatively resemble those from NiCE RF19 on 1 August  
1952 2013 where Crosbie et al. (2016) suspected that there was increased local subsidence and  
1953 divergence in the clear column. Similar to their case, we observed the following in the clear column  
1954 of RF09A: (i) warmer and drier air above and below the inversion base; (ii) the inversion base  
1955 height was lower (354 m ~~vs~~versus 375 m) with reduced temperature gradient in the inversion layer  
1956 (0.33 K km<sup>-1</sup> ~~vs~~versus 0.41 K km<sup>-1</sup>); and (iii) potential temperature exhibited warming and drying  
1957 in the layer equivalent to the top 100 m of cloud. The RF09B case differed in that above the

Formatted: Font: Italic

Formatted: Font: Italic

Formatted: Font: Italic



1958 inversion base, the air in the clear column was not warmer and drier but very slightly cooler and  
1959 moister, similar to RF08. This potentially is due to the diurnal nature of the clearing system where  
1960 there is a stronger forcing to dissipate clouds during mid-day with the help of subsidence of dry  
1961 and warm air from the FT, whereas later in the afternoon that process switches to a scenario where  
1962 cooler and moister air exists above the inversion base and there is a waiting process for stronger  
1963 radiative forcing to form a cloud again.

1964 The cloud layer is the thickest in RF09A (191 m) among all three case flights. The cloud  
1965 layer became thinner (137 m) later in the day during RF09B as a result of a change in the lifting  
1966 condensation level (*LCL*), where cloud base increased from 217 m to 265 m. Moreover, *LWP*  
1967 decreased during the day from  $32 \text{ g m}^{-2}$  to  $18 \text{ g m}^{-2}$ . It is important to note that the adiabaticity  
1968 parameter, defined as the ratio of measured *LWP* to *LWP* of an adiabatic cloud, exhibited values  
1969 of 0.75, 0.76, and 0.83 for RF08, RF09A, and RF09B, respectively. These adiabaticity values are  
1970 close to the average value of 0.766 for the region reported in Braun et al. (2018). The clouds were  
1971 quite thin near the interface based on the relatively low values of *LWP* in contrast to typical  
1972 conditions observed in the region based on airborne measurements in the same campaigns (Fig. 3  
1973 of Sorooshian et al., 2019). Other cloud properties such as  $N_d$ ,  $r_e$ , and rain rate were quite similar  
1974 in both RF09A and RF09B.  $N_d$  was greater in RF09A and RF09B as compared to RF08,  
1975 corresponding to smaller values of  $r_e$  and suppressed drizzle. The dataset cannot provide  
1976 unambiguous evidence as to whether the higher surface aerosol concentrations in RF09A and  
1977 RF09B, as compared to RF08, were due to (or led to) suppressed drizzle.

1978 Profiles of  $u'^2$  and  $v'^2$  exhibited downward trends with increasing altitude for RF09A  
1979 and RF09B, in general agreement with the findings for RF08. One contrasting aspect was the  
1980 comparison of  $v'^2$  between clear and cloudy columns, which mirrored RF08 during RF09A, while  
1981 in RF09B, the values of  $v'^2$  for the clear side were substantially lower. In addition,  $w'^2$  profiles  
1982 during RF09A and RF09B are substantially enhanced in the cloudy column as compared to RF08,  
1983 with maxima in the cloud layer. There is an accompanying increase in the buoyancy flux for these  
1984 profiles suggestive of a more significant contribution of buoyancy to *TKE* production. (Fig. 13e).

1985 Although more subtle,  $u'^2$  values also showed an increase in the cloudy ~~columns~~ column of  
1986 RF09A and RF09B relative to the clear column, also supportive of the role of buoyancy in these  
1987 cases. In addition, *TKE* profiles (Fig. 13d) were largely influenced by variances in the horizontal  
1988 component of wind speed ( $u'^2$  and  $v'^2$ ) which led to overall greater *TKE* values in the clear  
1989 column except for RF09B.

1990 Drizzle may be an important factor in governing the differences in buoyancy between the  
1991 cloudy columns of RF09A/B and RF08, ~~by creating a stabilizing effect.~~ While no obvious  
1992 decoupling of the RF08 cloudy MBL is observed, this profile may rely more heavily on shear  
1993 production to maintain a well-mixed state. The clearing persisted following RF08, while there  
1994 was a rapid infilling of cloud during the night following RF09A/B, similar to the case presented  
1995 by Crosbie et al. (2016), which was also non-drizzling. While the nocturnal radiative environment  
1996 has been shown to be conducive to infilling of clearings, we hypothesize that other factors that  
1997 promote tighter coupling between the cloud layer and the surface (such as a lack of drizzle) may  
1998 also contribute.

1999  
2000  
2001

Formatted: Font: Italic

Formatted: Font: Italic

Formatted: Font: Italic

Formatted: Font: Italic

Formatted: Font: Italic

Formatted: Font: Italic

Formatted: Font: Italic

Formatted: Font: Italic

Formatted: Font: Italic

Formatted: Font: Italic

2002 **4 Conclusions**

2003 This study extends upon recent works interested in large stratocumulus clearings that  
2004 significantly impact albedo and have implications for fog, cloud, and weather forecasting. We  
2005 specifically reported on ten years (2009-2018) of satellite and reanalysis data to characterize the  
2006 temporal behavior, spatial and dimensional characteristics, growth rates, and governing  
2007 environmental properties controlling the growth of clearings off the U.S. West Coast. We also  
2008 examined three case flights from the 2016 FASE campaign that probed clearings to gain a deeper  
2009 insight at finer spatial scales to try to validate speculated links between environmental parameters  
2010 and clearing growth rates based on machine learning simulations using satellite and reanalysis  
2011 data. The major results were as follows:

- 2012
- 2013 (i) Summertime (wintertime) experiences the highest (lowest) frequency of clearings ~~visible~~  
2014 ~~from spaces suggested by satellite retrievals.~~
  - 2015 (ii) The centroid of clearings is ~~entered~~located around coastal topographical features along  
2016 the California coastline, specifically Cape Blanco and Cape Mendocino.
  - 2017 (iii) The median length, width, and area of clearings between 09:00 and 18:00 (PST) increased  
2018 from 680 km, 193 km, and ~67,000 km<sup>2</sup>, respectively, to ~1231 km, 443 km, and ~250,000  
2019 km<sup>2</sup>. The most growth occurred between 09:00-12:00.
  - 2020 (iv) The most influential factors in clearing growth rates of total area between 09:00-12:00 were  
2021  ~~$T_{850}$ ,  $q_{950}$ ,  $SST$ , and  $V_{850}$~~  $MSLP_{anom}$  using two different scoring methods. Compared to non-  
2022 clearing days, clearing days were characterized by having an enhanced Pacific high shifted  
2023 more towards northern California, offshore air that is warm and dry, faster coastal surface  
2024 winds, higher lower tropospheric static stability, and stronger subsidence.
  - 2025 (v) Clearing days exhibited higher values of  $N_d$  and reduced values of  $r_e$ ,  $\tau$ , and  $LWP$  near the  
2026 California coast where clearings form and evolve. However, the mean cloud albedo over  
2027 the entire study domain was actually higher on clearing days.
  - 2028 (vi) Airborne data revealed that extensive horizontal shear at cloud-relevant altitudes, with  
2029 much faster winds with low-level jet structure parallel to the clearing edge on the clear side  
2030 as compared to the cloudy side. This helped to promote mixing and thus dissipation of  
2031 clouds. Differences in sounding profiles reveal that warm and dry air in the free troposphere  
2032 additionally promoted expansion of clearings.

2033 More research is needed to further characterize clearings and the broader regions they  
2034 evolve in. For instance, it remains uncertain as to if there is a physical link between the existence  
2035 of clearings and a higher domain-wide cloud albedo on clearing days. More data such as those  
2036 provided by GOES platforms can help understand processes occurring at the microscale that scale  
2037 up to more climatologically relevant scales. The results of this work showed that there are  
2038 important diurnal features that require additional examination with in situ observations. One of the  
2039 hypotheses posed in this work requiring more measurements and statistical robustness is the link  
2040 between sea salt aerosol and the formation and evolution of clearing events. Clearing days are  
2041 characterized by having stronger northerly winds, which translate into higher sea spray fluxes,  
2042 ~~which and~~ subsequently can impact clouds via faster onset of drizzle. This chain of events  
2043 subsequently can thin out clouds via depletion of cloud water. Targeted experiments to examine  
2044 these types of events will help advance understanding about their nature, which can then be  
2045 contrasted with clearings along other coastal regions such as the southeastern Atlantic Ocean. Also,  
2046 the nature of clearings has direct relevance to CTD events that evolve in similar regions as  
2047 discussed by Juliano et al. (2019a,b).

Formatted: Font: Italic

Formatted: Font: Italic

Formatted: Font: Italic

Formatted: Font: Italic

Formatted: Font: Italic

Formatted: Font: Italic

Formatted: Font: Italic

Formatted: Indent: First line: 0.5"

2048 **Data availability**

2049 Airborne field data used in this work can be found on the Figshare database (Sorooshian et al.,  
2050 2017; [https://figshare.com/articles/A\\_Multi-Year\\_Data\\_Set\\_on\\_Aerosol-Cloud-Precipitation-  
2051 Meteorology\\_Interactions\\_for\\_Marine\\_Stratocumulus\\_Clouds/5099983](https://figshare.com/articles/A_Multi-Year_Data_Set_on_Aerosol-Cloud-Precipitation-Meteorology_Interactions_for_Marine_Stratocumulus_Clouds/5099983)). Also, the ~~satellite and  
2052 reanalysis~~ other data used ~~can be obtained from~~ in this study are available at websites ~~listed~~ provided  
2053 in ~~Sections 2.1-2, Section 2.~~  
2054

2055 **Author contributions**

2056 ~~EC, XZ,~~ and AS designed the study. HJ, AS, EC, and HD conducted the research flights ~~in~~ during  
2057 the FASE field campaign. MSM and HD developed the image analysis tool to analyze GOES  
2058 images. MP, HD, and MAM ~~conducted~~ ran the GBRT model. HD analyzed the collected data. AB,  
2059 MB, and XZ provided ~~inputs for various part of project~~ input on the results and draft. AS and HD  
2060 wrote the paper. EC, MAM, AB, MB, and XZ revised the manuscript.  
2061

2062 **Competing interests**

2063 The authors declare that they have no conflict of interest.  
2064

2065 **Acknowledgments**

2066 This work was funded by Office of Naval Research grant N00014-16-1-2567 and NASA grants  
2067 NNX14AM02G and 80NSSC19K0442, the latter of which is in support of the ACTIVATE Earth  
2068 Venture Suborbital-3 (EVS-3) investigation, which is funded by NASA's Earth Science Division  
2069 and managed through the Earth System Science Pathfinder Program Office.  
2070

2071 [We acknowledge Johannes Mohrmann and an anonymous reviewer for their constructive  
2072 feedback.](#)



2073 **References**

2074  
2075 Albrecht, B. A.: Parameterization of Trade-Cumulus Cloud Amounts, J Atmos Sci, 38, 97-105,  
2076 [Doi 10.1175/1520-0469,https://doi.org/10.1175/1520-](https://doi.org/10.1175/1520-0469(1981)038<0097:POTCCA>2.0.CO;2)  
2077 [0469\(1981\)038<0097:POTCCA>2.0.CO;2](https://doi.org/10.1175/1520-0469(1981)038<0097:POTCCA>2.0.CO;2), 1981.

2078  
2079 [Albrecht, B. A., Fairall, C. W., Thomson, D. W., White, A. B., Snider, J. B., and Schubert, W.](https://doi.org/10.1029/GL017i001p00089)  
2080 [H.: Surface-Based Remote-Sensing of the Observed and the Adiabatic Liquid Water-Content of](https://doi.org/10.1029/GL017i001p00089)  
2081 [Stratocumulus Clouds, Geophys Res Lett, 17, 89-92, https://doi.org/10.1029/GL017i001p00089,](https://doi.org/10.1029/GL017i001p00089)  
2082 [1990.](https://doi.org/10.1029/GL017i001p00089)

2083  
2084 Albrecht, B. A., Jensen, M. P., and Syrett, W. J.: Marine Boundary-Layer Structure and  
2085 Fractional Cloudiness, J Geophys Res-Atmos, 100, 14209-14222, [Doi](https://doi.org/10.1029/95JD00827)  
2086 [10.1029/95JD00827,https://doi.org/10.1029/95JD00827](https://doi.org/10.1029/95JD00827), 1995.

2087  
2088 [Beardsley, R. C., Dorman, C. E., Friehe, C. A., Rosenfeld, L. K., and Winant, C. D.: Local](https://doi.org/10.1029/JC092iC02p01467)  
2089 [Atmospheric Forcing during the Coastal Ocean Dynamics Experiment .1. A Description of the](https://doi.org/10.1029/JC092iC02p01467)  
2090 [Marine Boundary-Layer and Atmospheric Conditions over a Northern California Upwelling](https://doi.org/10.1029/JC092iC02p01467)  
2091 [Region, J Geophys Res-Oceans, 92, 1467-1488, https://doi.org/10.1029/JC092iC02p01467,](https://doi.org/10.1029/JC092iC02p01467)  
2092 [1987.](https://doi.org/10.1029/JC092iC02p01467)

2093  
2094 Bennartz, R.: Global assessment of marine boundary layer cloud droplet number concentration  
2095 from satellite, J Geophys Res-Atmos, 112, Artn D02201,  
2096 [10.1029/2006JD007547,https://doi.org/10.1029/2006JD007547](https://doi.org/10.1029/2006JD007547), 2007.

2097  
2098 [Bosilovich, M. G., Lucchesi, R., and Suarez, M. : MERRA-2: File specification. GMAO Office](https://gmao.gsfc.nasa.gov/pubs/docs/Bosilovich785.pdf)  
2099 [Note No. 9 \(Version 1.1\), 73 pp, 2016, available from](https://gmao.gsfc.nasa.gov/pubs/docs/Bosilovich785.pdf)  
2100 <https://gmao.gsfc.nasa.gov/pubs/docs/Bosilovich785.pdf>

2101  
2102 Braun, R. A., Dadashazar, H., MacDonald, A. B., Crosbie, E., Jonsson, H. H., Woods, R. K.,  
2103 Flagan, R. C., Seinfeld, J. H., and Sorooshian, A.: Cloud Adiabaticity and Its Relationship to  
2104 Marine Stratocumulus Characteristics Over the Northeast Pacific Ocean, J Geophys Res-Atmos,  
2105 123, 13790-13806, [10.1029/2018JD029287,https://doi.org/10.1029/2018JD029287](https://doi.org/10.1029/2018JD029287), 2018.

2106  
2107 [Bretherton, C. S., and M. C. Wyant: Moisture transport, lower-tropospheric stability, and](https://doi.org/10.1175/1520-0469(1997)054<0148:MTL TSA>2.0.CO;2)  
2108 [decoupling of cloud-topped boundary layers, J Atmos Sci, 54, 148-167,](https://doi.org/10.1175/1520-0469(1997)054<0148:MTL TSA>2.0.CO;2)  
2109 [https://doi.org/10.1175/1520-0469\(1997\)054<0148:MTL TSA>2.0.CO;2](https://doi.org/10.1175/1520-0469(1997)054<0148:MTL TSA>2.0.CO;2), 1997.

2110  
2111 Bretherton, C. S., Klinker, E., Betts, A. K., and Coakley, J. A.: Comparison of Ceilometer,  
2112 Satellite, and Synoptic Measurements of Boundary-Layer Cloudiness and the ECMWF Diagnostic  
2113 Cloud Parameterization Scheme during ASTEX, J Atmos Sci, 52, 2736-2751, [Doi 10.1175/1520-](https://doi.org/10.1175/1520-0469(1995)052<2736:COCSAS>2.0.CO;2)  
2114 [0469,https://doi.org/10.1175/1520-0469\(1995\)052<2736:COCSAS>2.0.CO;2](https://doi.org/10.1175/1520-0469(1995)052<2736:COCSAS>2.0.CO;2), 1995.

2115

**Formatted:** Left, Space After: 8 pt, Line spacing: Multiple 1.08 li, Adjust space between Latin and Asian text, Adjust space between Asian text and numbers

**Formatted:** Font: Arial, 10.5 pt, Font color: Custom Color(RGB(118,118,118)), Pattern: Clear (White)

**Formatted:** Font: (Default) +Body (Calibri), 11 pt

**Formatted:** Don't adjust space between Latin and Asian text, Don't adjust space between Asian text and numbers

**Formatted:** Font: Not Bold

**Formatted:** Add space between paragraphs of the same style

**Formatted:** Left, Space After: 8 pt, Line spacing: Multiple 1.08 li, Adjust space between Latin and Asian text, Adjust space between Asian text and numbers

**Formatted:** Font: Arial, 10.5 pt, Font color: Custom Color(RGB(118,118,118)), Pattern: Clear (White)

**Formatted:** Font: (Default) +Body (Calibri), 11 pt

2116 Bretherton, C. S., Blossey, P. N., and Jones, C. R.: Mechanisms of marine low cloud sensitivity  
 2117 to idealized climate perturbations: A single-LES exploration extending the CGILS cases, J Adv  
 2118 Model Earth Sy, 5, 316-337, ~~10.1002/jame.20019~~, <https://doi.org/10.1002/jame.20019>, 2013.  
 2119  
 2120 Brueck, M., Nuijens, L., and Stevens, B.: On the Seasonal and Synoptic Time-Scale Variability of  
 2121 the North Atlantic Trade Wind Region and Its Low-Level Clouds, J Atmos Sci, 72, 1428-1446,  
 2122 ~~10.1175/Jas-D-14-0054.1~~, <https://doi.org/10.1175/JAS-D-14-0054.1>, 2015.  
 2123  
 2124 Brunke, M. A., Ma, P. - L., Reeves Eyre, J. E. J., Rasch, P. J., Sorooshian, A., and Zeng, X.:  
 2125 Subtropical marine low stratiform cloud deck spatial errors in the E3SMv1 Atmosphere Model,  
 2126 Geophys Res-Letters, 46, <https://doi.org/10.1029/2019GL084747>, 2019.  
 2127  
 2128 ~~Buchard, V., da Silva, A. M., Colarco, P. R., Darmenov, A., Randles, C. A., Govindaraju, R., . . .~~  
 2129 ~~Spurr, R. (2015). Using the OMI Aerosol Index and Absorption Aerosol Optical Depth to~~  
 2130 ~~Evaluate the NASA MERRA Aerosol Reanalysis. Atmospheric Chemistry and Physics, 15(10),~~  
 2131 ~~5743-5760, https://doi.org/10.5194/acp-15-5743-2015, 2015.~~  
 2132  
 2133 ~~Burk, S. D., and W. T. Thompson: The summertime low-level jet and marine boundary layer~~  
 2134 ~~structure along the California coast, Mon Wea Rev, 124, 668–686, https://doi.org/10.1175/1520-~~  
 2135 ~~0493(1996)124.0668:TSLJLA.2.0.CO;2, 1996.~~  
 2136  
 2137 ~~Chin, M., Ginoux, P., Kinne, S., Torres, O., Holben, B. N., Duncan, B. N., Martin, R. V., Logan,~~  
 2138 ~~J. A., Higurashi, A., and Nakajima, T.: Tropospheric aerosol optical thickness from the~~  
 2139 ~~GOCART model and comparisons with satellite and Sun photometer measurements, J Atmos~~  
 2140 ~~Sci, 59, 461-483, https://doi.org/10.1175/1520-0469(2002)059<0461:TAOTFT>2.0.CO;2, 2002.~~  
 2141  
 2142 ~~Bosilovich, M. G., Lucchesi, R., and Suarez, M.: MERRA 2: File specification. GMAO Office~~  
 2143 ~~Note No. 9 (Version 1.1), 73 pp., 2016, available from~~  
 2144 ~~[http://gmao.gsfc.nasa.gov/pubs/office\\_notes](http://gmao.gsfc.nasa.gov/pubs/office_notes).~~  
 2145  
 2146 Coakley, J. A., Durkee, P. A., Nielsen, K., Taylor, J. P., Platnick, S., Albrecht, B. A., Babb, D.,  
 2147 Chang, F. L., Tahnk, W. R., Bretherton, C. S., and Hobbs, P. V.: The appearance and disappearance  
 2148 of ship tracks on large spatial scales, J Atmos Sci, 57, 2765-2778, ~~Doi 10.1175/1520-~~  
 2149 ~~0469~~, [https://doi.org/10.1175/1520-0469\(2000\)057<2765:TAADOS>2.0.CO;2](https://doi.org/10.1175/1520-0469(2000)057<2765:TAADOS>2.0.CO;2), 2000.  
 2150  
 2151 Coggon, M. M., Sorooshian, A., Wang, Z., Craven, J. S., Metcalf, A. R., Lin, J. J., Nenes, A.,  
 2152 Jonsson, H. H., Flagan, R. C., and Seinfeld, J. H.: Observations of continental biogenic impacts  
 2153 on marine aerosol and clouds off the coast of California, J Geophys Res-Atmos, 119, 6724-6748,  
 2154 ~~10.1002/2013JD021228~~, <https://doi.org/10.1002/2013JD021228>, 2014.  
 2155  
 2156 Crosbie, E., Wang, Z., Sorooshian, A., Chuang, P. Y., Craven, J. S., Coggon, M. M., Brunke, M.,  
 2157 Zeng, X. B., Jonsson, H., Woods, R. K., Flagan, R. C., and Seinfeld, J. H.: Stratocumulus Cloud  
 2158 Clearings and Notable Thermodynamic and Aerosol Contrasts across the Clear-Cloudy Interface,  
 2159 J Atmos Sci, 73, 1083-1099, ~~10.1175/Jas-D-15-0137.1~~, <https://doi.org/10.1175/JAS-D-15-0137.1>,  
 2160 2016.  
 2161

**Formatted:** Hyperlink, Font: (Default) +Headings CS (Times New Roman), 11 pt

**Formatted:** Font: Not Bold

**Formatted:** Don't adjust space between Latin and Asian text, Don't adjust space between Asian text and numbers

**Formatted:** Space After: 0 pt, Add space between paragraphs of the same style

2162 Crosbie, E., Brown, M. D., Shook, M., Ziemba, L., Moore, R. H., Shingler, T., Winstead, E.,  
2163 Thornhill, K. L., Robinson, C., MacDonald, A. B., Dadashazar, H., Sorooshian, A., Beyersdorf,  
2164 A., Eugene, A., Collett, J., Straub, D., and Anderson, B.: Development and characterization of a  
2165 high-efficiency, aircraft-based axial cyclone cloud water collector, *Atmos Meas Tech*, 11, 5025-  
2166 5048, <https://doi.org/10.5194/amt-11-5025-2018>, 2018.

**Formatted:** Hyperlink, Font: (Default) +Headings CS (Times New Roman), 11 pt

2168 Dadashazar, H., Wang, Z., Crosbie, E., Brunke, M., Zeng, X. B., Jonsson, H., Woods, R. K.,  
2169 Flagan, R. C., Seinfeld, J. H., and Sorooshian, A.: Relationships between giant sea salt particles  
2170 and clouds inferred from aircraft physicochemical data, *J Geophys Res-Atmos*, 122, 3421-3434,  
2171 [10.1002/2016JD026019](https://doi.org/10.1002/2016JD026019), <https://doi.org/10.1002/2016JD026019>, 2017.

**Formatted:** Left, Space After: 8 pt, Line spacing: Multiple 1.08 li, Adjust space between Latin and Asian text, Adjust space between Asian text and numbers

**Formatted:** Font: Arial, 10.5 pt, Font color: Custom Color(RGB(118,118,118)), Pattern: Clear (White)

**Formatted:** Font: (Default) +Body (Calibri), 11 pt

2172  
2173 [Dadashazar, H., Braun, R. A., Crosbie, E., Chuang, P. Y., Woods, R. K., Jonsson, H. H., and](https://doi.org/10.5194/acp-18-1495-2018)  
2174 [Sorooshian, A.: Aerosol characteristics in the entrainment interface layer in relation to the](https://doi.org/10.5194/acp-18-1495-2018)  
2175 [marine boundary layer and free troposphere. \*Atmos Chem Phys\*, 18, 1495-1506, 10.5194/acp-18-](https://doi.org/10.5194/acp-18-1495-2018)  
2176 [1495-2018, 2018.](https://doi.org/10.5194/acp-18-1495-2018)

**Formatted:** Font: (Default) Segoe UI, 9 pt

2177  
2178 Durkee, P. A., Noone, K. J., Ferek, R. J., Johnson, D. W., Taylor, J. P., Garrett, T. J., Hobbs, P.  
2179 V., Hudson, J. G., Bretherton, C. S., Innis, G., Frick, G. M., Hoppel, W. A., O'Dowd, C. D.,  
2180 Russell, L. M., Gasparovic, R., Nielsen, K. E., Tessmer, S. A., Ostrom, E., Osborne, S. R., Flagan,  
2181 R. C., Seinfeld, J. H., and Rand, H.: The impact of ship-produced aerosols on the microstructure  
2182 and albedo of warm marine stratocumulus clouds: A test of MAST hypotheses Ii and Iii, *J Atmos*  
2183 *Sci*, 57, 2554-2569, [Doi 10.1175/1520-0469](https://doi.org/10.1175/1520-0469(2000)057<2554:TIOSPA>2.0.CO;2), [https://doi.org/10.1175/1520-](https://doi.org/10.1175/1520-0469(2000)057<2554:TIOSPA>2.0.CO;2)  
2184 [0469\(2000\)057<2554:TIOSPA>2.0.CO;2](https://doi.org/10.1175/1520-0469(2000)057<2554:TIOSPA>2.0.CO;2), 2000.

**Formatted:** Space After: 0 pt, Add space between paragraphs of the same style

2185  
2186 [Elith, J., Leathwick, J. R., and Hastie, T.: A working guide to boosted regression trees, \*J Anim\*](https://doi.org/10.1111/j.1365-2656.2008.01390.x)  
2187 [Ecol, 77, 802-813, <https://doi.org/10.1111/j.1365-2656.2008.01390.x>, 2008.](https://doi.org/10.1111/j.1365-2656.2008.01390.x)

2188  
2189 [Edwards, K. A., Rogerson, A. M., Winant, C. D., and Rogers, D. P.: Adjustment of the marine](https://doi.org/10.1175/1520-0469(2001)058<1511:AOTMAB>2.0.CO;2)  
2190 [atmospheric boundary layer to a coastal cape, \*J Atmos Sci\*, 58, 1511-1528,](https://doi.org/10.1175/1520-0469(2001)058<1511:AOTMAB>2.0.CO;2)  
2191 [https://doi.org/10.1175/1520-0469\(2001\)058<1511:AOTMAB>2.0.CO;2](https://doi.org/10.1175/1520-0469(2001)058<1511:AOTMAB>2.0.CO;2), 2001.

2192  
2193 Friedman, J. H.: Greedy function approximation: A gradient boosting machine, *Ann Stat*, 29(5),  
2194 1189-1232, 2001.

**Formatted:** Space After: 0 pt

2195  
2196 [Friedman, J. H., and Meulman, J. J.: Multiple additive regression trees with application in](https://doi.org/10.1002/sim.1501)  
2197 [epidemiology, \*Stat Med\*, 22, 1365-1381, <https://doi.org/10.1002/sim.1501>, 2003.](https://doi.org/10.1002/sim.1501)

2198  
2199 Fuchs, J., Cermak, J., and Andersen, H.: Building a cloud in the southeast Atlantic: understanding  
2200 low-cloud controls based on satellite observations with machine learning, *Atmos Chem Phys*, 18,  
2201 16537-16552, <https://doi.org/10.5194/acp-18-16537-2018>, 2018.

**Formatted:** Hyperlink, Font: (Default) +Headings CS (Times New Roman), 11 pt

2202  
2203 [Garreaud, R. D., and Munoz, R. C.: The low-level jet off the west coast of subtropical South](https://doi.org/10.1175/Mwr2972.1)  
2204 [America: Structure and variability, \*Mon Weather Rev\*, 133, 2246-2261,](https://doi.org/10.1175/Mwr2972.1)  
2205 <https://doi.org/10.1175/Mwr2972.1>, 2005.

**Formatted:** Font: (Default) Segoe UI, 9 pt

**Formatted:** Space After: 0 pt, Add space between paragraphs of the same style

2207 Gelaro, R., McCarty, W., Suarez, M. J., Todling, R., Molod, A., Takacs, L., Randles, C. A.,  
2208 Darnenov, A., Bosilovich, M. G., Reichle, R., Wargan, K., Coy, L., Cullather, R., Draper, C.,  
2209 Akella, S., Buchard, V., Conaty, A., da Silva, A. M., Gu, W., Kim, G. K., Koster, R., Lucchesi,  
2210 R., Merkova, D., Nielsen, J. E., Partyka, G., Pawson, S., Putman, W., Rienecker, M., Schubert, S.  
2211 D., Sienkiewicz, M., and Zhao, B.: The Modern-Era Retrospective Analysis for Research and  
2212 Applications, Version 2 (MERRA-2), J Climate, 30, 5419-5454, <https://doi.org/10.1175/Jcli-D-16-0758.1>, 2017.

**Formatted:** Hyperlink, Font: (Default) +Headings CS (Times New Roman), 11 pt

2215 Gerber, H., Arends, B. G., and Ackerman, A. S.: New microphysics sensor for aircraft use, Atmos  
2216 Res, 31, 235-252, ~~Doi~~ [https://doi.org/10.1016/0169-8095\(94\)90001-9](https://doi.org/10.1016/0169-8095(94)90001-9), 1994.

**Formatted:** Hyperlink, Font: (Default) +Headings CS (Times New Roman), 11 pt

2217 [Haack, T., Burk, S. D., Dorman, C., and Rogers, D.: Supercritical flow interaction within the  
2218 Cape Blanco-Cape Mendocino Orographic Complex, Mon Weather Rev, 129, 688-708,  
2219 \[https://doi.org/10.1175/1520-0493\\(2001\\)129<0688:SFIWTC>2.0.CO;2\]\(https://doi.org/10.1175/1520-0493\(2001\)129<0688:SFIWTC>2.0.CO;2\), 2001.](https://doi.org/10.1175/1520-0493(2001)129<0688:SFIWTC>2.0.CO;2)

2221 Hahn, C. J., and S. G. Warren: A gridded climatology of clouds over land (1971–96) and ocean  
2222 (1954–97) from surface observations worldwide. Numeric Data Package NDP-026E  
2223 ORNL/CDIAC-153, CDIAC, Department of Energy, Oak Ridge, TN, 2007.

2225 [Hartmann, D. L., and Short, D. A.: On the Use of Earth Radiation Budget Statistics for Studies of  
2226 Clouds and Climate, J Atmos Sci, 37, 1233-1250, \[https://doi.org/10.1175/1520-0469\\(1980\\)037<1233:OTUOER>2.0.CO;2\]\(https://doi.org/10.1175/1520-0469\(1980\)037<1233:OTUOER>2.0.CO;2\), 1980.](https://doi.org/10.1175/1520-0469(1980)037<1233:OTUOER>2.0.CO;2)

2228 [Hastie, T., Tibshirani, R., and Friedman, J. H.: The elements of statistical learning : data mining,  
2229 inference, and prediction, 2nd ed., Springer series in statistics, Springer, New York, 2009.](https://doi.org/10.1007/978-1-4939-9736-1)

2231 Hegg, D. A., and P. V. Hobbs (1986), Studies of the mechanisms and rate with which nitrogen  
2232 species are incorporated into cloud water and precipitation, Second Annual Report on Project  
2233 CAPA-21-80 to the Coordinating Research Council.

2236 Hegg, D. A., Covert, D. S., Jonsson, H. H., and Woods, R. K.: The contribution of anthropogenic  
2237 aerosols to aerosol light-scattering and CCN activity in the California coastal zone, Atmos Chem  
2238 Phys, 10, 7341-7351, <https://doi.org/10.5194/acp-10-7341-2010>, 2010.

**Formatted:** Hyperlink, Font: (Default) +Headings CS (Times New Roman), 11 pt

2240 [Herman, G. F., Wu, M. L. C., and Johnson, W. T.: The Effect of Clouds on the Earths Solar and  
2241 Infrared Radiation Budgets, J Atmos Sci, 37, 1251-1261, \[https://doi.org/10.1175/1520-0469\\(1980\\)037<1251:Teocot>2.0.Co;2\]\(https://doi.org/10.1175/1520-0469\(1980\)037<1251:Teocot>2.0.Co;2\), 1980.](https://doi.org/10.1175/1520-0469(1980)037<1251:Teocot>2.0.Co;2)

2244 Hubanks, P. A., King, M. D., Platnick, S., and Pincus, R.: MODIS atmosphere L3 gridded product  
2245 algorithm theoretical basis document, ATBD Reference Number: ATBD-MOD-30, 2019.

2247 Juliano, T. W., Parish, T. R., Rahn, D. A., and Leon, D. C.: An Atmospheric Hydraulic Jump in  
2248 the Santa Barbara Channel, J Appl Meteorol Clim, 56, 2981-2998, ~~10.1175/Jame-D-16-0396-1~~  
2249 <https://doi.org/10.1175/JAMC-D-16-0396.1>, 2017.

2252 Juliano, T. W., Lebo, Z. J., Thompson, G., and Rahn, D. A.: A New Perspective on Coastally  
 2253 Trapped Disturbances Using Data from the Satellite Era, *B Am Meteorol Soc*, 100, 631-651,  
 2254 <https://doi.org/10.1175/Bams-D-18-0002.1>, 2019a.

2255  
 2256 Juliano, T. W., Coggon, M. M., Thompson, G., Rahn, D. A., Seinfeld, J. H., Sorooshian, A., and  
 2257 Lebo, Z. J.: Marine Boundary Layer Clouds Associated with Coastally Trapped Disturbances:  
 2258 Observations and Model Simulations, *J Atmos Sci*, 76, 2963-2993, [https://doi.org/10.1175/Jas-D-](https://doi.org/10.1175/Jas-D-18-0317.1)  
 2259 [18-0317.1](https://doi.org/10.1175/Jas-D-18-0317.1), 2019b.

2260  
 2261 Jung, E., Albrecht, B. A., Jonsson, H. H., Chen, Y. C., Seinfeld, J. H., Sorooshian, A., Metcalf, A.  
 2262 R., Song, S., Fang, M., and Russell, L. M.: Precipitation effects of giant cloud condensation nuclei  
 2263 artificially introduced into stratocumulus clouds, *Atmos Chem Phys*, 15, 5645-5658, <https://doi.org/10.5194/acp-15-5645-2015>, 2015.

2264  
 2265 Klein, S. A.: Synoptic variability of low-cloud properties and meteorological parameters in the  
 2266 subtropical trade wind boundary layer, *J Climate*, 10, 1818-1839, [https://doi.org/10.1175/1520-](https://doi.org/10.1175/1520-0442(1997)10<1818:TSCOLS>2.0.CO;2)  
 2267 [0442](https://doi.org/10.1175/1520-0442(1997)10<1818:TSCOLS>2.0.CO;2), 1997.

2268  
 2269 Klein, S. A., and Hartmann, D. L.: The Seasonal Cycle of Low Stratiform Clouds, *J Climate*, 6,  
 2270 1587-1606, [Doi 10.1175/1520-0442;https://doi.org/10.1175/1520-](https://doi.org/10.1175/1520-0442(1993)06<1587:TSCOLS>2.0.CO;2)  
 2271 [0442\(1993\)006<1587:TSCOLS>2.0.CO;2](https://doi.org/10.1175/1520-0442(1993)06<1587:TSCOLS>2.0.CO;2), 1993.

2272  
 2273 Klein, S. A., Hartmann, D. L., and Norris, J. R.: On the Relationships among Low-Cloud Structure,  
 2274 Sea-Surface Temperature, and Atmospheric Circulation in the Summertime Northeast Pacific, *J*  
 2275 *Climate*, 8, 1140-1155, [Doi 10.1175/1520-0442;https://doi.org/10.1175/1520-](https://doi.org/10.1175/1520-0442(1995)08<1140:OTRALC>2.0.CO;2)  
 2276 [0442\(1995\)008<1140:OTRALC>2.0.CO;2](https://doi.org/10.1175/1520-0442(1995)08<1140:OTRALC>2.0.CO;2), 1995.

2277  
 2278 Kloesel, K. A.: Marine Stratocumulus Cloud Clearing Episodes Observed during Fire, *Mon*  
 2279 *Weather Rev*, 120, 565-578, [Doi 10.1175/1520-0493;https://doi.org/10.1175/1520-](https://doi.org/10.1175/1520-0493(1992)120<0565:MSCCEO>2.0.CO;2)  
 2280 [0493\(1992\)120<0565:MSCCEO>2.0.CO;2](https://doi.org/10.1175/1520-0493(1992)120<0565:MSCCEO>2.0.CO;2), 1992.

2281  
 2282 Lacis, A. A., and Hansen, J. E.: Parameterization for Absorption of Solar-Radiation in Earths  
 2283 Atmosphere, *J Atmos Sci*, 31, 118-133, [Doi 10.1175/1520-0469;https://doi.org/10.1175/1520-](https://doi.org/10.1175/1520-0469(1974)031<0118:APFTAO>2.0.CO;2)  
 2284 [0469\(1974\)031<0118:APFTAO>2.0.CO;2](https://doi.org/10.1175/1520-0469(1974)031<0118:APFTAO>2.0.CO;2), 1974.

2285  
 2286 [Lima, D. C. A., Soares, P. M. M., Semedo, A., & Cardoso, R. M.: A global view of coastal low-](https://doi.org/10.1175/JCLI-D-17-0395.1)  
 2287 [level wind jets using an ensemble of reanalyses. \*Journal of Climate\*, 31\(4\), 1525–1546.](https://doi.org/10.1175/JCLI-D-17-0395.1)  
 2288 <https://doi.org/10.1175/JCLI-D-17-0395.1>, 2018.

2289  
 2290 Lu, M. L., Sorooshian, A., Jonsson, H. H., Feingold, G., Flagan, R. C., and Seinfeld, J. H.: Marine  
 2291 stratocumulus aerosol-cloud relationships in the MASE-II experiment: Precipitation susceptibility  
 2292 in eastern Pacific marine stratocumulus, *J Geophys Res-Atmos*, 114, Artn D24203,  
 2293 <https://doi.org/10.1029/2009jd012774>, 2009.

2294  
 2295 MacDonal, A. B., Dadashazar, H., Chuang, P. Y., Crosbie, E., Wang, H. L., Wang, Z., Jonsson,  
 2296 H. H., Flagan, R. C., Seinfeld, J. H., and Sorooshian, A.: Characteristic Vertical Profiles of Cloud  
 2297

Formatted: Hyperlink, Font: (Default) +Headings CS (Times New Roman), 11 pt

Formatted: Hyperlink, Font: (Default) +Headings CS (Times New Roman), 11 pt

Formatted: Hyperlink, Font: (Default) +Headings CS (Times New Roman), 11 pt

Formatted: Hyperlink, Font: (Default) +Headings CS (Times New Roman), 11 pt

Formatted: Left

Formatted: Hyperlink, Font: (Default) +Headings CS (Times New Roman), 11 pt

2298 Water Composition in Marine Stratocumulus Clouds and Relationships With Precipitation, J  
2299 Geophys Res-Atmos, 123, 3704-3723, <https://doi.org/10.1002/2017JD027900>, 2018.

Formatted: Hyperlink, Font: (Default) +Headings CS (Times New Roman), 11 pt

2300  
2301 Mardi, A. H., Dadashazar, H., MacDonald, A. B., Braun, R. A., Crosbie, E., Xian, P., Thorsen,  
2302 T. J., Coggon, M. M., Fenn, M. A., Ferrare, R. A., Hair, J. W., Woods, R. K., Jonsson, H. H.,  
2303 Flagan, R. C., Seinfeld, J. H., and Sorooshian, A.: Biomass Burning Plumes in the Vicinity of the  
2304 California Coast: Airborne Characterization of Physicochemical Properties, Heating Rates, and  
2305 Spatiotemporal Features, J Geophys Res-Atmos, 123, 13560-13582,  
2306 <https://doi.org/10.1029/2018JD029134>, 2018.

Formatted: Left

Formatted: Hyperlink, Font: (Default) +Headings CS (Times New Roman), 11 pt

2307  
2308 [Mardi, A. H., Dadashazar, H., MacDonald, A. B., Crosbie, E., Coggon, M. M., Aghdam, M. A.,  
2309 Woods, R. K., Jonsson, H. H., Flagan, R. C., Seinfeld, J. H., and Sorooshian, A.: Effects of  
2310 Biomass Burning on Stratocumulus Droplet Characteristics, Drizzle Rate, and Composition, J  
2311 Geophys Res-Atmos, 124, 12301-12318, 10.1029/2019jd031159, 2019.](https://doi.org/10.1029/2019jd031159)

Formatted: Font: (Default) Segoe UI, 9 pt

2312  
2313 Martin, G. M., Johnson, D. W., and Spice, A.: The Measurement and Parameterization of Effective  
2314 Radius of Droplets in Warm Stratocumulus Clouds, J Atmos Sci, 51, 1823-1842, ~~Doi~~  
2315 [10.1175/1520-0469\(1994\)051<1823:TMAPOE>2.0.CO;2](https://doi.org/10.1175/1520-0469(1994)051<1823:TMAPOE>2.0.CO;2),  
2316 1994.

Formatted: Add space between paragraphs of the same style

2317  
2318 Maudlin, L. C., Wang, Z., Jonsson, H. H., and Sorooshian, A.: Impact of wildfires on size-resolved  
2319 aerosol composition at a coastal California site, Atmos Environ, 119, 59-68,  
2320 <https://doi.org/10.1016/j.atmosenv.2015.08.039>, 2015.

Formatted: Hyperlink, Font: (Default) +Headings CS (Times New Roman), 11 pt

2321  
2322 Myers, T. A., and Norris, J. R.: Observational Evidence That Enhanced Subsidence Reduces  
2323 Subtropical Marine Boundary Layer Cloudiness, J Climate, 26, 7507-7524,  
2324 <https://doi.org/10.1175/Jcli-D-12-00736.1>, 2013.

Formatted: Hyperlink, Font: (Default) +Headings CS (Times New Roman), 11 pt

2325  
2326 ~~Meeoy~~McCoy, D. T., Bender, F. A. M., Mohrmann, J. K. C., Hartmann, D. L., Wood, R., and  
2327 Grosvenor, D. P.: The global aerosol-cloud first indirect effect estimated using MODIS, MERRA,  
2328 and AeroCom, J Geophys Res-Atmos, 122, 1779-1796, <https://doi.org/10.1002/2016JD026141>,  
2329 2017.

Formatted: Hyperlink, Font: (Default) +Headings CS (Times New Roman), 11 pt

2330  
2331 Menzel, W. P., and Purdom, J. F. W.: Introducing GOES-1: The first of a new generation of  
2332 geostationary operational environmental satellites, *Bull. Amer. Meteor. Soc.*, 75, 757-781,  
2333 ~~1994~~.[https://doi.org/10.1175/1520-0477\(1994\)075<0757:IGITFO>2.0.CO;2](https://doi.org/10.1175/1520-0477(1994)075<0757:IGITFO>2.0.CO;2), 1994.

Formatted: Left

2334  
2335 Modini, R. L., Frossard, A. A., Ahlm, L., Russell, L. M., Corrigan, C. E., Roberts, G. C.,  
2336 Hawkins, L. N., Schroder, J. C., Bertram, A. K., Zhao, R., Lee, A. K. Y., Abbatt, J. P. D., Lin, J.,  
2337 Nenes, A., Wang, Z., Wonaschutz, A., Sorooshian, A., Noone, K. J., Jonsson, H., Seinfeld, J. H.,  
2338 Toom-Sauntry, D., Macdonald, A. M., and Leaitch, W. R.: Primary marine aerosol-cloud  
2339 interactions off the coast of California, J Geophys Res-Atmos, 120, 4282-4303,  
2340 <https://doi.org/10.1002/2014JD022963>, 2015.

Formatted: Hyperlink, Font: (Default) +Headings CS (Times New Roman), 11 pt

2341  
2342



2343 [Munoz, R. C., and R. D. Garreaud: Dynamics of the low-level jet off the west coast of](#)  
 2344 [subtropical South America, Mon Wea. Rev, 133, 3661–3677,](#)  
 2345 <https://doi.org/10.1175/MWR3074.1>, 2005.

2346  
 2347 [Neiburger, M., Johnson, D. S., and Chien, C. W.: Part 1: The Inversion over the Eastern North](#)  
 2348 [Pacific Ocean. Studies of the Structure of the Atmosphere over the Eastern Pacific Ocean in](#)  
 2349 [Summer, Univ. of California Publications in Meteor., No. 1, University of California Press, 1–](#)  
 2350 [94, 1961.](#)

2351  
 2352 ~~[Norris, J. R., and Leovy, C. B.: Interannual Variability in Stratiform Cloudiness and Sea Surface](#)~~  
 2353 ~~[Temperature, J Climate, 7, 1915–1925, Doi-10.1175/1520-0442, 1994.](#)~~

2354  
 2355 Nicholls, S., and Leighton, J.: An observational study of the structure of stratiform cloud sheets:  
 2356 Part I. Structure. Quart. J. Roy. Meteor. Soc., 112, 431–460,  
 2357 ~~[1986-https://doi.org/10.1002/qj.49711247209, 1986,](#)~~

2358 ~~[Norris, J. R., and Leovy, C. B.: Interannual Variability in Stratiform Cloudiness and Sea-Surface](#)~~  
 2359 ~~[Temperature, J Climate, 7, 1915–1925, https://doi.org/10.1175/1520-0442, 1994.](#)~~

2360  
 2361 Otsu, N., "A Threshold Selection Method from Gray-Level Histograms", IEEE Transactions on  
 2362 Systems, Man, and Cybernetics. Vol. 9, No. 1, pp. 62–66, 1979.

2363  
 2364 Painemal, D., and Zuidema, P.: Microphysical variability in southeast Pacific Stratocumulus  
 2365 clouds: synoptic conditions and radiative response, Atmos Chem Phys, 10, 6255–6269,  
 2366 <https://doi.org/10.5194/acp-10-6255-2010>, 2010.

2367  
 2368 Painemal, D., and Minnis, P.: On the dependence of albedo on cloud microphysics over marine  
 2369 stratocumulus clouds regimes determined from Clouds and the Earth's Radiant Energy System  
 2370 (CERES) data (vol 117, D06203, 2012), J Geophys Res-Atmos, 117, Artn D09299,  
 2371 <https://doi.org/10.1029/2012jd017902>, 2012.

2372  
 2373 [Parish, T. R.: Forcing of the summertime low-level jet along the California coast, J Appl](#)  
 2374 [Meteorol, 39, 2421–2433, https://doi.org/10.1175/1520-](#)  
 2375 [0450\(2000\)039<2421:FOTSLL>2.0.CO;2, 2000.](#)

2376  
 2377 [Parish, T. R., Rahn, D. A., and Leon, D. C.: Aircraft Measurements and Numerical Simulations](#)  
 2378 [of an Expansion Fan off the California Coast, J Appl Meteorol Clim, 55, 2053–2062,](#)  
 2379 <https://doi.org/10.1175/JAMC-D-16-0101.1>, 2016.

2380  
 2381 Pedregosa, F., Varoquaux, G., Gramfort, A., Michel, V., Thirion, B., Grisel, O., Blondel, M.,  
 2382 Prettenhofer, P., Weiss, R., Dubourg, V., Vanderplas, J., Passos, A., Cournapeau, D., Brucher, M.,  
 2383 Perrot, M., and Duchesnay, E.: Scikit-learn: Machine Learning in Python, J Mach Learn Res, 12,  
 2384 2825–2830, 2011.

2385  
 2386 Platnick, S., King, M. D., Ackerman, S. A., Menzel, W. P., Baum, B. A., Riedi, J. C., and Frey, R.  
 2387 A.: The MODIS cloud products: Algorithms and examples from Terra, Ieee T Geosci Remote, 41,  
 2388 459–473, <https://doi.org/10.1109/Tgrs.2002.808301>, 2003.

**Formatted:** Left, Space After: 8 pt, Add space between paragraphs of the same style, Line spacing: Multiple 1.08 li, Adjust space between Latin and Asian text, Adjust space between Asian text and numbers

**Formatted:** Font: (Default) +Headings CS (Times New Roman), Underline, Font color: Hyperlink

**Formatted:** Space After: 0 pt

**Formatted:** Hyperlink, Font: (Default) +Headings CS (Times New Roman), 11 pt

**Formatted:** Hyperlink, Font: (Default) +Headings CS (Times New Roman), 11 pt

**Formatted:** Hyperlink, Font: (Default) +Headings CS (Times New Roman), 11 pt

2389  
 2390 Platnick, S., Meyer, K. G., King, M. D., Wind, G., Amarasinghe, N., Marchant, B., Arnold, G. T.,  
 2391 Zhang, Z. B., Hubanks, P. A., Holz, R. E., Yang, P., Ridgway, W. L., and Riedi, J.: The MODIS  
 2392 Cloud Optical and Microphysical Products: Collection 6 Updates and Examples From Terra and  
 2393 Aqua, *Ieee T Geosci Remote*, 55, 502-525, <https://doi.org/10.1109/Tgrs.2016.2610522>, 2017.

2394  
 2395 Prabhakar, G., Ervens, B., Wang, Z., Maudlin, L. C., Coggon, M. M., Jonsson, H. H., Seinfeld, J.  
 2396 H., and Sorooshian, A.: Sources of nitrate in stratocumulus cloud water: Airborne measurements  
 2397 during the 2011 E-PEACE and 2013 NiCE studies, *Atmos Environ*, 97, 166-173,  
 2398 <https://doi.org/10.1016/j.atmosenv.2014.08.019>, 2014.

2399  
 2400 [Rahn, D. A., and Garreaud, R.: Marine boundary layer over the subtropical southeast Pacific](https://doi.org/10.5194/acp-10-4507-2010)  
 2401 [during VOCALS-REx - Part 2: Synoptic variability, \*Atmos Chem Phys\*, 10, 4507-4519,](https://doi.org/10.5194/acp-10-4507-2010)  
 2402 <https://doi.org/10.5194/acp-10-4507-2010>, 2010.

2403  
 2404 [Rahn, D. A., Parish, T. R., and Leon, D.: Observations of Large Wind Shear above the Marine](https://doi.org/10.1175/Jas-D-15-0363.1)  
 2405 [Boundary Layer near Point Buchon, California, \*J Atmos Sci\*, 73, 3059-3077,](https://doi.org/10.1175/Jas-D-15-0363.1)  
 2406 <https://doi.org/10.1175/Jas-D-15-0363.1>, 2016.

2407  
 2408 [Randall, D. A.: Stratocumulus Cloud Deepening through Entrainment, \*Tellus A\*, 36, 446-457,](https://doi.org/10.3402/tellusa.v36i5.11646)  
 2409 <https://doi.org/10.3402/tellusa.v36i5.11646>, 1984.

2410  
 2411 [Ranjha, R., G. Svensson, M. Tjernström, and A. Semedo: Global distribution and seasonal](https://doi.org/10.3402/tellusa.v65i0.20412)  
 2412 [variability of coastal low level jets derived from ERA-Interim reanalysis. \*Tellus\*, 65A, 20412,](https://doi.org/10.3402/tellusa.v65i0.20412)  
 2413 <https://doi.org/10.3402/tellusa.v65i0.20412>, 2013.

2414  
 2415 Russell, L. M., Sorooshian, A., Seinfeld, J. H., Albrecht, B. A., Nenes, A., Ahlm, L., Chen, Y. C.,  
 2416 Coggon, M., Craven, J. S., Flagan, R. C., Frossard, A. A., Jonsson, H., Jung, E., Lin, J. J., Metcalf,  
 2417 A. R., Modini, R., Mulmenstadt, J., Roberts, G. C., Shingler, T., Song, S., Wang, Z., and  
 2418 Wonaschutz, A.: Eastern Pacific Emitted Aerosol Cloud Experiment, *B Am Meteorol Soc*, 94,  
 2419 709-+, <https://doi.org/10.1175/Bams-D-12-00015.1>, 2013.

2420  
 2421 Sanchez, K. J., Russell, L. M., Modini, R. L., Frossard, A. A., Ahlm, L., Corrigan, C. E.,  
 2422 Roberts, G. C., Hawkins, L. N., Schroder, J. C., Bertram, A. K., Zhao, R., Lee, A. K. Y., Lin, J.  
 2423 J., Nenes, A., Wang, Z., Wonaschutz, A., Sorooshian, A., Noone, K. J., Jonsson, H., Toom, D.,  
 2424 Macdonald, A. M., Leaitch, W. R., and Seinfeld, J. H.: Meteorological and aerosol effects on  
 2425 marine cloud microphysical properties, *J Geophys Res-Atmos*, 121, 4142-4161,  
 2426 <https://doi.org/10.1002/2015JD024595>, 2016.

2427  
 2428 Sorooshian, A., Wang, Z., Coggon, M. M., Jonsson, H. H., and Ervens, B.: Observations of Sharp  
 2429 Oxalate Reductions in Stratocumulus Clouds at Variable Altitudes: Organic Acid and Metal  
 2430 Measurements During the 2011 E-PEACE Campaign, *Environ Sci Technol*, 47, 7747-7756,  
 2431 <https://doi.org/10.1021/es4012383>, 2013a.

2432

**Formatted:** Hyperlink, Font: (Default) +Headings CS (Times New Roman), 11 pt

**Formatted:** Hyperlink, Font: (Default) +Headings CS (Times New Roman), 11 pt

**Formatted:** Hyperlink, Font: (Default) +Headings CS (Times New Roman), 11 pt

**Formatted:** Space After: 0 pt, Add space between paragraphs of the same style

**Formatted:** Left

**Formatted:** Hyperlink, Font: (Default) +Headings CS (Times New Roman), 11 pt

**Formatted:** Hyperlink, Font: (Default) +Headings CS (Times New Roman), 11 pt



2433 Sorooshian, A., Wang, Z., Feingold, G., and L'Ecuyer, T. S.: A satellite perspective on cloud water  
2434 to rain water conversion rates and relationships with environmental conditions, *J Geophys Res-*  
2435 *Atmos*, 118, 6643-6650, <https://doi.org/10.1002/jgrd.50523>, 2013b.

**Formatted:** Hyperlink, Font: (Default) +Headings CS  
(Times New Roman), 11 pt

2437 Sorooshian, A., MacDonald, A. B., Dadashazar, H., Bates, K. H., Coggon, M. M., Craven, J. S.,  
2438 Crosbie, E., Hersey, S. P., Hodas, N., Lin, J. J., Marty, A. N., Maudlin, L. C., Metcalf, A. R.,  
2439 Murphy, S. M., Padro, L. T., Prabhakar, G., Rissman, T. A., Shingler, T., Varutbangkul, V., Wang,  
2440 Z., Woods, R. K., Chuang, P. Y., Nenes, A., Jonsson, H. H., Flagan, R. C., and Seinfeld, J. H.: A  
2441 multi-year data set on aerosol-cloud-precipitation-meteorology interactions for marine  
2442 stratocumulus clouds, *Figshare*,  
2443 <https://doi.org/10.6084/m9.figshare.5099983.v3>, 2017.

**Formatted:** Hyperlink, Font: (Default) +Headings CS  
(Times New Roman), 11 pt

2445 Sorooshian, A., MacDonald, A. B., Dadashazar, H., Bates, K. H., Coggon, M. M., Craven, J. S.,  
2446 Crosbie, E., Hersey, S. P., Hodas, N., Lin, J. J., Marty, A. N., Maudlin, L. C., Metcalf, A. R.,  
2447 Murphy, S. M., Padro, L. T., Prabhakar, G., Rissman, T. A., Shingler, T., Varutbangkul, V., Wang,  
2448 Z., Woods, R. K., Chuang, P. Y., Nenes, A., Jonsson, H. H., Flagan, R. C., and Seinfeld, J. H.: A  
2449 multi-year data set on aerosol-cloud-precipitation-meteorology interactions for marine  
2450 stratocumulus clouds, *Sci Data*, 5, Artn 180026, <https://doi.org/10.1038/Sdata.2018.26>, 2018.

**Formatted:** Hyperlink, Font: (Default) +Headings CS  
(Times New Roman), 11 pt

2452 Sorooshian, A., Anderson, B., Bauer, S. E., Braun, R. A., Cairns, B., Crosbie, E., Dadashazar, H.,  
2453 Diskin, G., Ferrare, R., Flagan, R. C., Hair, J., Hostetler, C., Jonsson, H. H., Kleb, M. M., Liu, H.  
2454 Y., MacDonald, A. B., McComiskey, A., Moore, R., Painemal, D., Russell, L. M., Seinfeld, J. H.,  
2455 Shook, M., Smith, W. L., Thornhill, K., Tselioudis, G., Wang, H. L., Zeng, X. B., Zhang, B.,  
2456 Ziemba, L., and Zuidema, P.: Aerosol-Cloud-Meteorology Interaction Airborne Field  
2457 Investigations: Using Lessons Learned from the US West Coast in the Design of ACTIVATE off  
2458 the US East Coast, *B Am Meteorol Soc*, 100, 1511-1528, [https://doi.org/10.1175/Bams-D-18-](https://doi.org/10.1175/Bams-D-18-0100.1)  
2459 [0100.1](https://doi.org/10.1175/Bams-D-18-0100.1), 2019.

**Formatted:** Hyperlink, Font: (Default) +Headings CS  
(Times New Roman), 11 pt

2461 [Stephens, G. L., and Greenwald, T. J.: The Earths Radiation Budget and Its Relation to](https://doi.org/10.1029/91jd00972)  
2462 [Atmospheric Hydrology .2. Observations of Cloud Effects, \*J Geophys Res-Atmos\*, 96, 15325-  
2463 \[15340, \\*https://doi.org/10.1029/91jd00972\\*. 1991.\]\(https://doi.org/10.1029/91jd00972\)](https://doi.org/10.1029/91jd00972)

2465 Stevens, B., Lenschow, D. H., Vali, G., Gerber, H., Bandy, A., Blomquist, B., Brenguier, J. L.,  
2466 Bretherton, C. S., Burnet, F., Campos, T., Chai, S., Faloona, I., Friesen, D., Haimov, S., Laursen,  
2467 K., Lilly, D. K., Loehrer, S. M., Malinowski, S. P., Morley, B., Petters, M. D., Rogers, D. C.,  
2468 Russell, L., Savic-Jovac, V., Snider, J. R., Straub, D., Szumowski, M. J., Takagi, H., Thornton,  
2469 D. C., Tschudi, M., Twohy, C., Wetzel, M., and van Zanten, M. C.: Dynamics and chemistry of  
2470 marine stratocumulus - Dycoms-II, *B Am Meteorol Soc*, 84, 579-593, [10.1175/Bams-84-5-](https://doi.org/10.1175/BAMS-84-5-579)  
2471 [579, \*https://doi.org/10.1175/BAMS-84-5-579\*](https://doi.org/10.1175/BAMS-84-5-579), 2003.

**Formatted:** Space After: 0 pt, Add space between  
paragraphs of the same style

**Formatted:** Left

2473 Stull, R. B.: *An Introduction to Boundary Layer Meteorology*. Kluwer Academic, 666 pp, 1988.

2475 Tibshirani, R.: Regression shrinkage and selection via the Lasso, *J Roy Stat Soc B Met*, 58(1), 267-  
2476 288, 1996.

2478 Wang, S. P., Albrecht, B. A., and Minnis, P.: A Regional Simulation of Marine Boundary-Layer  
2479 Clouds, *J Atmos Sci*, 50, 4022-4043, ~~Doi-~~<https://doi.org/10.1175/1520-0469>, 1993.  
2480  
2481 Wang, Z., Sorooshian, A., Prabhakar, G., Coggon, M. M., and Jonsson, H. H.: Impact of emissions  
2482 from shipping, land, and the ocean on stratocumulus cloud water elemental composition during  
2483 the 2011 E-PEACE field campaign, *Atmos Environ*, 89, 570-580,  
2484 <https://doi.org/10.1016/j.atmosenv.2014.01.020>, 2014.  
2485  
2486 Wang, Z., Ramirez, M. M., Dadashazar, H., MacDonald, A. B., Crosbie, E., Bates, K. H., Coggon,  
2487 M. M., Craven, J. S., Lynch, P., Campbell, J. R., Aghdam, M. A., Woods, R. K., Jonsson, H.,  
2488 Flagan, R. C., Seinfeld, J. H., and Sorooshian, A.: Contrasting cloud composition between coupled  
2489 and decoupled marine boundary layer clouds, *J Geophys Res-Atmos*, 121, 11679-11691,  
2490 <https://doi.org/10.1002/2016jd025695>, 2016.  
2491  
2492 Warren, S. G., Hahn, C. J., London, J., Chervin, R. M., and Jenne, R. L.: Global distribution of  
2493 total cloud cover and cloud types over land, NCAR Tech. Note NCAR/TN-2731STR, National  
2494 Center for Atmospheric Research, Boulder, CO, 1986.  
2495  
2496 Wood, R.: Drizzle in stratiform boundary layer clouds. *Part II: Microphysical aspects*, *J Atmos*  
2497 *Sci*, 62, 3034-3050, <https://doi.org/10.1175/Jas3530.1.2005a>.  
2498  
2499 *Wood, R.: Drizzle in stratiform boundary layer clouds. Part I: Vertical and horizontal structure*, *J*  
2500 *Atmos Sci*, 62, 3011-3033, ~~Doi-~~<https://doi.org/10.1175/Jas3529.1.20052005b>.  
2501  
2502 *Wood, R.: Cancellation of aerosol indirect effects in marine stratocumulus through cloud*  
2503 *thinning*, *J Atmos Sci*, 64, 2657-2669, <https://doi.org/10.1175/Jas3942.1.2007>.  
2504  
2505 *Wood, R.: Stratocumulus Clouds*, *Mon Weather Rev.* 140, 2373-2423,  
2506 <https://doi.org/10.1175/Mwr-D-11-00121.1.2012>.  
2507  
2508 *Wood, R., and Bretherton, C. S.: Boundary layer depth, entrainment, and decoupling in the*  
2509 *cloud-capped subtropical and tropical marine boundary layer*, *J Climate*, 17, 3576-3588,  
2510 <https://doi.org/10.1175/1520-0442.2004>.  
2511  
2512 Wood, R., and Bretherton, C. S.: On the relationship between stratiform low cloud cover and  
2513 lower-tropospheric stability, *J Climate*, 19, 6425-6432, ~~Doi-~~<https://doi.org/10.1175/Jcli3988.1>,  
2514 2006.  
2515  
2516 Youn, J. S., Crosbie, E., Maudlin, L. C., Wang, Z., and Sorooshian, A.: Dimethylamine as a major  
2517 alkyl amine species in particles and cloud water: Observations in semi-arid and coastal regions,  
2518 *Atmos Environ*, 122, 250-258, <https://doi.org/10.1016/j.atmosenv.2015.09.061>, 2015.  
2519  
2520 Yuter, S. E., Hader, J. D., Miller, M. A., and Mechem, D. B.: Abrupt cloud clearing of marine  
2521 stratocumulus in the subtropical southeast Atlantic, *Science*, 361, 697-+,  
2522 <https://doi.org/10.1126/science.aar5836>, 2018.  
2523

**Formatted:** Hyperlink, Font: (Default) +Headings CS (Times New Roman), 11 pt

**Formatted:** Hyperlink, Font: (Default) +Headings CS (Times New Roman), 11 pt

**Formatted:** Hyperlink, Font: (Default) +Headings CS (Times New Roman), 11 pt

**Formatted:** Hyperlink, Font: (Default) +Headings CS (Times New Roman), 11 pt

**Formatted:** Hyperlink, Font: (Default) +Headings CS (Times New Roman), 11 pt

**Formatted:** Hyperlink, Font: (Default) +Headings CS (Times New Roman), 11 pt

**Formatted:** Hyperlink, Font: (Default) +Headings CS (Times New Roman), 11 pt

**Formatted:** Space After: 0 pt, Line spacing: single, Don't adjust space between Latin and Asian text, Don't adjust space between Asian text and numbers

2524  
2525  
2526 Zemba, J., and Friehe, C. A.: The Marine Atmospheric Boundary-Layer Jet in the Coastal Ocean  
2527 Dynamics Experiment, J Geophys Res-Oceans, 92, 1489-1496,  
2528 <https://doi.org/10.1029/Jc092ic02p01489>, 1987.  
2529  
2530 Zuidema, P., Painemal, D., de Szoeke, S., and Fairall, C.: Stratocumulus Cloud-Top Height  
2531 Estimates and Their Climatic Implications, J Climate, 22, 4652-4666,  
2532 <https://doi.org/10.1175/2009JCLI2708.1>, 2009.

2533 **Table 1.** Summary of reanalysis and satellite data products used in this study. For the rows with multiple products, underlined entries  
 2534 correspond to one in another between different columns.

2535

Input coordinate for data download	Parameter	Source	Product identifier	Spatial resolution	Vertical level	Temporal resolution	Reference
20°-60° N, 110°-160° W	Visible band imagery	GOES-11/15 imager	NA	1 km × 1 km at nadir	NA	30 min	Menzel and Purdom, 1994
20°-60° N, 110°-160° W	Mean sea level pressure	MERRA-2 model	M2I3NPASM	0.5° × 0.625°	NA	3 h	Bosilovich et al., 2016
20°-60° N, 110°-160° W	Air temperature	MERRA-2 model	<u>M2T1NXFLX</u> /M2I3NPASM	0.5° × 0.625°	<u>Sea surface</u> , 950, 850, 700 hPa	<u>1 h</u> /3 h	Bosilovich et al., 2016
20°-60° N, 110°-160° W	Geopotential height	MERRA-2 model	M2I3NPASM	0.5° × 0.625°	850, 500 hPa	3 h	Bosilovich et al., 2016
20°-60° N, 110°-160° W	Wind speed	MERRA-2 model	M2T1NXFLX	0.5° × 0.625°	<u>Surface</u> , 950, 850, 700 hPa	<u>1 h</u> /3 h	Bosilovich et al., 2016
20°-60° N, 110°-160° W	Vertical pressure velocity	MERRA-2 model	M2I3NPASM	0.5° × 0.625°	700 hPa	3 h	Bosilovich et al., 2016
20°-60° N, 110°-160° W	Planetary boundary layer height	MERRA-2 model	M2T1NXFLX	0.5° × 0.625°	NA	1 h	Bosilovich et al., 2016
20°-60° N, 110°-160° W	Sea surface temperature	MERRA-2 model	M2T1NXOCN	0.5° × 0.625°	NA	1 h	Bosilovich et al., 2016
20°-60° N, 110°-160° W	Specific humidity	MERRA-2 model	<u>M2I1NXASM</u> /M2I3NPASM	0.5° × 0.625°	<u>10 m</u> , 950, 850, 700 hPa	<u>1 h</u> /3 h	Bosilovich et al., 2016
20°-60° N, 110°-160° W	Aerosol optical depth AOD	MERRA-2 model	M2I3NXGAS	0.5° × 0.625°	NA	3 h	Bosilovich et al., 2016
30°-50° N, 115°-135° W	Cloud optical thickness liquid	MODIS-Terra/Aqua	MOD08_D3/MYD08_D3	1° × 1°	NA	Daily	Hubanks et al., 2019
30°-50° N, 115°-135° W	Cloud fraction day	MODIS-Terra/Aqua	MOD08_D3/MYD08_D3	1° × 1°	NA	Daily	Hubanks et al., 2019
30°-50° N, 115°-135° W	Cloud water path liquid	MODIS-Terra/Aqua	MOD08_D3/MYD08_D3	1° × 1°	NA	Daily	Hubanks et al., 2019
30°-50° N, 115°-135° W	Cloud effective radius liquid	MODIS-Terra/Aqua	MOD08_D3/MYD08_D3	1° × 1°	NA	Daily	Hubanks et al., 2019

2536

2537

2538 **Table 2.** Absolute changes in the parallel component of horizontal wind speed relative to the cloud  
2539 edge,  $|\Delta v|$  in units of  $\text{m s}^{-1}$ , across various legs using FASE aircraft data. Values were calculated  
2540 based on a 40 km leg distance (approximate length of each leg). Values for the cloud top leg were  
2541 estimated using the sawtooth leg performed across the cloud top boundary. The free troposphere  
2542 level leg was not conducted in RF08 and thus left blank.  
2543

Formatted: Font: Italic

	RF08	RF09A	RF09B
Free troposphere		0.4	1.6
Cloud top	9.6	6.4	4.8
Mid-cloud	7.2	6.8	6.0
Above cloud base	6.8	5.2	5.2
Surface	3.6	2.4	0.0

2544

2545  
2546  
2547  
2548

**Table 3.** Summary of thermodynamic, dynamic, and cloud properties on both sides of the clear-cloudy interface for three FASE case research flights (RFs).  $U$  represents total horizontal wind speed ( $U = \sqrt{u^2 + v^2}$ ) across the depth of the inversion layer.

	Cloudy			Clear		
	RF08	RF09A	RF09B	RF08	RF09A	RF09B
$SST$ (K)	286.6	287.1	287.3	287.0	287.5	287.2
Surface wind ( $m s^{-1}$ )	11.3	11.1	11.6	13.2	12.3	11.5
$u^*$ ( $m s^{-1}$ )	0.15	0.19	0.11	0.40	0.32	0.25
$w^*$ ( $m s^{-1}$ )	0.44	0.64	0.68	0.44	0.53	0.38
$z_{i/LMO}$	9.8	15.7	49.1	0.8	2.2	1.4
Inversion-base height (m)	367	375	391	359	354	386
Inversion-top height (m)	422	441	457	443	440	455
Inversion depth (m)	55	66	66	82	86	69
$\Delta\theta_i$ (K)	7.4	8.6	7.0	7.3	7.6	5.4
$(\Delta\theta_i/\Delta z)_{Max}$ ( $K m^{-1}$ )	0.38	0.41	0.25	0.32	0.33	0.23
$\Delta q_T$ ( $g kg^{-1}$ )	-3	-3.2	-2.6	-2.9	-3.3	-2.6
$\Delta U$ ( $m s^{-1}$ )	0.80	1.35	1.35	5.44	2.50	5.32
Cloud base (m)	242	217	265			
Cloud top (m)	372	408	401			
Cloud depth (m)	131	191	137			
Cloud $LWP$ ( $g m^{-2}$ )	15	32	18			
$R_{cb}$ ( $mm day^{-1}$ )	0.48	0.09	0.07			
$r_e$ ( $\mu m$ )	6.6	6.0	5.9			
$N_d$ ( $cm^{-3}$ )	107	141	148			
Surface PCASP ( $cm^{-3}$ )	108	206	236	106	186	207

Formatted: Font: Italic

Formatted: Font: Italic

Formatted: Font: Italic

Formatted: Font: Italic

Formatted: Font: Italic

Formatted: Font: Italic

Formatted: Font: Italic

Formatted: Font: Italic

Formatted: Font: Italic

Formatted: Font: Italic

Formatted: Font: Italic

Formatted: Font: Italic

Formatted: Font: Italic

2549  
2550

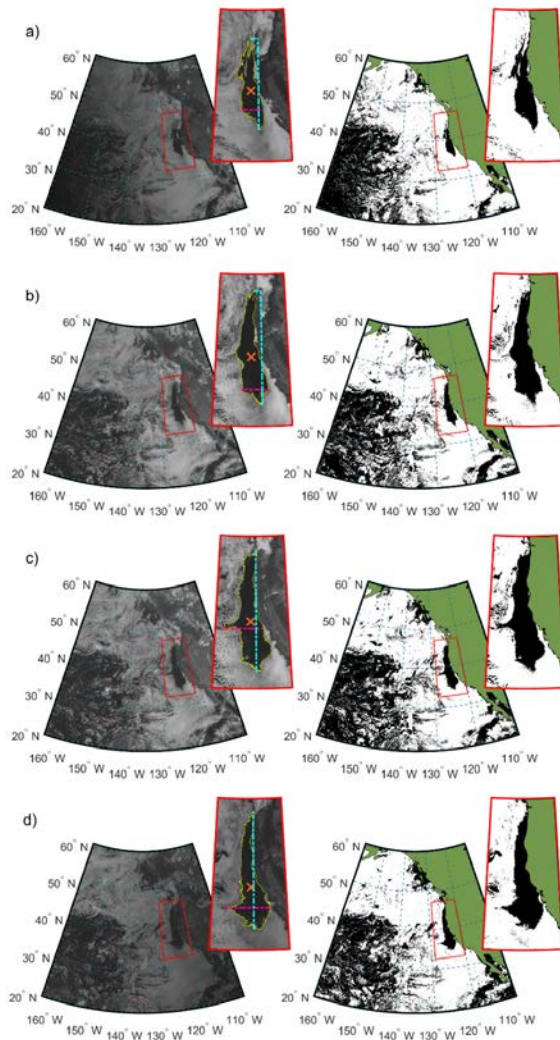


**Figure 1.** Sequence of data processing with GOES imagery at four times during a day: (i) 16:15 UTC 09 August 2011; (ii) 19:15 UTC 09 August 2011; (iii) 20:45 UTC 09 August 2011; and (iv) 01:15 UTC 10 August 2011. Left panels show visible-band images of a clearing event obtained from GOES-11 data, while the right panel is produced using cloud masking. Note that the clearing border, centroid, and lengths ( $x$  and  $y$ ) are overlaid on the GOES images. Local time (PST) requires subtraction of seven hours from UTC time.

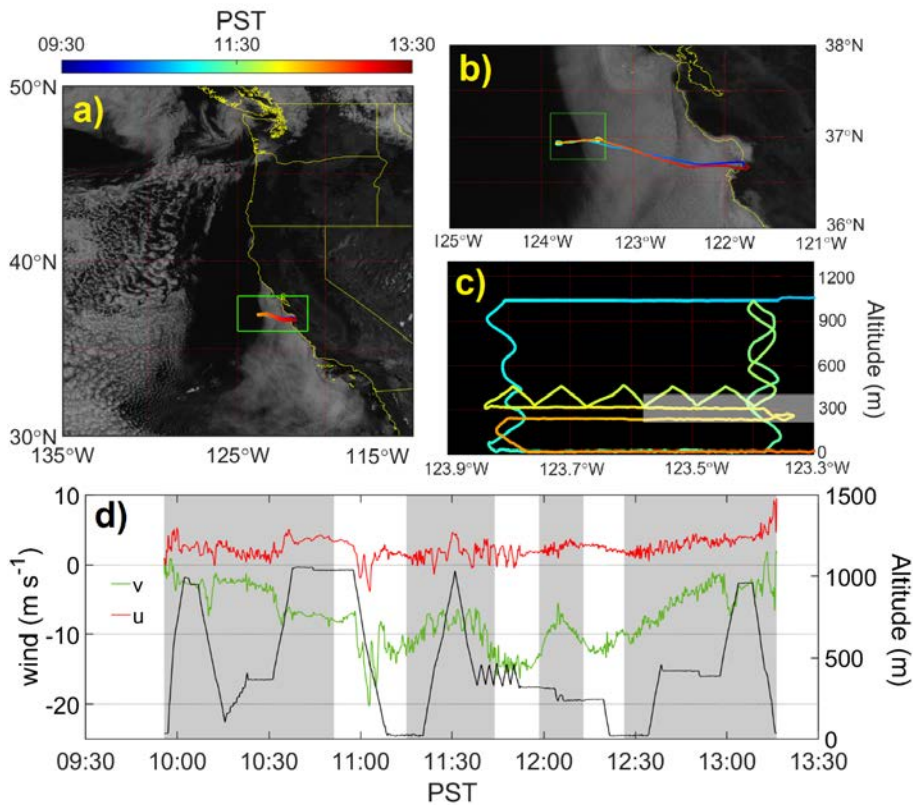


**Figure 2.** a) GOES 15 visible band image (11:45 (18:45) PST (UTC) on 03 Aug 2016) with the overlaid flight path of FASE RF09A. b) Zoomed-in view of the satellite image to highlight the clear-cloudy border. c) Aircraft flight strategy at the cloudy-clear interface for the green box highlighted in b). Cloud borders are denoted by a shaded box. d) Time series of flight altitude and horizontal wind speed, which is decomposed into two components that are perpendicular ( $u$ ) and parallel ( $v$ ) to the cloud edge. Wind speeds were smoothed using low-pass filtering. Parts of the flight that sampled air on the cloudy side of the clear-cloudy border are shaded in grey.

Formatted: Font: Italic

Formatted: Font: Italic



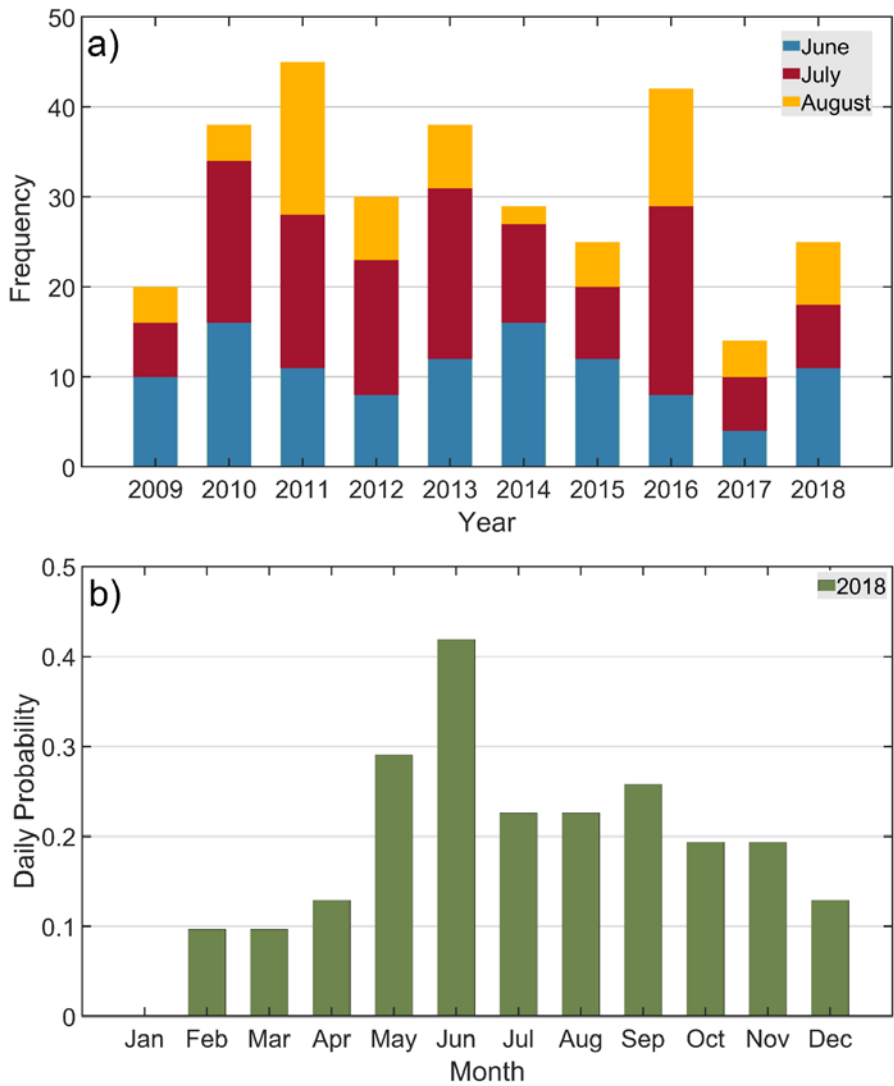


**Figure 3.** a) Frequency of clearing events in the study region for each summer month between 2009 and 2018. b) Daily probability of clearing events (i.e., days with clearings divided by total days in that month) in each month of a representative year, 2018.

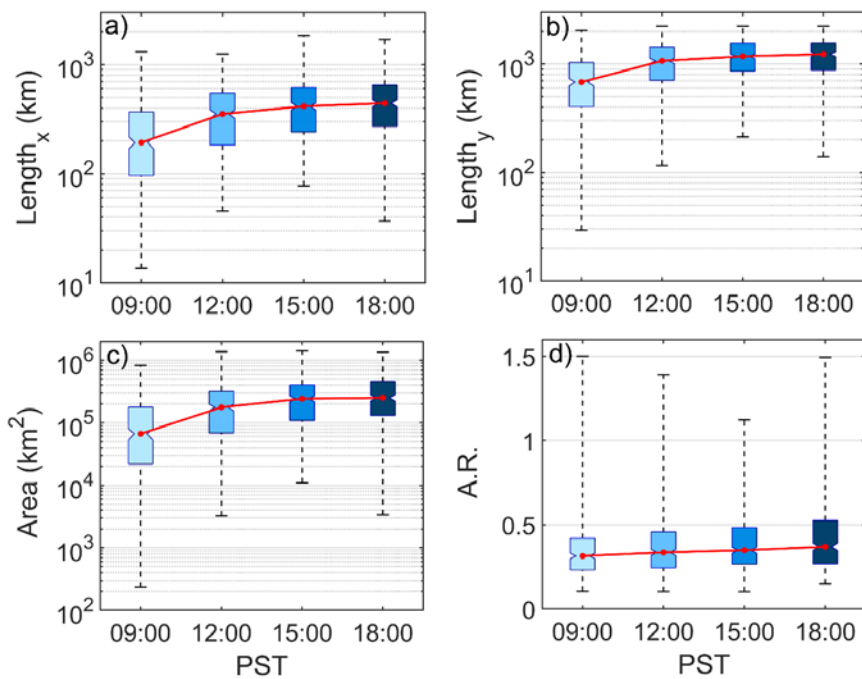


**Figure 4.** Diurnal profiles of (a) widest point of clearings at a fixed latitudinal value, (b) longest dimension between the maximum and minimum latitudinal coordinates of a clearing regardless of longitudinal value, (c) total clearing area, and (d) aspect ratio of clearing (i.e., width divided by length using the maximum values as described by panels a-b). The box and whisker plots show the median values (red points), the 25<sup>th</sup> and 75<sup>th</sup> percentile values (bottom and top of boxes, respectively), and minimum and maximum values (bottom and top whiskers, respectively).

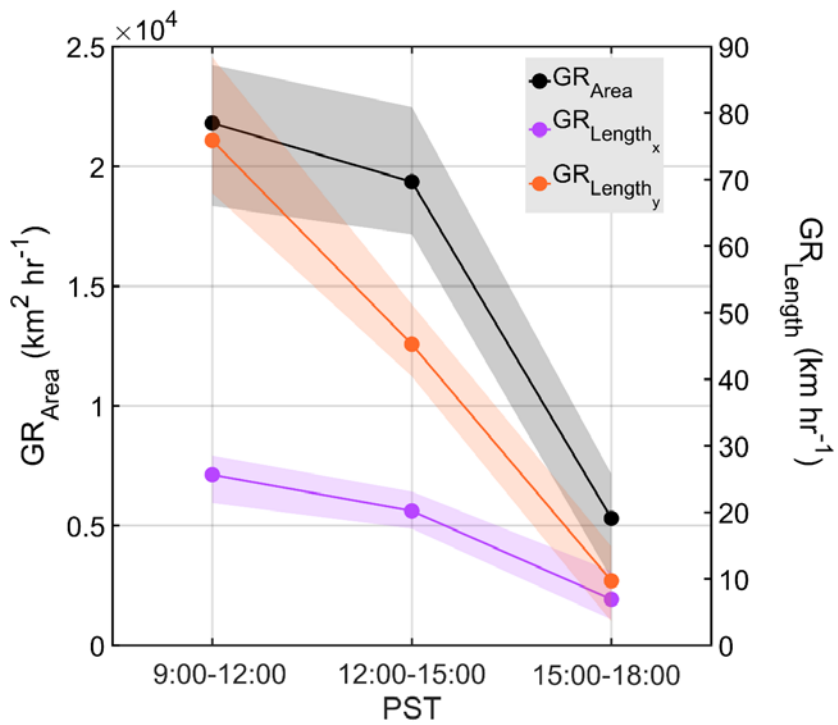


**Figure 5.** The median growth rate of clearing area (left y axis) and width and length of clearings (right y axis) over three hour increments. Shading of curves represents 95% confidence intervals calculated using bootstrapping ( $n=10,000$ ).

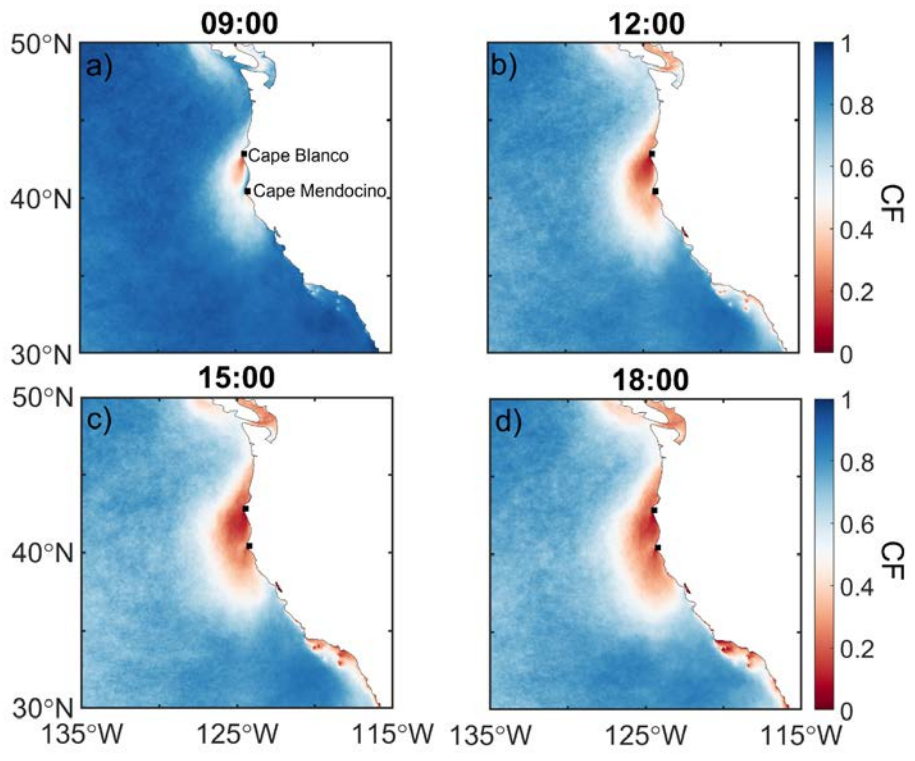
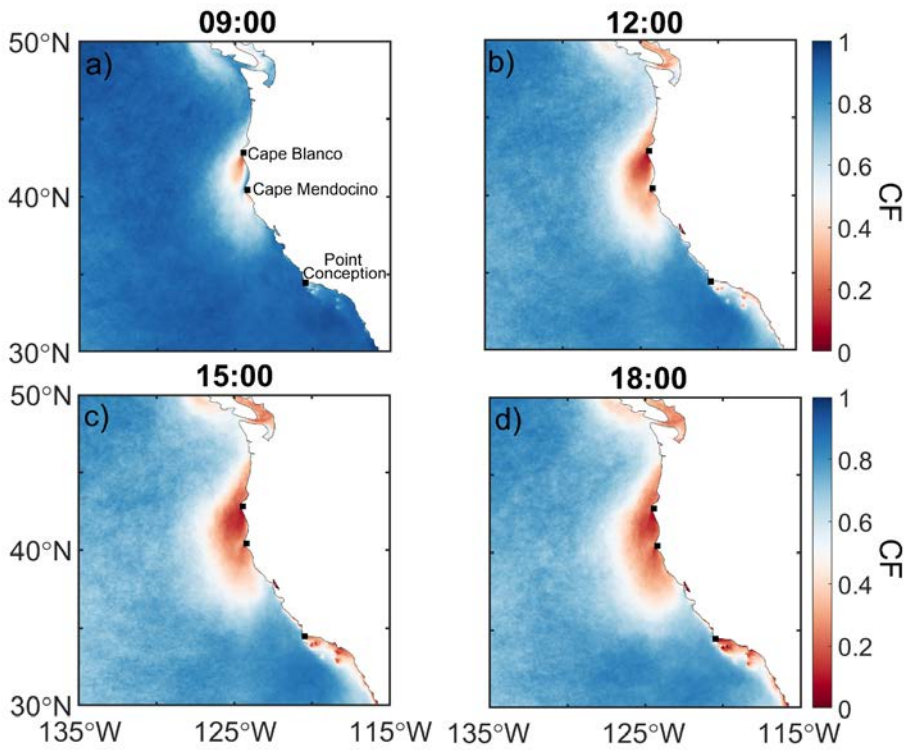
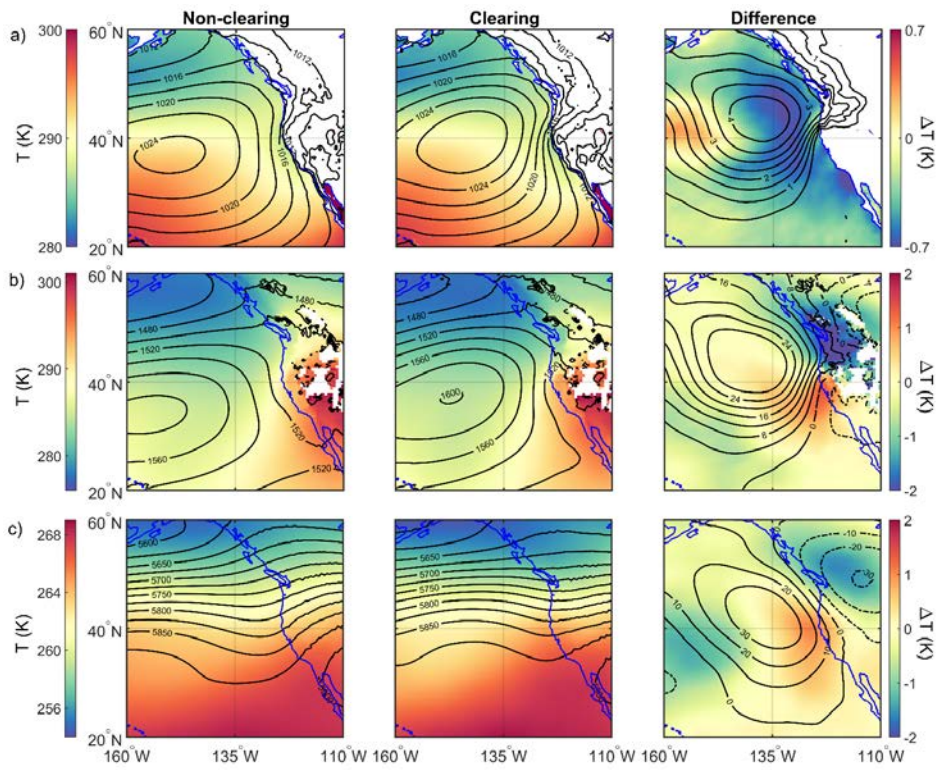


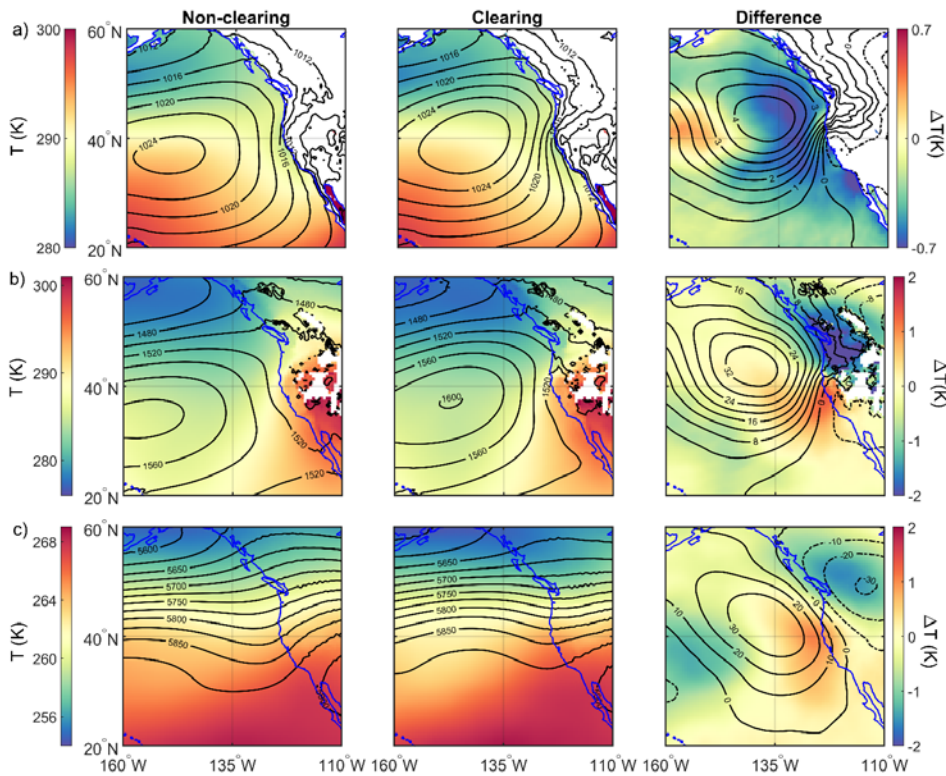
Figure 6.



**Figure 5.** Diurnal profiles (PST times shown; add 7 h for UTC) of cloud fraction (*CF*) in the study region based on GOES imagery data from 306 clearing cases between 2009 and 2018 during JJA months.

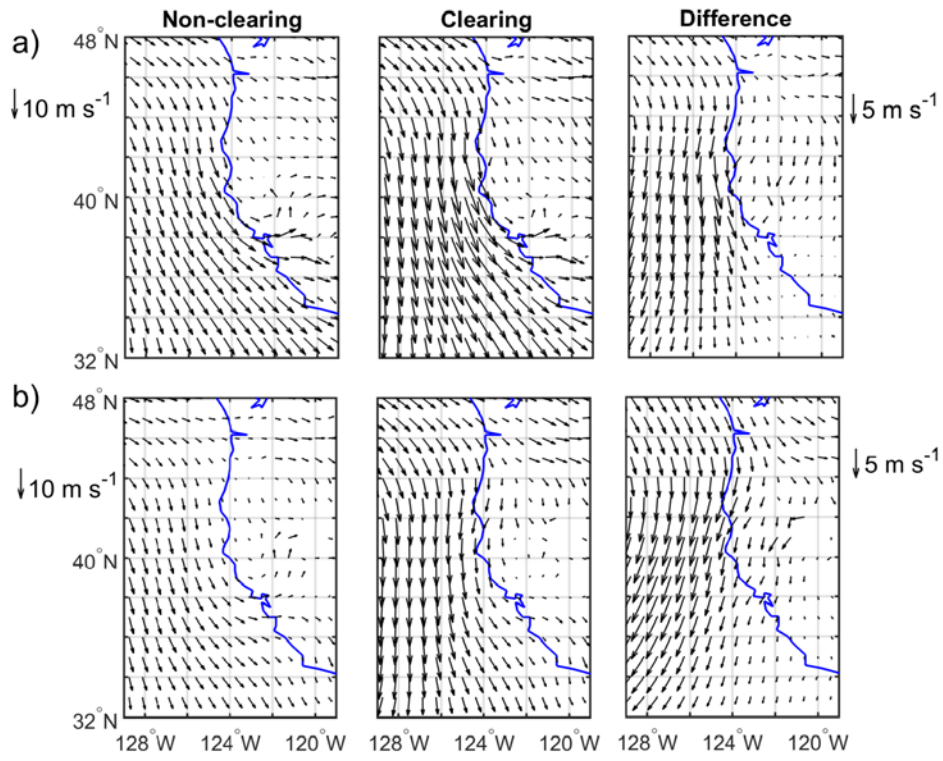
Formatted: Font: Italic

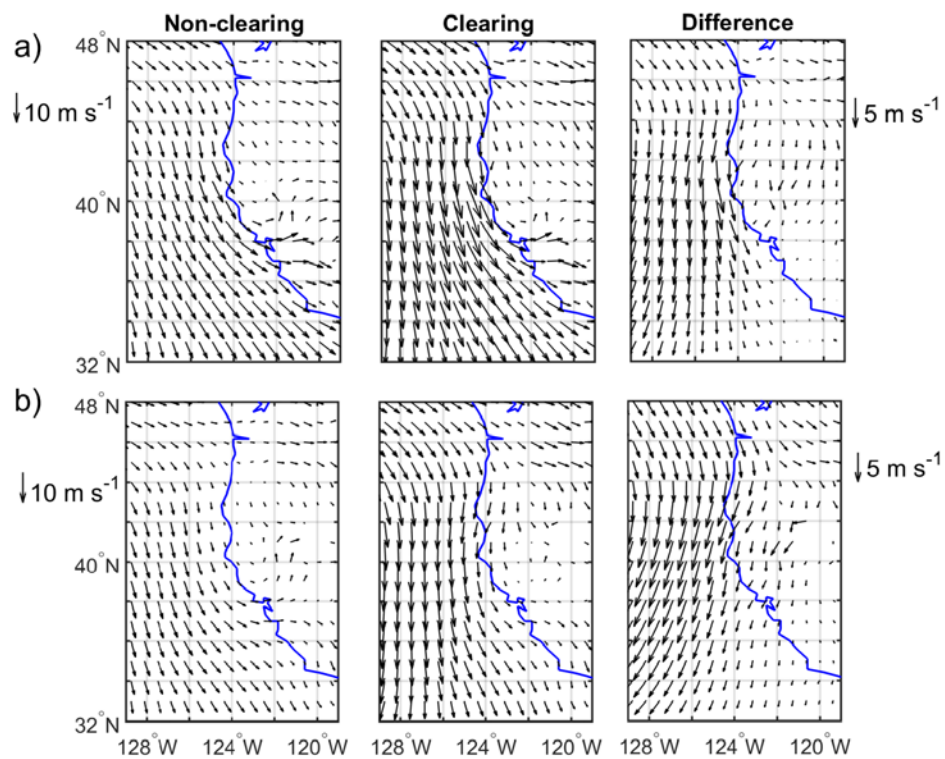




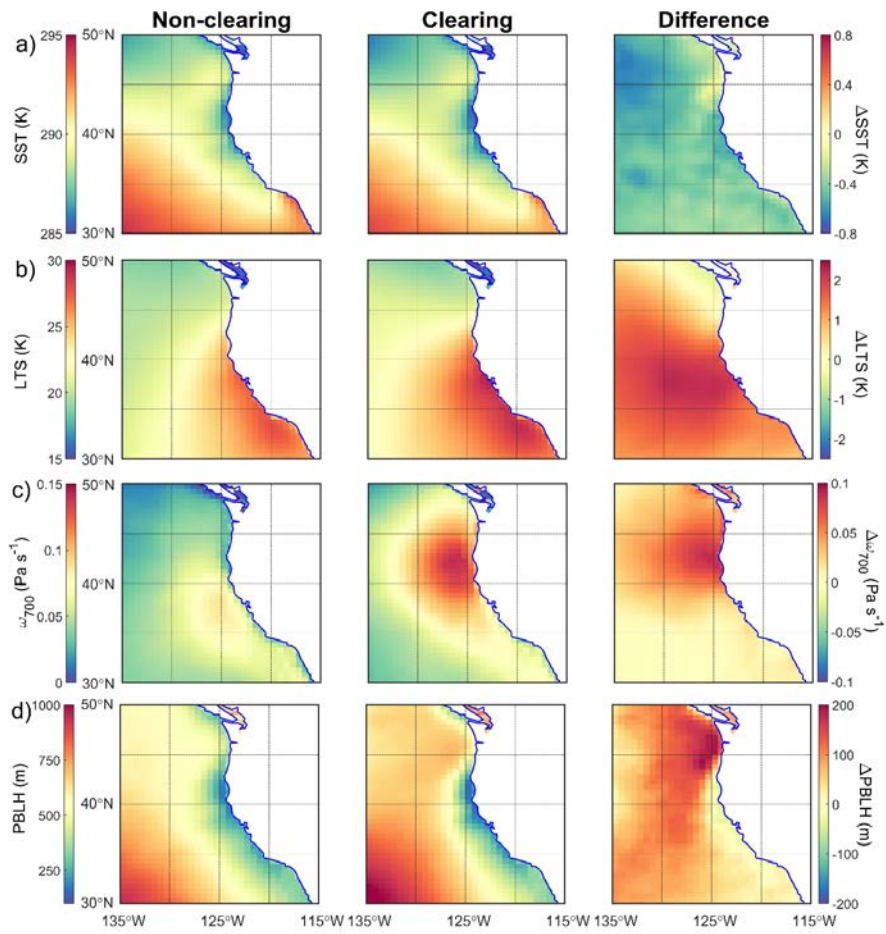
**Figure 76.** Climatology of non-clearing and clearing days as well as their differences (clearing minus non-clearing) during the summers (JJA) between 2009 and 2018 for a) mean sea level pressure (contours in hPa) and air temperature (color map) at sea surface, b) 850 hPa geopotential heights (contours in m) and air temperature (color map), and c) 500 hPa geopotential heights (contours in m) and air temperature (color map). The data were obtained from MERRA-2 reanalysis. Differences (clearing minus non-clearing) are shown in the farthest right column with separate color scales. White areas indicate no data were available.







**Figure 8.** Same as Fig. 76 but for wind speed at the a) surface and b) 850 hPa. Reference wind vectors are shown on the far left for the left two columns, with separately defined vectors on the far right for the difference (clearing minus non-clearing) plots in the farthest right column.



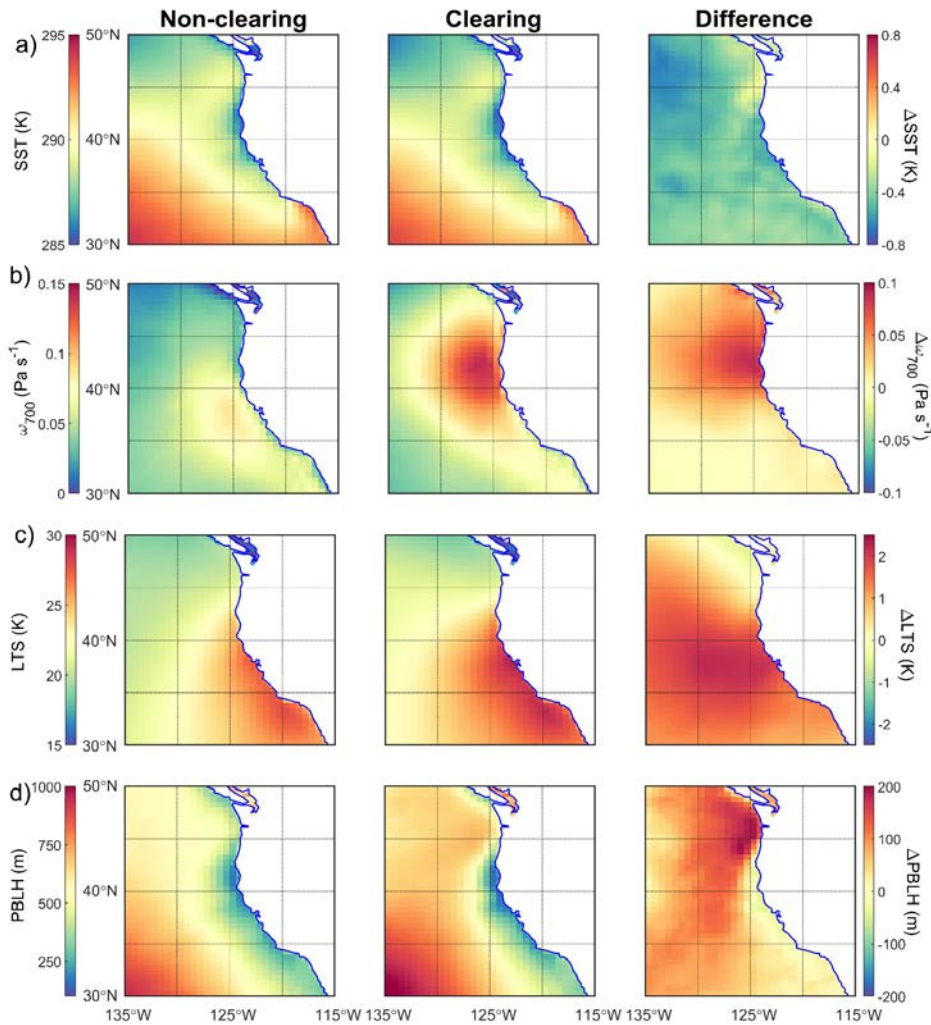


**Figure 8.** Spatial map of environmental parameters controlling properties of stratocumulus clouds for non-clearing and clearing events: a) sea surface temperature (*SST*), b) ~~lower-tropospheric stability (*LTS*)~~, c) ~~lower-tropospheric stability (*LTS*)~~, d) planetary boundary layer height (*PBLH*), e) specific humidity at 10 m (*q*<sub>10m</sub>), f) specific humidity at 850 hPa (*q*<sub>850</sub>), and g) aerosol optical depth (*AOD*). Differences (clearing minus non-clearing) are shown in the farthest right column with separate color scales.

- Formatted: Font: Italic
- Formatted: Font: Italic
- Formatted: Font: Italic
- Formatted: Font: Italic
- Formatted: Font: Italic
- Formatted: Font: Italic

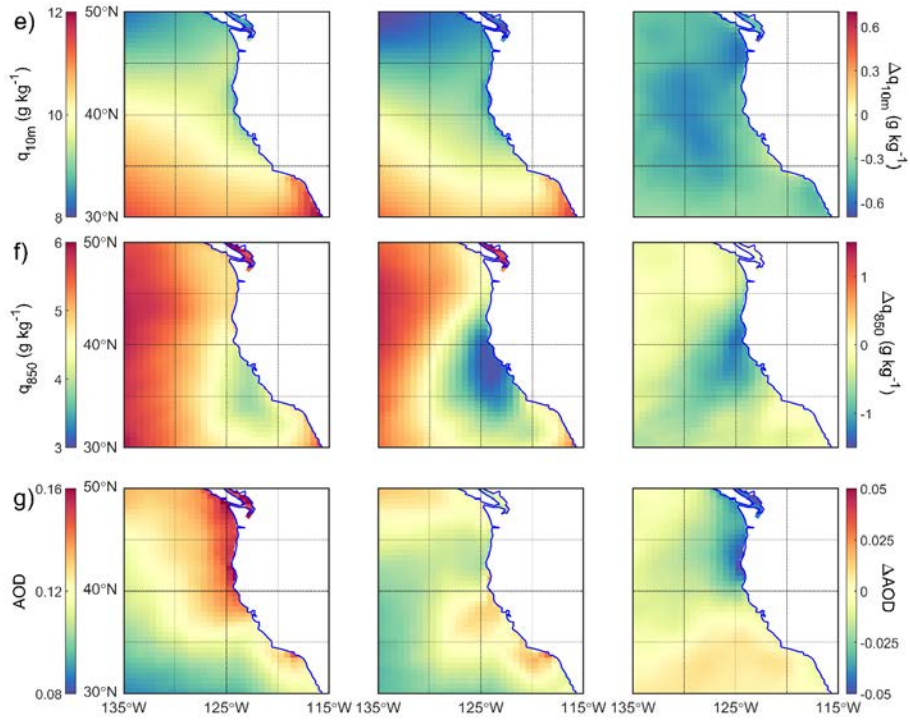
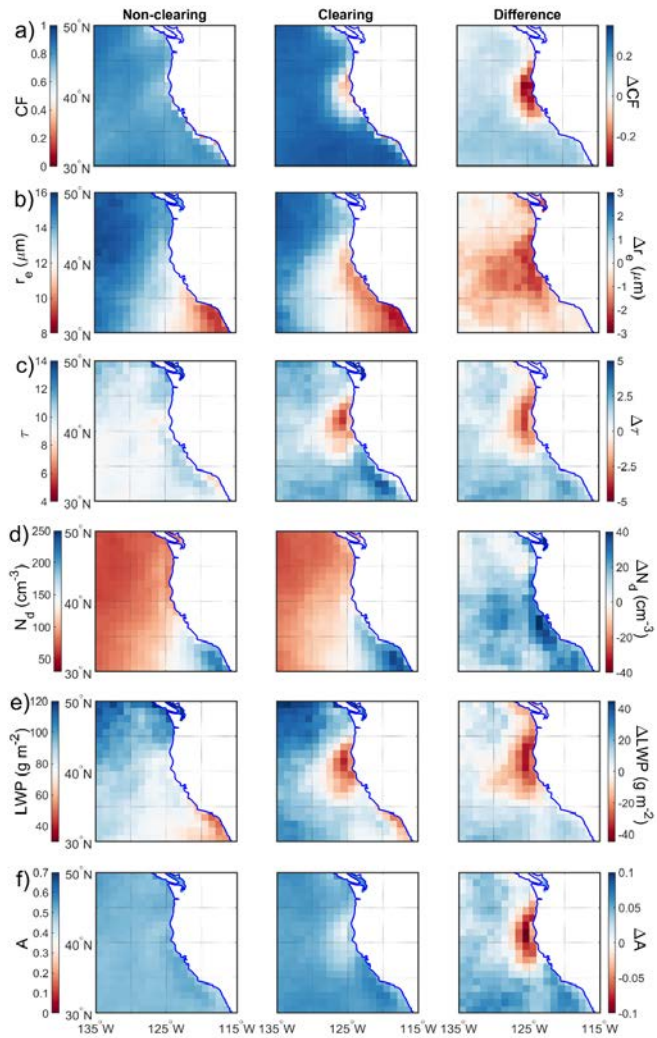
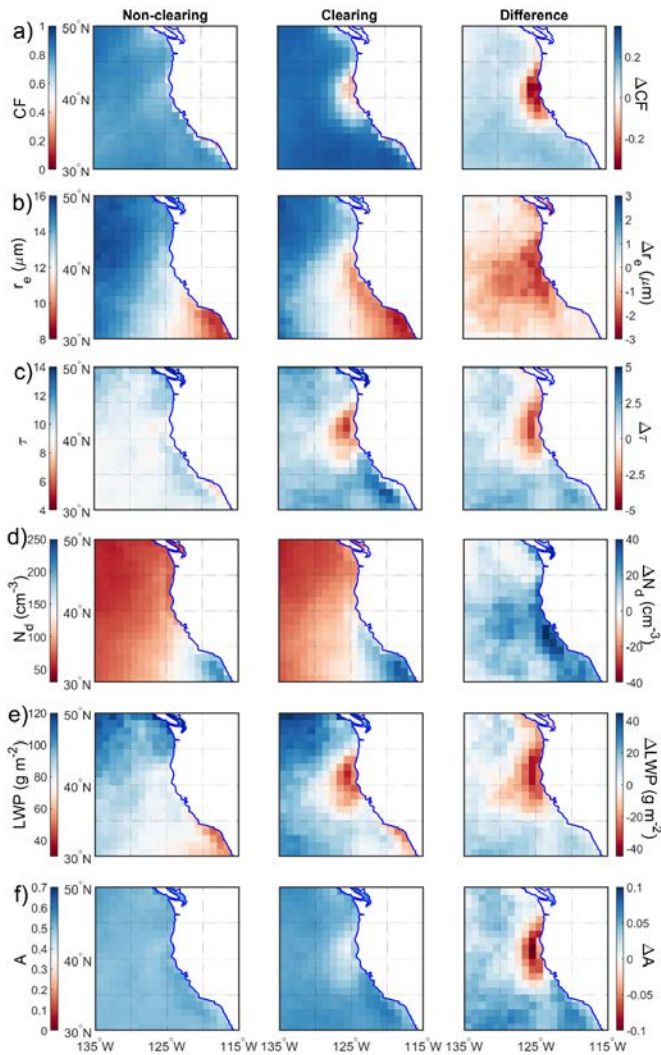


Figure 98 (continued).







**Figure 109.** Average cloud parameters for non-clearing and clearing days obtained from MODIS Terra Level 3 (Collection 6.1) data: a) cloud fraction day ( $CF$ ), b) cloud top droplet effective radius ( $r_e$ ), c) cloud optical thickness ( $\tau$ ), d) cloud droplet number concentration ( $N_d$ ), e) cloud liquid water path ( $LWP$ ), and f) cloud albedo ( $A$ ). Differences (clearing minus non-clearing) are shown in the farthest right column with separate color scales. Values from any instances of clear pixels were omitted from the analysis to produce panels b-f. Fig. [SSS6](#) is an analogous figure based on MODIS Aqua data.

Formatted: Font: Italic

Formatted: Font: Italic

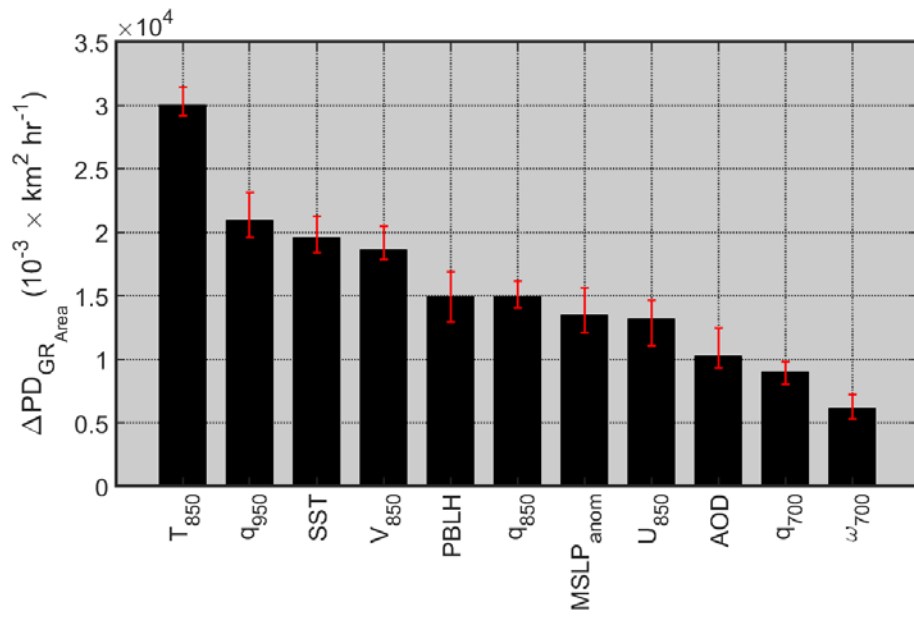
Formatted: Font: Italic

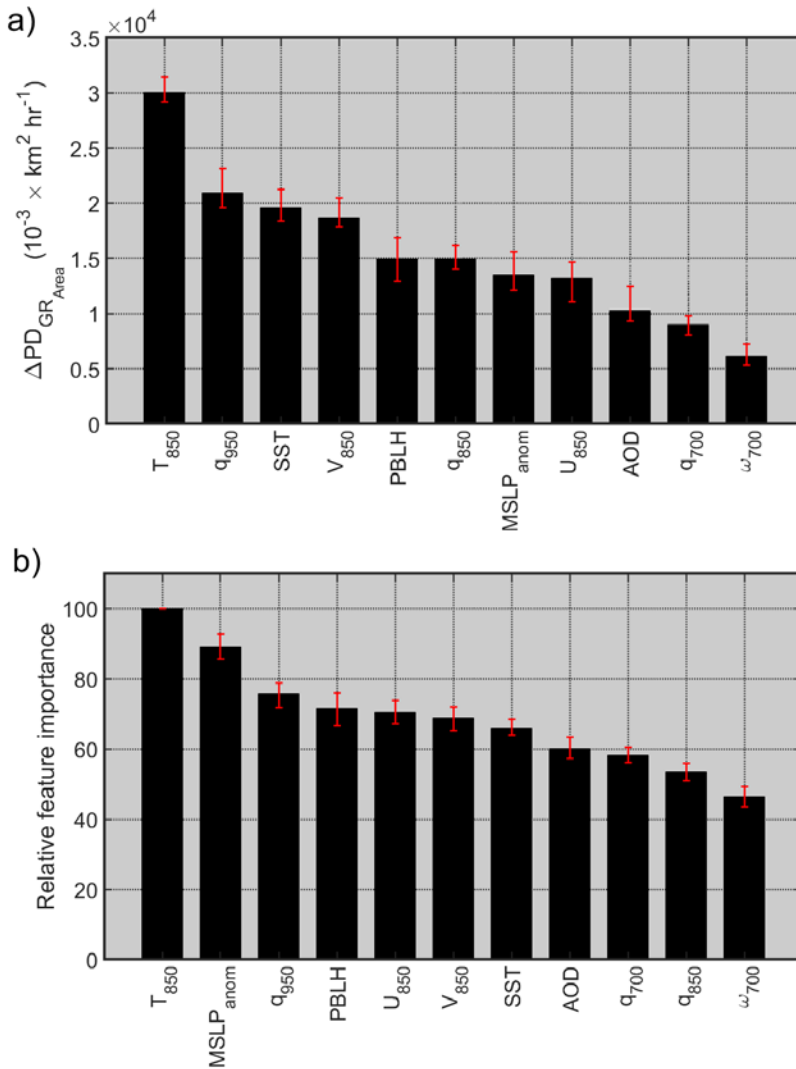
Formatted: Font: Italic

Formatted: Font: Italic

Formatted: Font: Italic



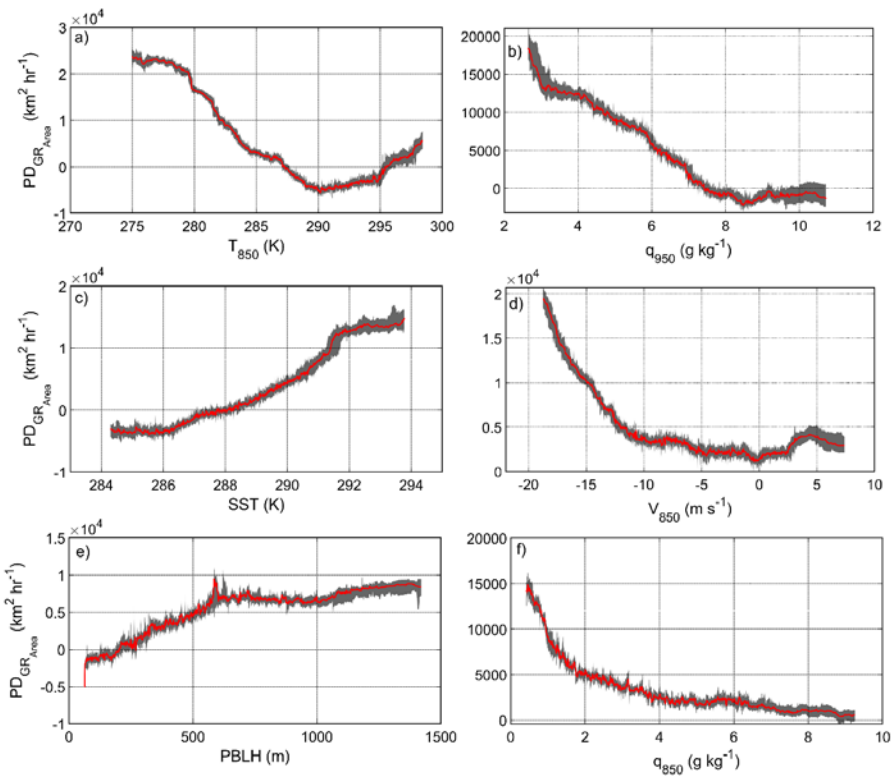




**Figure 11. The10.** Two scoring methods used for measuring the relative influence of input variables in the GBRT model: a) the median difference of maximum and minimum partial dependence (PD) of clearing growth rate ( $GR_{Area}$ ), and b) the median of relative feature importance calculated based on the method developed by Friedman (2001). Error bars represent the range of variability in 30 model runs. Note that GBRT simulations were performed using clearing growth rates obtained from the analysis of first and second GOES images (~09:00 – 12:00 PST) for all 306 clearing events examined.

Formatted: Font: Italic

Formatted: Font: Italic



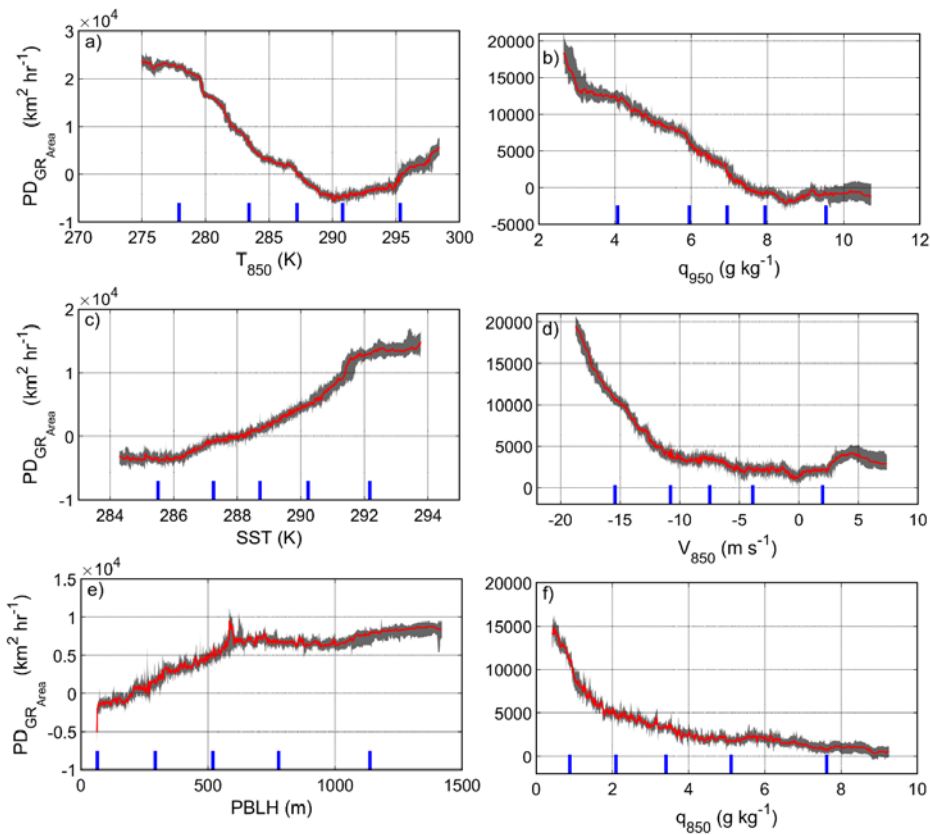


**Figure 1211.** The median partial dependence ( $PD$ ) of clearing growth rate ( $GR_{Area}$ ) on the following parameters: a) air temperature at 850 hPa ( $T_{850}$ ), b) air specific humidity at 950 hPa ( $q_{950}$ ), c) sea surface temperature ( $SST$ ), d) meridional wind speed at 850 hPa ( $V_{850}$ ), e) planetary boundary layer height ( $PBLH$ ), f) air specific humidity at 850 hPa ( $q_{850}$ ), g) mean sea level pressure anomaly ( $MSLP_{anom}$ ), h) zonal wind speed at 850 hPa ( $U_{850}$ ), i) aerosol optical depth ( $AOD$ ), j) air specific humidity at 700 hPa ( $q_{700}$ ), and k) vertical pressure velocity at 700 hPa ( $\omega_{700}$ ). **Red Shaded Grey shaded** areas represent the range of variability of  $PD$  for 30 model runs. **Blue lines** represent the values of the (left to right) 5<sup>th</sup>, 25<sup>th</sup>, 50<sup>th</sup>, 75<sup>th</sup>, and 95<sup>th</sup> percentiles of the input parameter. GBRT simulations were performed using clearing growth rates obtained from the analysis of first and second GOES images (09:00 – 12:00 PST) for all 306 clearing events examined.

Formatted: Font: Italic

Formatted: Font: Italic

Formatted: Font: Italic

Formatted: Font: Italic

Formatted: Font: Italic

Formatted: Font: Italic

Formatted: Font: Italic

Formatted: Font: Italic

Formatted: Font: Italic

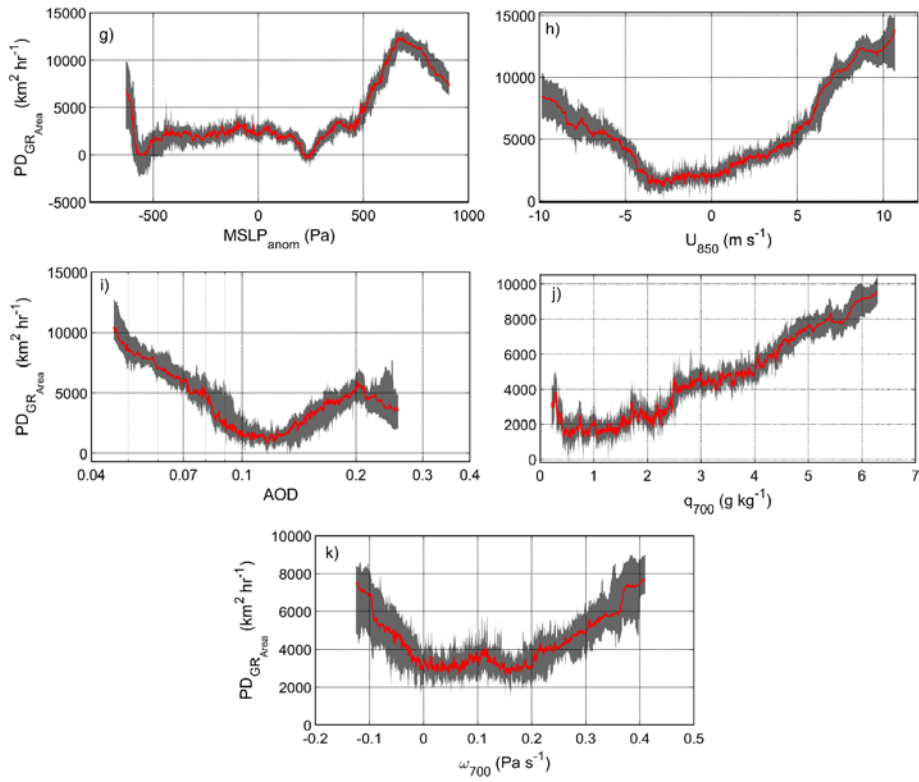
Formatted: Font: Italic

Formatted: Font: Italic

Formatted: Font: Italic

Formatted: Font: Italic

Formatted: Font: Italic



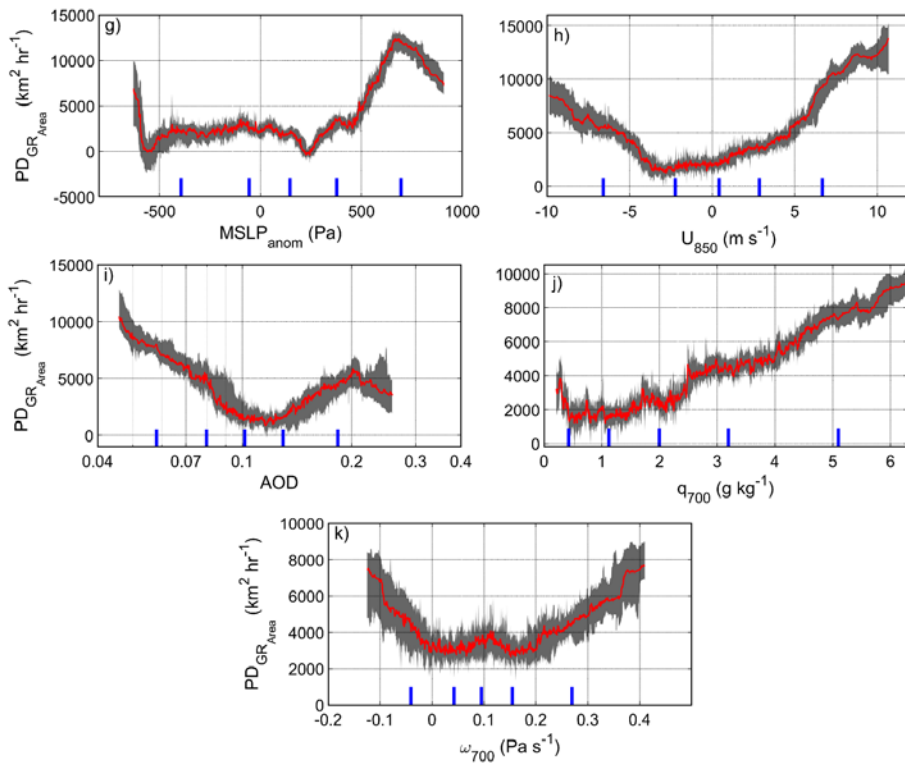
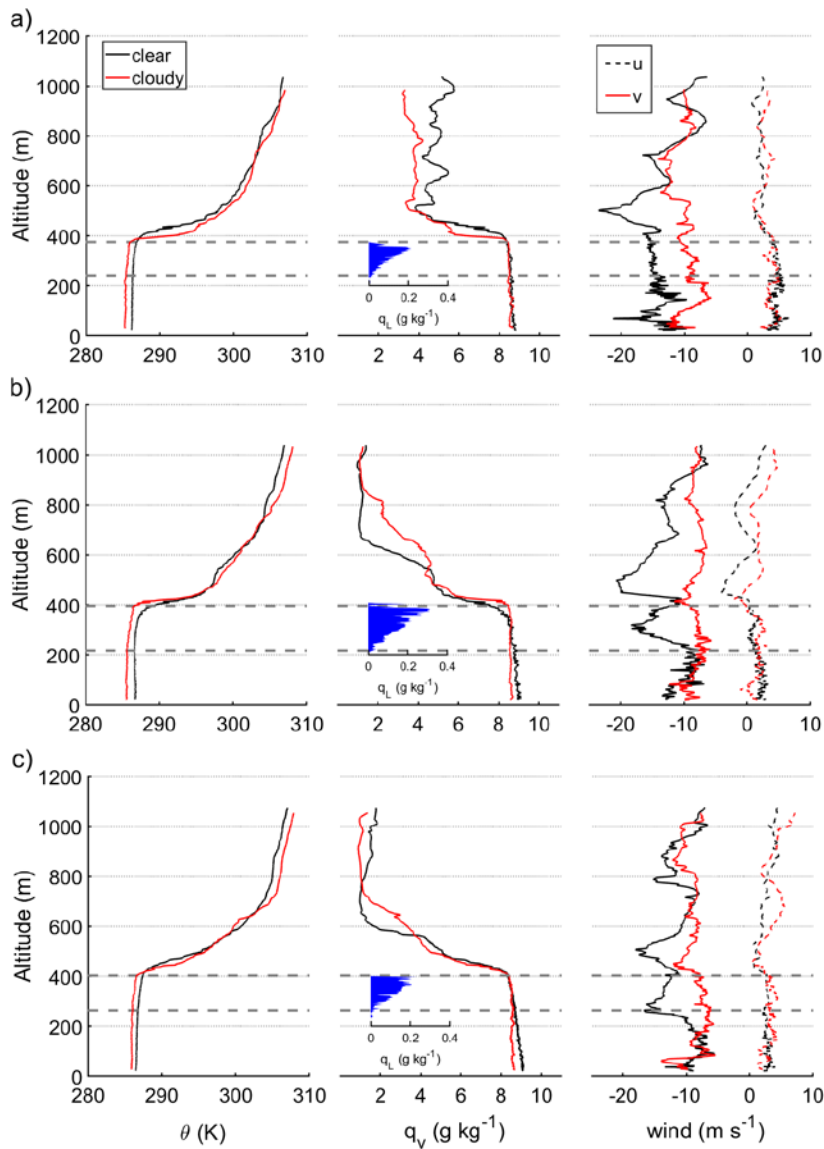


Figure 1211 (continued).

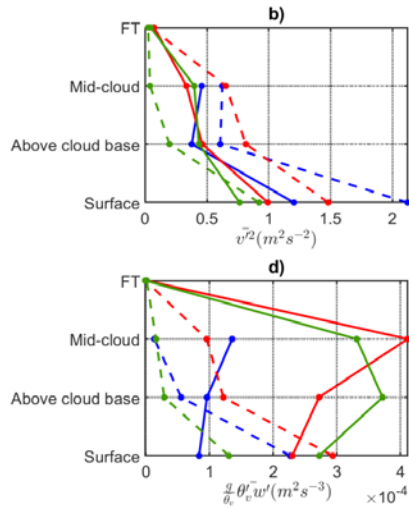
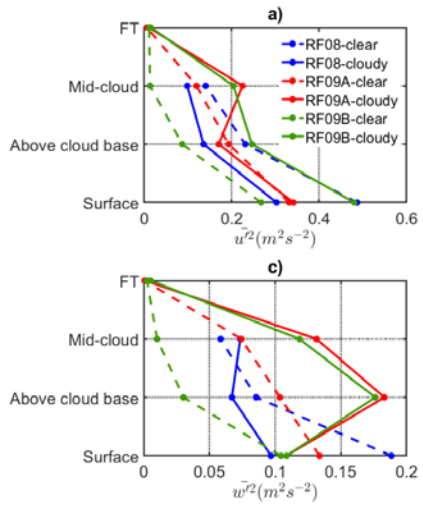


**Figure 13.12.** Sounding profiles of clear and cloudy columns for three case research flights examined in the FASE campaign: a) RF08, b) RF09A, c) RF09B. Horizontal wind speeds are decomposed into two components, ( $u$ ) perpendicular and ( $v$ ) parallel, relative to the cloud edge. Cloud base and top borders are marked with dashed lines.

Formatted: Font: Italic

Formatted: Font: Italic





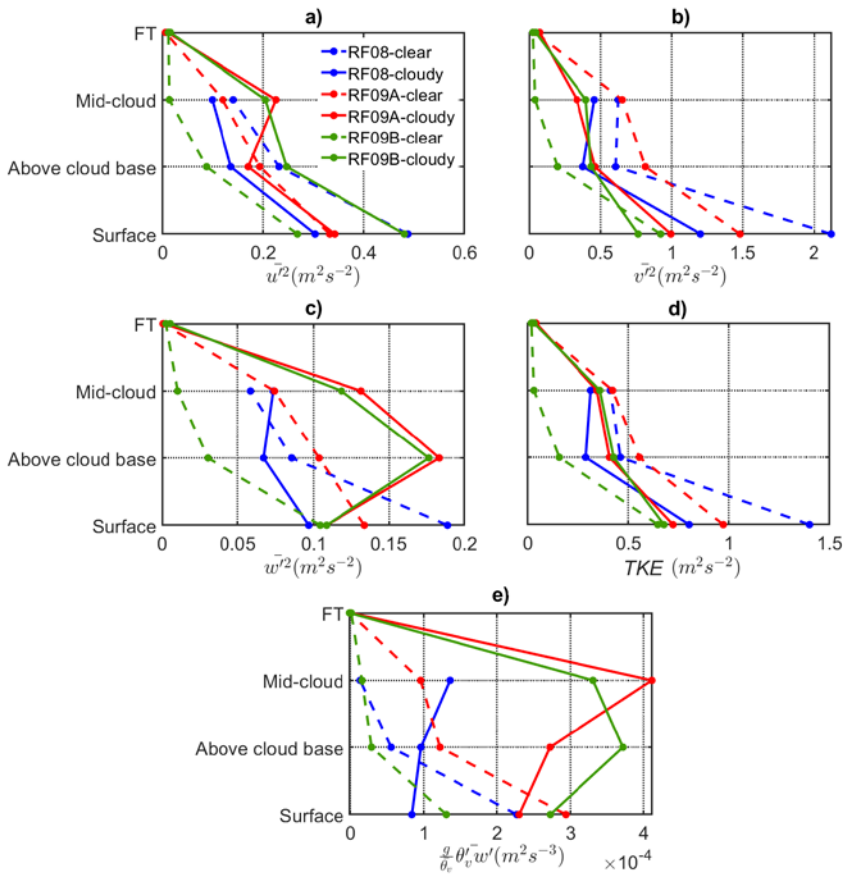


**Figure 1413.** Selected dynamic parameters for the clear (dash lines) and cloudy (solid lines) parts of the legs performed at different altitudes for three FASE case research flights: Panels a-c) exhibit squared average velocity fluctuations of wind speed components ( $\bar{u}'^2$  and  $\bar{v}'^2$  horizontal components,  $\bar{w}'^2$  vertical component). Horizontal wind speeds are decomposed into two components, ( $\bar{u}'^2$ ) perpendicular and ( $\bar{v}'^2$ ) parallel, relative to the cloud edge. Panel d) shows and e) display turbulent kinetic energy and buoyancy flux profiles, respectively, for the three flights.

- Formatted: Font color: Text 1
- Formatted: Font color: Text 1
- Formatted: Font: Italic, Font color: Text 1
- Formatted: Font color: Text 1
- Formatted: Font: Italic, Font color: Text 1
- Formatted: Font color: Text 1
- Formatted: Font: Italic, Font color: Text 1
- Formatted: Font color: Text 1
- Formatted: Font: Italic, Font color: Text 1
- Formatted: Font color: Text 1
- Formatted: Font: Italic, Font color: Text 1
- Formatted: Font color: Text 1
- Formatted: Font color: Text 1
- Formatted: Font color: Text 1
- Formatted: Font: (Default) +Body (Calibri), 11 pt